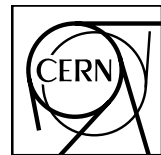


EUROPEAN ORGANIZATION FOR NUCLEAR RESEARCH



ALICE-PUBLIC-2013-xxx
February 14, 2013

Letter of Intent A Forward Calorimeter (FoCal) for the ALICE experiment

The ALICE FoCal Collaboration*

Abstract

We propose to construct a forward electromagnetic calorimeter (FoCal) as an upgrade to the ALICE experiment. This new detector will provide unique capabilities to study small- x gluon distributions via prompt photons and will also significantly enhance the capabilities of ALICE for general photon- and jet-related measurements. The FoCal is a finely granular Si/W-calorimeter covering pseudorapidities up to $\eta \simeq 5$.

*See Chapter 6 for the list of participating institutions.

Executive Summary

It is proposed to build a Forward Calorimeter (FoCal) as an upgrade of the ALICE experiment at the CERN LHC. The FoCal will extend the capabilities of the ALICE experiment to study the properties of hot and dense partonic matter, for which ALICE was designed, adding new capabilities to study cold dense partonic matter. The FoCal also provides unique capabilities at the LHC to investigate Parton Distribution Functions (PDFs) in a new regime of very small Bjorken- x and low Q^2 , where it is expected that the PDFs evolve non-linearly due to the high gluon densities, a phenomenon referred to as gluon saturation. The primary physics objective of the FoCal is to provide high precision measurements of direct photons in $p + p$ and $p + A$ collisions, which constrain PDFs at small x and low Q^2 , in the nucleon and in nuclei.

The FoCal will also add capabilities to measure jets, as well as coincident gamma-jet and jet-jet in the same reactions, providing further constraints on small x PDFs. It will also significantly enhance the ALICE capabilities for jet quenching studies in $A + A$ collisions with the measurement of the nuclear modification factor of π^0 at forward rapidities and with the ability to select on events with a direct photon or jet in the FoCal, and to use the full power of the ALICE detector to study the details of the event and the recoiling jet at mid-rapidity in the central detectors of ALICE. In particular, it will complement the unique forward quarkonium studies with simultaneous constraints on the longitudinal density profile from parton energy loss studies at the same rapidities.

A key feature of FoCal is the ability to reconstruct π^0 decays at forward rapidity and up to large transverse momenta $p_T > 20 \text{ GeV}/c$. This not only provides a precise measurement of π^0 production, which is a dominant background for the direct photon measurement, but also allows for a direct rejection of decay photons.

The typical opening angles of π^0 decays at forward rapidity are small, due to the longitudinal boost. Such decays can be reconstructed only with a high-granularity compact silicon-tungsten (Si/W) sampling electromagnetic calorimeter with longitudinal segmentation. The segments will consist of sampling layers of tungsten and silicon pads ($\sim 1 \text{ cm}$) summed longitudinally in towers, with a layer of silicon pixel or mini-pad ($\sim 1 \text{ mm}$) readout between longitudinal segments. The layers with very fine granularity allow to discriminate between isolated photons and decay photons from neutral pions.

We have performed detailed performance studies with detector simulation and reconstruction for selected physics observables. In particular, we show that the proposed setup is capable of measuring direct photons in $p+p$ and $p+Pb$ collisions in the forward region with p_T above about $5 \text{ GeV}/c$, up to large $p_T > 20 \text{ GeV}/c$ with a precision of better than 10% over most of the range. This measurement will provide unique new constraints to the gluon density in the Pb nucleus. In addition, π^0 measurements will be possible in $p+p$ and $p+Pb$ collisions, which can further probe CGC and saturation effects. Simulations with $Pb+Pb$ collisions show that a π^0 measurement will certainly be possible over the momentum range $7 < p_T < 20 \text{ GeV}/c$, providing new insights in parton energy loss at forward rapidities.

Explanatory note to ALICE readers: In the initial FoCal design it was intended to replace the existing ALICE Photon Multiplicity with a very fine granularity electromagnetic calorimeter at the PMD location inside the L3 magnet at ~ 3.5 m. This option would allow high precision direct photon and modest jet measurements in the rapidity range of $y \sim 2.5 - 4.5$, probing x values as low as $\sim 5 \times 10^{-6}$. Simulations were performed for this FoCal geometry and used to development the necessary analysis algorithms, and to obtain the first performance plots shown here. It was later realized that a superior design would consist of a very fine granularity electromagnetic calorimeter backed by a hadronic calorimeter, located outside the L3 magnet at a distance of about 8 m from the ALICE interaction region. This option would allow high precision direct photon and jet measurements in the rapidity range of $y \sim 3.3 - 5$, and provide a unique capability at the LHC to probe x values as low as $\sim 10^{-6}$. However, this option would require modifications of the ALICE infrastructure and beam pipe, which seem feasible according to initial investigation by ALICE technical support. Initial simulation results shown here demonstrate that measurements at the 8 m location are equally feasible (or improved even). The 8 m location is therefore preferred, and if this preference is endorsed by ALICE, the 4 m option would be eliminated from the document before submission to the LHCC, and all performance plots would be replaced by those now being produced for the 8 m location. Furthermore, the FoCal provides a unique capability at the LHC to measure direct photons as a means to investigate the phenomena of gluon saturation, as the current document demonstrates. The FoCal will also contribute significantly to the ALICE Pb+Pb program through many different measurements, some of which will be unique at the LHC, such as identified particle (π^0 and η) R_{AA} at very forward rapidity, although less compelling as justification for the FoCal construction. It is intended that the document will be updated with a selection of Pb+Pb performance plots, as they become available.

Contents

1 Physics Motivation	6
1.1 Nucleon parton distributions at small x	7
1.2 Nuclear parton distributions and gluon saturation	12
1.3 Medium properties in nucleus-nucleus collisions	19
1.4 The physics case for a forward calorimeter in ALICE	22
2 Conceptual Design	31
2.1 General Design Considerations	31
2.2 The FoCal Design	34
2.2.1 The FoCal-E Design	34
2.2.2 The FoCal-H Hadronic Calorimeter Design	37
2.3 The FoCal Configuration for Simulations	38
3 Standalone Performance	39
3.1 MC simulation and analysis algorithms	39
3.1.1 GEANT3 Model	39
3.1.2 AliROOT configuration	39
3.2 Analysis framework	40
3.2.1 Clustering algorithm	40
3.2.2 Shower reconstruction algorithm	41
3.3 Single photon reconstruction	42
3.3.1 Photon identification	45
3.4 Neutral meson reconstruction	47
4 Performance in p+p, p+A, and Pb+Pb	50
4.1 Efficiency in p+p	50
4.1.1 Direct photon yield expectations	50
4.1.2 FoCal at 4m	51
4.1.3 FoCal at 8m	56

4.2	Efficiency in p+Pb	58
4.3	Isolation cuts with FoCal-H	61
4.4	Performance with reduced granularity	63
4.5	Efficiency in Pb+Pb	66
4.6	γ_{dir} and jet measurements in Pb+Pb collisions	68
4.7	Physics Performance Summary	69
5	Technical Implementation	71
5.1	Mechanics	71
5.1.1	FoCal-E Mechanics	71
5.1.2	FoCal-H Mechanics	74
5.2	Sensors and Electronics	78
5.2.1	Silicon pad sensors and electronics for the LGL	78
5.2.2	Monolithic Active Pixel Sensors for HGL	81
5.2.3	FoCal-H sensors and electronics	83
5.3	DAQ	83
5.3.1	LGL Readout	84
5.3.2	HGL Readout	84
5.4	Integration	84
6	Project Management and Organisation, Participating Institutes, Cost Estimates and Time Schedule	86
6.1	Project Management and Organisation	86
6.2	Participating Institutes	86
6.3	Cost Estimates	87
6.4	Time Schedule	89
A	Analysis algorithms	93
A.1	Description of clustering algorithm	93
A.2	Description of shower reconstruction algorithm	94

B FoCal R&D and Prototype Results	94
B.1 W+Si pad prototype	94
B.1.1 Pad sensor ASIC development at CNS:	98
B.1.2 Pad sensor ASIC development at ORNL:	100
B.2 W+Si MAPS prototype and beam tests	102

1 Physics Motivation

Knowledge of the density of quarks and gluons (partons in general) in a nucleon or a nucleus is crucial to the understanding of particle production in high-energy collisions. While the parton distribution functions (PDFs) for the nucleon are relatively well known over a broad range of Bjorken- x (the fraction of the nucleon momentum carried by the parton), new regions of small x have become accessible at the LHC with the increase in the \sqrt{s} of the collisions. On general grounds, it's expected that at very small x and small Q^2 the parton densities (particularly, the gluon density) will become so large that the assumptions of conventional pQCD descriptions will break down. Measurements that probe the parton distributions in this kinematic regime of gluon saturation will provide fundamental input to the theoretical understanding and treatment of such cold dense partonic matter. In addition, saturated gluon matter is expected to behave as classical gluon fields, and as such this new state of matter is of interest in its own right.

Furthermore, nuclei cannot be treated as simple superpositions of protons and neutrons. In particular, the effects of high parton density at low x are amplified in nuclei. As a result, their PDFs are subject to large uncertainties in kinematic regions of interest to current experiments. This is particularly important for the study of the hot and dense strongly interacting matter created in high-energy nuclear collisions. Many observables relevant for this research study modifications of particle distributions in nuclear collisions relative to p+p collisions, as for example, the suppression of heavy quarkonium, or the suppression of high transverse momentum hadron (i.e. jet) production. The quantitative interpretation of these modifications requires precise knowledge of any initial state modifications in nuclei, also called *cold nuclear matter* effects, to be able to disentangle them from those attributable to the hot high density partonic matter created in those collisions.

We propose to build a forward calorimeter (FoCal) as an upgrade to the ALICE setup. The detector is designed to measure prompt photons in the pseudorapidity range $2.5 \sim 3. < \eta < 4.5 \sim 5.$ (depending on final design choice) over the full azimuth and over a large transverse momentum range from a few GeV/c up to $p_T \approx 100 \text{ GeV}/c.$ The FoCal will provide photon isolation capability to separate fragmentation photons from prompt photons and will allow to discriminate photons from neutral pions at large momenta. It will also provide jet measurement capability. It will allow to

- measure isolated prompt photons to study yields and correlations over a rapidity and transverse momentum range significantly beyond that provided by existing detectors, which will give access to the low- x structure of protons and nuclei relevant to gluon saturation physics, and
- extend the general capabilities of ALICE for measurements of direct photons, pions, and other neutral hadrons, as well as jets, towards higher rapidity, as well as correlations between these measurements and measurements with the central detectors of the ALICE experiment, for more detailed QGP studies, and
- provide the capability to trigger on photons and jets in a large acceptance at forward rapidity.

1.1 Nucleon parton distributions at small x

The factorization theorem of QCD prescribes that the cross section for production of a hadron in a hard-scattering process of a nucleon-nucleon collision, can be factorized into long-distance and short-distance contributions [1]. The leading contribution to the hadron production cross section from a single hard collision between two partons, a and b (quarks or gluons) within incoming nucleons, A and B , can be written in factorized form as

$$E_h \frac{d\sigma_{AB \rightarrow h(p)}}{d^3 p_h} = \sum_{abk} \int d^3 x_2 f_{b|B}(x_2) \int d^3 x_1 f_{a|A}(x_1) \int dz D_{h|k}(z) E_k \frac{d\hat{\sigma}_{ab \rightarrow k}}{d^3 p_k} \quad (1)$$

where $x_1 = p_A/p_a$ ($x_2 = p_B/p_b$) is the fraction of the momentum of nucleon A (B) carried by parton a (b), $f(x, Q^2)$ is the distribution of the parton momentum fraction, or parton distribution function (PDF), in the nucleon when resolved at momentum transfer scale Q^2 , and $E_k \frac{d\hat{\sigma}_{ab \rightarrow k}}{d^3 p_k}$ is the elementary cross section for the interaction of partons a and b to produce parton k in the final state with momentum p_k . The probability for parton k to fragment and produce a hadron carrying a momentum fraction $z = p_h/p_k$ is given by the fragmentation function $D_{h|k}(z)$. The total hadron production cross section is given by summing over all parton interaction processes that can lead to the specified hadron in the final state, integrated over the initial parton distributions and fragmentation distributions.

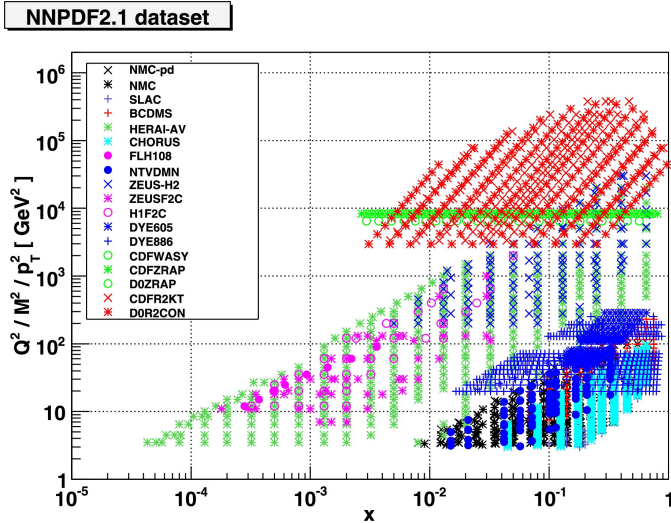


Fig. 1: The x and Q^2 corresponding to various measurements used in the determination of the NNPDF2.1 PDFs. The analysis includes results from DIS, Drell-Yan, inclusive jet, and weak vector boson production, as well as charm production (see Ref. [5] for details).

The parton distributions and fragmentation functions encapsulate the short-distance behavior that is not calculable from first principles in QCD (except possibly in lattice QCD). On the other hand, QCD prescribes how these distributions should evolve, as the scale (Q^2) at which they are probed is varied, as given by the DGLAP evolution equations [2, 3, 4]. The PDFs are determined empirically as the result of a best-fit comparison of pQCD predictions, assuming factorization

as in Eq.1 and DGLAP evolution, to a variety of experimental measurements of hard-scattering processes, which cover a broad range of Q^2 . As has been done by other groups in the past, the NNPDF collaboration has analyzed a large number of measurements including deep-inelastic scattering (DIS), Drell-Yan, inclusive jet, and weak vector boson production spanning a large range of x and Q^2 , as shown in Fig.1, for determination of the recently determined NNPDF2.1 [5] PDFs. The overall consistency between data and theory, within their respective uncertainties, provides strong support for QCD in general, and specifically for the factorization assumption with universal PDFs that evolve according to the DGLAP equations.

Nevertheless, on general grounds, it is expected that at small x and small Q^2 the parton density will become so large that non-linear effects due to gluon fusion will compete with isolated splittings and invalidate the assumption of linear DGLAP evolution of the PDFs. This so called regime of *gluon saturation* or *color glass condensate* [6] is expected to occur when the product of the gluon areal density $\rho \sim xg(x, Q^2)/\pi r^2$ times the gluon fusion cross section $\sigma_{gg \rightarrow g} \sim \alpha_s/Q^2$ is greater than unity, $\rho \sigma_{gg \rightarrow g} \gtrsim 1$. Here $xg(x, Q^2)$ is the number of gluons in the nucleon and πr^2 is the cross sectional area of the nucleon. This leads to the expectation that the region of gluon saturation is entered when Q is less than the saturation scale Q_s given by

$$Q_s^2 \sim \alpha_s \frac{xg(x, Q^2)}{\pi r^2} \sim x^{-0.3} \quad (2)$$

Within the framework of the NNPDF global analysis it has recently been shown that the description of the global dataset shown in Fig. 1 can be improved by exclusion of the data in the region of small x and Q^2 by considering only the data with $Q^2 \gtrsim A_{cut}x^{-\lambda}$ with $\lambda = 0.3$ and $A_{cut} = 1 \sim 1.5$ GeV² in the PDF determination [7], i.e. by excluding the region where gluon saturation effects might be expected to play a role. The analysis suggests that improvement in this region is not expected by going from an NLO to NNLO treatment, but might be expected with resummation of powers of $\alpha_s \log(x)$, but also that the deviations may be due to the onset of saturation effects [7].

Due to the large increase in \sqrt{s} compared to previous colliders, measurements at the LHC probe the nucleon PDFs over a region of x and Q^2 that is much greater than that previously accessible, as shown in Fig. 2. While much of the p+p physics program at the LHC probes the PDFs in a region of large Q^2 , the Pb-Pb program is very much focussed on bulk particle production in the p_T region of a few GeV/c where $Q^2 (\approx p_T^2) \lesssim 10$ GeV² and $x \sim 10^{-3} - 10^{-4}$, where gluons are the dominant partons. Much of the information about PDFs at low- x and low Q^2 come from DIS measurements (see Fig. 1). However, because gluons are uncharged they are not directly probed in the DIS process, but constrained only indirectly, such as by momentum sum rules, with the result that gluon PDFs have rather large uncertainties in the low- x and low Q^2 region, as shown in Fig. 3 [7].

Measurements of isolated direct photons can provide strong constraints on the gluon PDFs. At leading order the dominant process is the quark-gluon Compton process, shown in Fig. 4a), with quark-anti-quark annihilation contributing mostly at large x . At leading order, the photon is produced directly at the parton interaction vertex without fragmentation ($D(z) \equiv 1$ in Eq. 1). On the other hand, at next-to-leading order, photons may also be produced in bremsstrahlung or

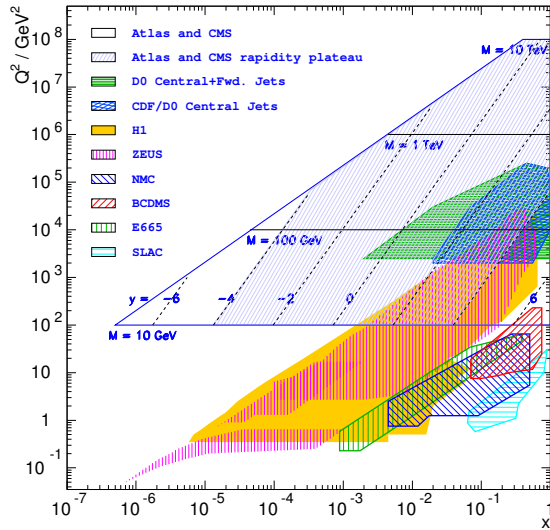


Fig. 2: The x and Q^2 regions of coverage of previous measurements showing the extended region that will be probed by measurements at the LHC (for processes with $Q^2 > 100 \text{ GeV}^2$).

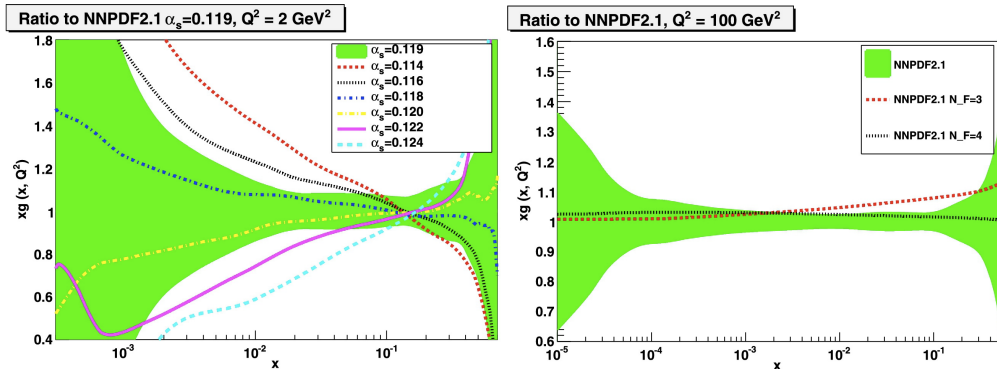


Fig. 3: The ratio of the gluon distribution function $xG(x, Q^2)$ to the nominal value with shaded region showing the theoretical uncertainty at $Q^2 = 2$ (left) and $Q^2 = 100 \text{ GeV}^2$ (right). The curves show the sensitivity to changes in specific assumptions (on α_s and n_f : see Ref. [7]).

fragmentation of one of the outgoing partons (see Fig. 4 c) and d)), in which case the parton-to-photon fragmentation distributions $D_{\gamma|k}(z)$ are required in the calculation of the rate. At LHC energies, the majority of prompt photons are produced in the fragmentation process, complicating the relationship between the kinematic variables of the measured photon and those of the incoming partons (and their PDFs). However, fragmentation photons are typically being found within the *jet cone* of hadrons from the fragmentation of the parton into a jet, and by application of isolation cuts their contribution can be largely suppressed, as shown for example in Fig.5 [8], such that the dominant process is the quark-gluon Compton scattering process, with the measured photon more directly reflecting the gluon PDFs.

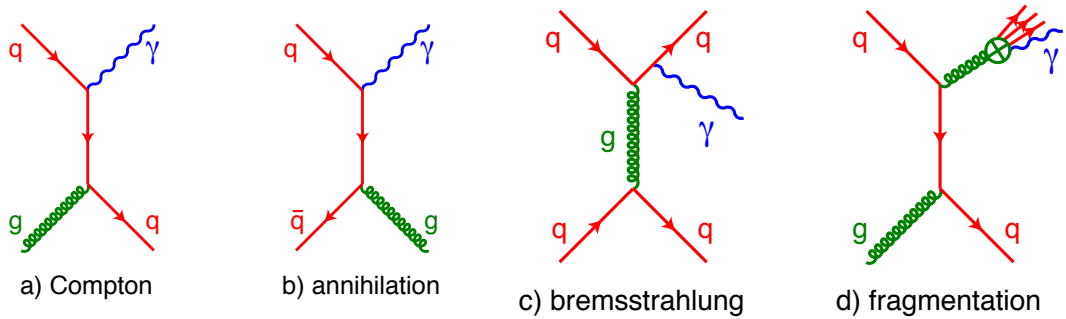


Fig. 4: Feynman diagrams for photon production. At leading order isolated photons from the a) quark-gluon Compton process, and b) quark-antiquark annihilation process. Non-isolated photons at next-to-leading order from c) bremsstrahlung from a quark, and d) emission during the gluon fragmentation process.

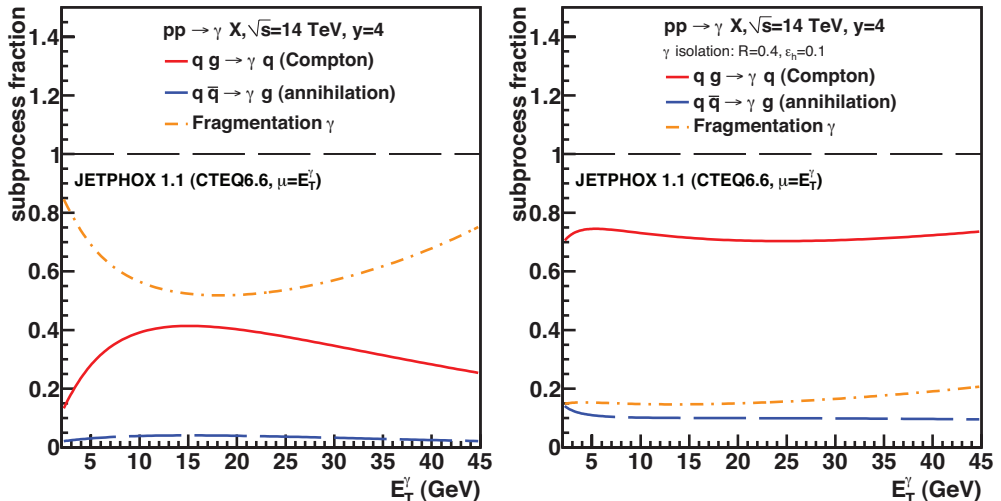


Fig. 5: Relative contributions of the qg -Compton, $q\bar{q}$ annihilation, and fragmentation subprocesses in NLO prompt photon production in p+p collisions at $\sqrt{s} = 14$ TeV at the LHC at forward rapidity obtained with the JETPHOX program (from [8]). Relative contributions are shown without (left) and with (right) an isolation cut.

Photons are also produced in radiative decays of fragmentation products, most dominantly from π^0 's and η 's, with a rate at low p_T that far exceeds the direct photon rates from the processes shown in Fig. 4. Although the decay photons can also be suppressed by isolation cuts, or directly identified through an invariant mass reconstruction of the parent π^0 , the direct photon measurements ultimately have a low p_T limit imposed by this dramatically increasing background of decay photons. Recent isolated photon measurements at the LHC have been performed by CMS down to $p_T > 25$ GeV/c ($2.1 < |\eta_\gamma| < 2.5$) and $p_T > 20$ GeV/c ($|\eta_\gamma| < 1.44$) in p+p collisions at 7 TeV [9, 10] and for $p_T > 20$ GeV/c ($|\eta_\gamma| < 1.44$) in 2.76 TeV p+p collisions [11]. ATLAS has published isolated photon measurements down to $p_T > 45$ GeV/c ($|\eta_\gamma| < 2.37$) [14] and

$p_T > 15 \text{ GeV}/c$ ($|\eta_\gamma| < 1.81$) [14] in 7 TeV p+p collisions. These LHC results were found to be consistent with NLO pQCD predictions, within uncertainties.

More generally, isolated photon results from all collider measurements have been shown to be consistent with NLO pQCD predictions using the JETPHOX program [15] and NNPDF2.1 PDFs, as shown in Fig. 6 (from [16]). When the isolated photon data sets are considered globally, it's found that the uncertainty on the gluon PDFs can be reduced by about 20% [16]. As seen in Fig. 6 the recent LHC isolated photon results probe the gluon PDFs in the x region down to about 5×10^{-3} at $Q^2 > 200 \text{ GeV}^2$, where the uncertainty on the gluon PDFs is relatively small (see Fig. 3), and where saturation effects are not expected. To probe the gluon distributions in the interesting region of smaller x and Q^2 , it will be necessary to perform the isolated photon measurements at the LHC at lower p_T and at more forward rapidity. For example, x values of 10^{-5} could be reached with a measurements at $y = 4$ if it can be carried out at as low as $p_T \sim 5 \text{ GeV}/c$.

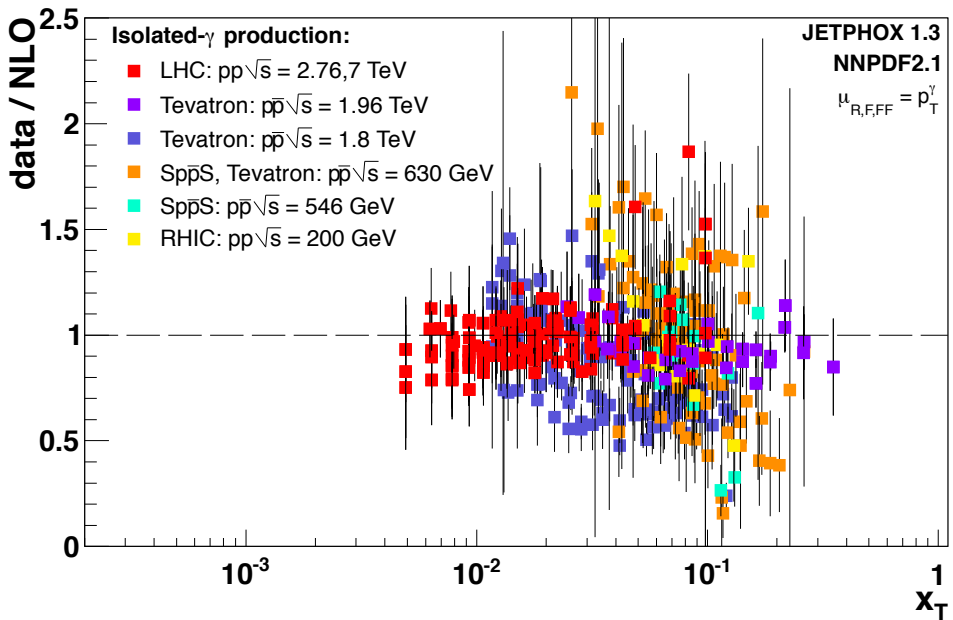


Fig. 6: Ratio of data/theory for all isolated photon measurements at p+p or p+ \bar{p} colliders versus $x_T = 2p_T/\sqrt{s}$. The NLO QCD predictions were calculated with JETPHOX 1.3 using the NNPDF2.1 PDFs (see [16] for details).

The parton distributions can be probed more precisely by constraining the kinematics of the underlying partonic interaction. Coincidence measurements allow to constrain the parton kinematics and provide such information. For a $2 \rightarrow 2$ hard scattering process at the parton level, such as in the quark-gluon Compton process of Fig. 4, the x -values of the incoming partons can be directly related to the transverse momentum and rapidity of the outgoing partons as

$$x_1 = \frac{p_T}{\sqrt{s}}(e^{y_3} + e^{y_4}) \quad (3)$$

$$x_2 = \frac{p_T}{\sqrt{s}}(e^{-y_3} + e^{-y_4}) \quad (4)$$

$$Q^2 = \frac{1}{4}x_1x_2s \quad (5)$$

where x_1 and x_2 are the momentum fractions of the two incoming partons, y_3 and y_4 are the rapidities of the outgoing partons, and $p_{T3} = p_{T4} = p_T$. When the outgoing partons have the same rapidity with $y_3 = y_4 = y$, then

$$x_2 = x_T e^{-y} \quad (6)$$

$$Q^2 = (\frac{1}{2}x_2 e^y \sqrt{s})^2 = p_T^2 \quad (7)$$

where $x_T = 2p_T/\sqrt{s}$. For an inclusive isolated photon measurement Eqs. 6 and 7 provide a reasonable estimate of x_2 and Q^2 since the rate is maximum for $y_3 \approx y_4$, where Q^2 is minimum. For a coincidence measurement, at leading order, the measurement of the prompt photon provides the measurement of the p_T , and of y_3 , leaving only the rapidity of the recoiling parton y_4 to be determined to fix the kinematics. In the case of the Compton or annihilation process, y_4 is the rapidity of the recoiling parton, which is then measured as the rapidity of the recoiling jet. Therefore, measurement of the angle (i.e. pseudorapidity) of the recoiling jet, or even the angle of the leading particle, such as a π^0 , within the jet, in coincidence with the isolated photon allows to approximately fix, or at least constrain, the x_1 and x_2 of the interacting partons, with the result that the integrals over x_1 and x_2 in Eq. 1 fall away, or are sharply limited. Thus, if x_1 lies in a region where the PDFs are well-known, then $f(x_2)$ ($\equiv g(x, Q^2)$ for the gluon) is "measured" nearly directly by the γ -jet (or γ -hadron) coincidence measurement.

1.2 Nuclear parton distributions and gluon saturation

It has been realized since 1983 from measurements of DIS on Fe targets by the European Muon Collaboration [17] that the parton distributions of a nucleus with N neutrons and Z protons is not trivially given as the superposition of N neutron and Z proton PDFs. Instead, there are a variety of effects, relevant in different x regions, which modify the parton distributions in a nucleus in such a complex manner that the nuclear PDFs (nPDFs) must be extracted from a global analysis of QCD predictions for various measurements of hard processes with nuclear targets, in a manner completely analogous to what is done for the extraction of the nucleon PDFs, as discussed above. Figure 7 shows, as example, the ratio of the gluon distribution function of a Pb nucleus to that of the proton as a function of x for different parameterizations of the gluon nPDF. The various parameterizations exhibit a large spread for small values of x , reflecting the general lack of constraints due to the limited set of relevant measurements with nuclear targets.

The nuclear gluon distributions have been determined assuming linear QCD evolution, which implies that the real uncertainties at very low x are even larger due to the expected stronger effects of gluon saturation. As discussed above, the density of partons carrying a small momentum fraction x within a nucleon is known to increase when probed at small momentum transfer Q^2 (i.e. low spatial resolution). At low parton density, this increase with decreasing x can be successfully described within perturbative QCD. However, for large gluon densities, non-linear

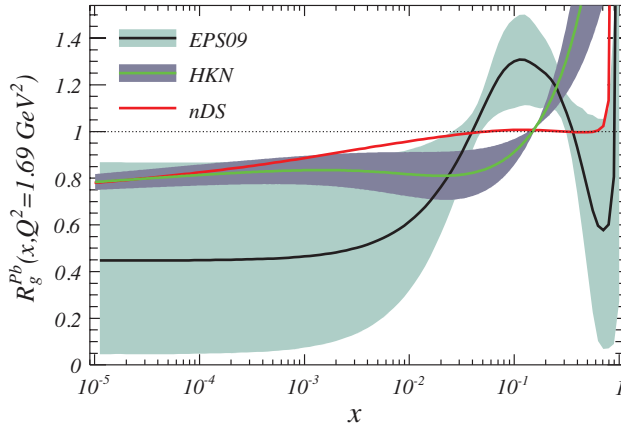


Fig. 7: Ratio of the gluon distribution functions of a Pb-nucleus to that of the proton for different parameterizations of the nuclear PDFs [18] at $Q^2 = 1.69 \text{ GeV}^2$.

effects become important and an increase in the number of gluons due to branchings will compete with a decrease due to gluon fusion. Following the same argumentation as above for the case of the nucleon (see Eq. 2), gluon fusion will play a dominant role when the product of the gluon density and gluon fusion cross section becomes greater than unity. The gluon density of a nucleus of mass number A is approximately $xG(x, Q^2) \approx Axg(x, Q^2)$ and the cross sectional area of the nucleus is approximately $\pi R^2 \approx \pi(rA^{1/3})^2$ with the result that the saturation regime in nuclei will be reached at a higher Q^2 than in a nucleon, specifically when Q^2 is less than the saturation scale Q_s given by

$$Q_s^2 \sim \alpha_s \frac{xG(x, Q^2)}{\pi R^2} \sim A^{1/3} x^{-\lambda} \quad (8)$$

where $\lambda \approx 0.3$ as above. Thus the effects of gluon saturation are expected to set in at a factor of ~ 6 higher Q^2 with a heavy nuclear target. In fact, if the impact parameter b of the interaction can be selected, such as by a selection on the particle multiplicity, the factor would vary from ~ 1 for peripheral collisions, to $\sim 2A^{1/3}$ for $b = 0$ collisions.

The experimentally accessible saturation region increases substantially with center-of-mass energy. Measurements at the LHC with its much larger \sqrt{s} will facilitate a major advance for investigation of gluon saturation effects in nuclei. Fig. 8 illustrates the kinematic extent of the saturation for p+A (or d+A) collisions as a function of the outgoing parton p_T and y at the RHIC and LHC accelerators. At the LHC, the x -values at a given rapidity are smaller, such that the saturation region extends to larger p_T -values. In general, the LHC will give access to a significantly larger region of phase space that is dominated by gluon saturation, and in particular, the region of gluon saturation will extend to p_T values high enough that perturbative QCD should otherwise be applicable. To study the details of gluon saturation experimentally, one would like to measure isolated photon production over a wide range of rapidity and transverse momenta, particularly extending the measurements as low in p_T as possible. In this way, much of the saturation region indicated in Fig. 8 would become accessible.

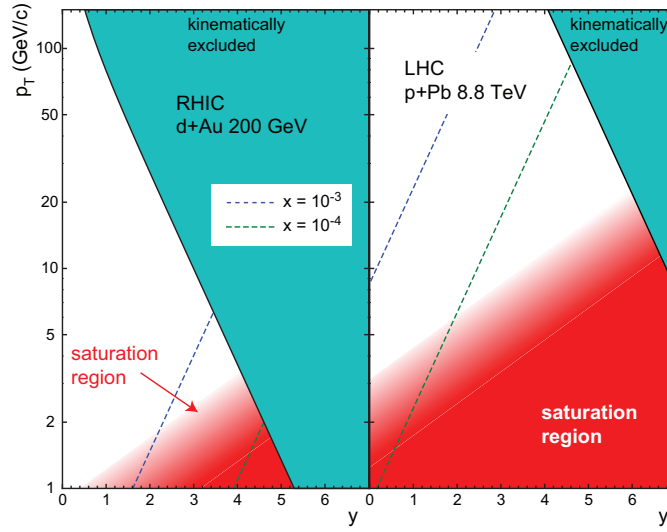


Fig. 8: Accessible phase space for hadron production as a function of rapidity y_h and transverse momentum p_T , in collider experiments at RHIC and LHC. The red areas indicate estimates of the region where gluon saturation should be observable ($p_T < Q_s$).

Nuclear effects on hadron production in nucleus-nucleus collisions are quantified by measurement of the nuclear modification factor

$$R_{AB} = \frac{\frac{1}{p_T} \frac{dN_{AB}^h(b)}{dp_T}}{\langle N_{\text{coll}}(b) \rangle \frac{1}{p_T} \frac{dN_{pp}^h}{dp_T}} \quad (9)$$

for collisions of nuclei of mass number A with nuclei of mass number B, at impact parameter b (or for a range of centrality selection) with $1/p_T \cdot dN_{AB}^h(b)/dp_T$ the invariant yield of hadron h per event, for that centrality selection, and $1/p_T \cdot dN_{pp}^h/dp_T$ the invariant yield of hadron h per inelastic p+p event, and $\langle N_{\text{coll}}(b) \rangle$ the average number of binary nucleon-nucleon collisions for the chosen centrality selection. One expects $R_{AB} = 1$ in the absence of nuclear effects, if the nuclear result was simply equivalent to the result of a superposition of nucleon-nucleon collisions.

Many observables relevant for the investigation of the hot and dense partonic matter produced in ultra-relativistic heavy-ion collisions at the RHIC and LHC study modifications of particle distributions in nucleus-nucleus collisions relative to p+p collisions, through measurements of R_{AA} . These include, for example, the suppression of heavy quarkonium, or the suppression of high transverse momentum hadrons (i.e. jets). An interpretation of any observed deviations from $R_{AA} = 1$ as due to the effects of the hot and dense partonic matter produced in the collision, requires precise knowledge of possible initial state modifications of the nuclei, also called *cold nuclear matter* effects, to be able to disentangle them from those that should be attributed to the effects of the produced matter.

Saturated gluon matter would modify the initial conditions of the nucleus-nucleus collision. It

would reveal itself through two characteristic properties, which manifest themselves through particular signatures:

1. a suppression of the momentum distribution of gluons, which would lead to a suppression of inclusive hadron yields in a momentum range where parton scattering is dominant and
2. a change from a collection of incoherent gluons to a coherent state, which should be observable as a decrease and/or broadening of the azimuthal correlation between recoiling jets from parton-parton scattering.

These effects are not essentially different than effects that might be caused by the propagation of partons through the produced matter, and therefore they must be quantified before nucleus-nucleus results can be properly interpreted.

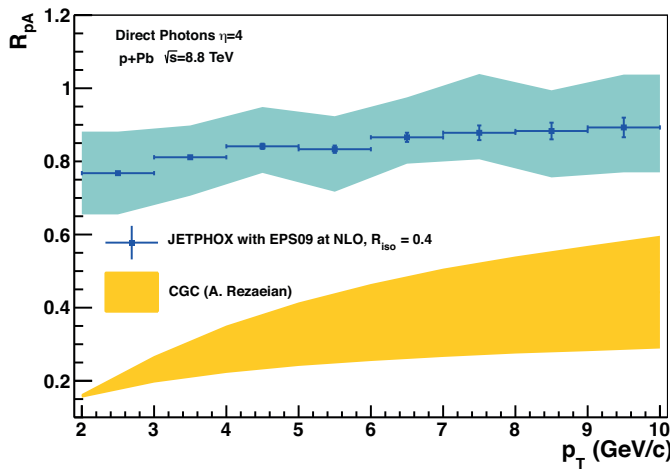


Fig. 9: Nuclear modification factor for direct photons for pPb collisions at 8.8 TeV at the LHC. Predictions for the gluon saturation model from [19] are compared to different calculations for isolated photons in NLO pQCD using JETPHOX with the EPS09 PDF sets. The blue shaded area indicates the uncertainty associated with the different error sets of those PDFs, while the orange band is an estimate of the systematic uncertainty of the CGC calculation.

Conclusive evidence for gluon saturation will be seen through observation of a deviation of particle yields from the predictions of perturbative QCD using linear evolution, with a deviation that increases in significance as the measurement goes further into the expected saturation region of low x and Q^2 . Predictions of the nuclear modification factor R_{pA} for the photon yields in pp and pA at the LHC that include the effects of gluon saturation [19] are compared with NLO pQCD calculations using nuclear PDFs [21] in Fig. 9. A significant difference is observed, with the predictions of the saturation model being below ~ 0.3 in particular at low p_T , while the pQCD calculations, including nuclear PDFs with shadowing, all predict R_{pA} greater than 0.6. The crucial test of the theoretical interpretation will be the ability to reproduce the details of the transverse momentum (i.e. Q^2) and rapidity (i.e. x) dependence of the nuclear suppression. The

signature of saturation physics will be the observation of this transition from agreement with the predictions of pQCD at high p_T , to a disagreement, which transitions to an agreement with the saturation predictions, at some low p_T reflecting Q_s , with the transition occurring at larger p_T (larger Q_s) as the rapidity of the measurement increases, reflecting the decreasing x (as per Eqs. 2 and 8).

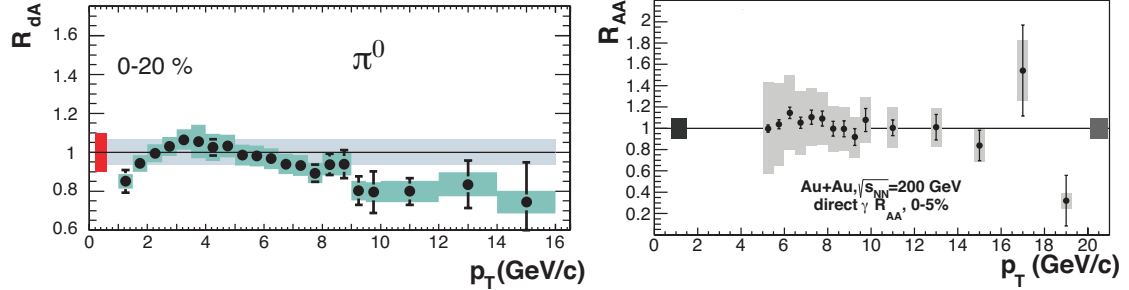


Fig. 10: Nuclear modification factor as a function of p_T as measured by the PHENIX experiment at mid-rapidity, on the left for neutral pions in central d+Au collisions [22] and on the right for direct photons in central Au+Au collisions [23].

Gluon saturation will very likely be visible through its effect on jet production, or on hadrons as jet fragmentation products. However, in addition to the difficulty to relate the measured kinematic variables of the final state to those of the initial state, strongly interacting probes have the additional disadvantage that they are likely to be affected by final state interactions in cold nuclear matter. This potential problem is illustrated with recent results from the PHENIX collaboration shown in Fig. 10. The nuclear modification factor for direct photons in central Au+Au collisions (right) shows no deviation from unity, indicating that no initial (or final) state nuclear effects are present. On the other hand, the nuclear modification factor for neutral pions in d+Au collisions (left) shows a suppression at high transverse momentum. Since initial state effects should be similarly present in d+A and A+A collisions, the suppression of R_{dA} for hadrons suggests the presence of final state modifications. Other hadronic measurements potentially sensitive to small x partons distributions, like e.g. forward J/ψ production, suffer from comparable final state modifications (nuclear absorption in this case) [20]. In addition, all hadronic probes provide much less direct information on parton kinematics. This indicates that initial state effects will be more difficult to extract and interpret from jet or hadron measurements, in comparison to direct photon measurements.

One of the most important findings in the study of high energy heavy ion collisions is the strong collectivity observed, in particular the large values of elliptic flow. Large values of v_2 are generally considered to be signs of hydrodynamic behaviour, which in turn requires local equilibration of the produced matter. The elliptic flow shows a straightforward dependence on the collision geometry. For ideal hydrodynamics it is proportional to the initial spatial eccentricity. Beyond that, its magnitude depends on the equation of state (EOS) of the matter produced. To extract this information from elliptic flow measurements knowledge of the initial density distributions, which determine the eccentricity, is important. This makes studies of gluon saturation significant

for the interpretation of elliptic flow in nucleus-nucleus collisions.

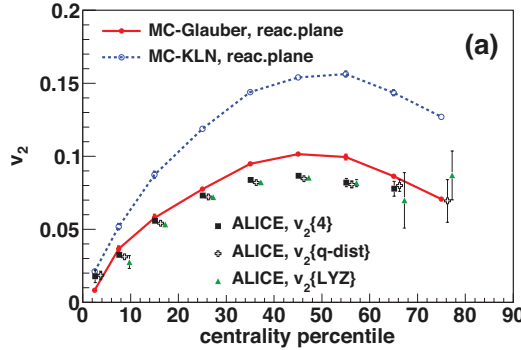


Fig. 11: Predictions for elliptic flow from a hybrid model [24] using two different assumptions for the description of the initial state with (MC-KLN) or without (MC-Glauber) gluon saturation compared to measurements from ALICE.

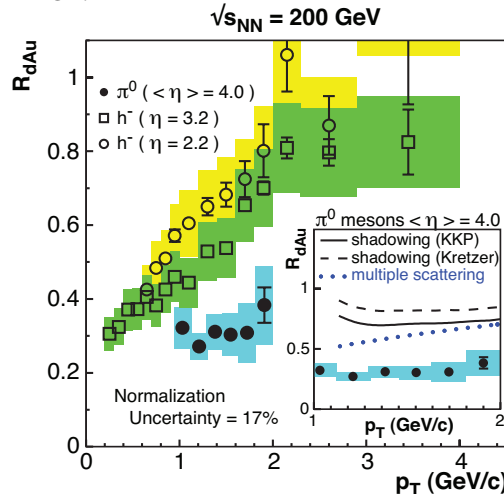


Fig. 12: Nuclear modification factor R_{dAu} for hadron production in d+Au collisions at forward rapidities as measured by STAR (π^0) and BRAHMS (negative hadrons). The inset illustrates that conventional calculations including shadowing effects are not able to describe the suppression shown in the STAR data (from [26]).

As an example, Figure 11 shows calculations of v_2 from a hybrid model [24] compared to experimental data. It is obvious that the two different initial state descriptions yield very different predictions, and that it will be crucial to provide another means to constrain the initial state to be able to resolve ambiguities in the interpretation of elliptic flow measurements.

Gluon saturation was able to explain the observed particle multiplicities in Au+Au collisions at RHIC, which turned out to be much smaller than initially predicted. However, a successful prediction of the multiplicity of produced particles is not sufficient evidence for gluon saturation. On the other hand, the production of hadrons at forward rapidities in d+Au collisions has been

observed to be suppressed, with a suppression that increases with increasing rapidity, as illustrated by the nuclear modification factor measured by BRAHMS and STAR shown in Fig. 12. The measurements show a significant suppression of the yield in d+Au collisions, implying a strong cold nuclear matter effect that is qualitatively consistent with the expectations for gluon saturation. Furthermore, studies of azimuthal particle-pair correlations have been performed by STAR and PHENIX. Preliminary results for pairs of neutral pions at forward rapidity measured by STAR are shown in Fig. 13 [25]. While a strong peak at $\Delta\phi = \pi$, associated with the recoil jet opposite to the trigger particle, is observed for p+p collisions, the correlation structure is apparently suppressed and/or broadened in central d+Au collisions, also in qualitative agreement with expectations from gluon saturation.

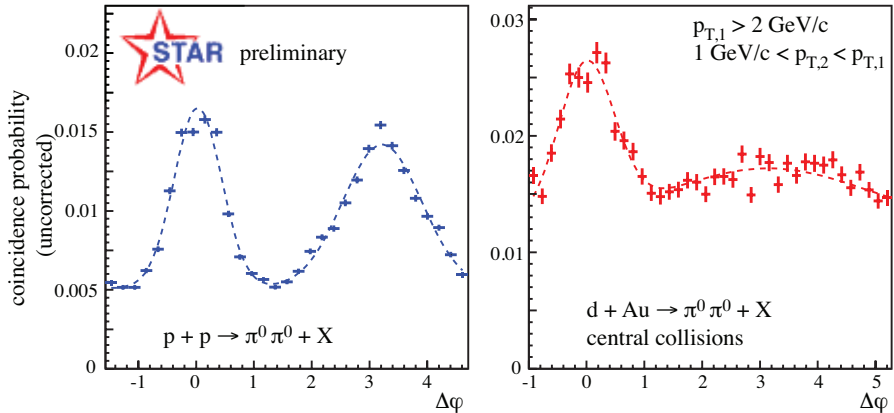


Fig. 13: Uncorrected coincidence probability versus azimuthal angle difference between two forward neutral pions in p+p (left) and central d+Au collisions (right).

As discussed above, correlation measurements allow to constrain the kinematics and can provide quantitatively more precise information. In particular, the correlated pair yield nuclear suppression factor J_{AB} can be defined analogous to R_{AB} in Eq. 9 as [27]

$$J_{AB} = \frac{1}{\langle N_{\text{coll}} \rangle} \frac{\sigma_{AB}^{\text{pair}} / \sigma_{AB}}{\sigma_{pp}^{\text{pair}} / \sigma_{pp}} \quad (10)$$

where $\langle N_{\text{coll}} \rangle$ is the average number of binary nucleon collisions for the A+B centrality selection, and σ and σ^{pair} are the cross sections (or normalized yields) for the full event selection and particle-pair event selection, for A+B and p+p collisions.

The pair yield in the near-side peak ($\Delta\phi = 0$), as seen in Fig. 13, carries information about the fragmentation of a single jet, while the pair yield in the away-side peak ($\Delta\phi = \pi$), carries information about the frequency with which the hard process yields back-to-back pairs that satisfy the particular cuts on rapidity and p_T . So, for example, in the case of the quark-gluon Compton process, tight cuts on the p_T and rapidity of the isolated photon, and on the rapidity of the away-side jet or leading jet fragmentation hadron, allow to tightly constrain the x_2 and Q^2 of the hard-scattering process. Then, comparison of the pair yield in the away-side peak for

p+Pb vs p+p, using J_{pPb} , would allow to study the suppression of the Compton process for the selected x_2 and Q^2 . In the case of an isolated γ -jet coincidence measurement with such tight p_T and rapidity cuts, J_{pPb} , is expected to be essentially equal to $R_g^{Pb}(x, Q^2)$, the ratio of the gluon distribution of the Pb nucleus, to the nucleon gluon distribution

$$J_{pPb} \propto \frac{f_{a|p}(x_1)f_{b|Pb}(x_2)\hat{\sigma}_{ab \rightarrow cd}D_{4|d}(z_d)}{f_{a|p}(x_1)f_{b|p}(x_2)\hat{\sigma}_{ab \rightarrow cd}D_{4|d}(z_d)} \propto \frac{G_{Pb}(x_2, Q^2)}{g_p(x_2, Q^2)} = R_g^{Pb}(x, Q^2) \quad (11)$$

Therefore, studies of J_{pA} , for isolated γ -jet (or γ -hadron) coincidences with tight cuts on p_T and rapidity would allow to extract the nuclear gluon modification, as shown in Fig. 7, directly.

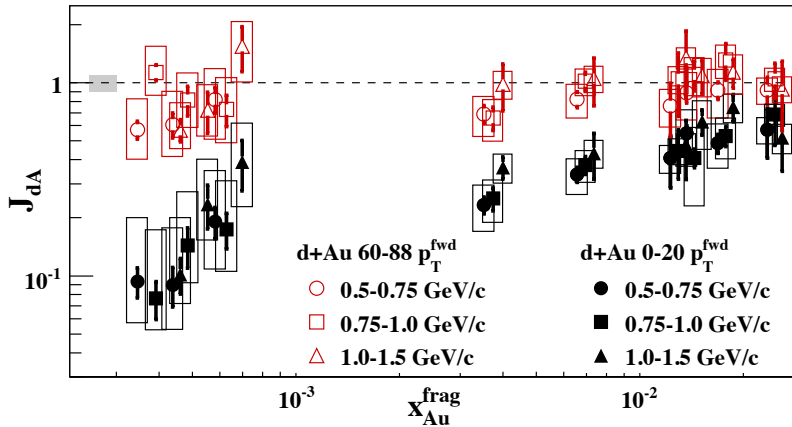


Fig. 14: The away-side pair nuclear suppression J_{dA} versus x_{Au}^{frag} for peripheral (60 – 88%) and central (0 – 20%) d+Au collisions at $\sqrt{s_{NN}} = 200$ GeV. The quantity x_{Au}^{frag} provides an (under) estimate of x_2 .

PHENIX has measured J_{dAu} of the away-side peak for correlations between neutral pion pairs for various centralities in d+Au collisions at $\sqrt{s_{NN}} = 200$ GeV, as shown in Fig. 14 [27]. The analysis has been performed for different selections on the p_T and rapidity of the pions, and is plotted against the x_2 -like quantity $x_{Au}^{frag} = (\langle p_{T3} \rangle e^{-\langle \eta_3 \rangle} + \langle p_{T4} \rangle e^{-\langle \eta_4 \rangle}) / \sqrt{s_{NN}}$. The quantity x_{Au}^{frag} is expected to provide an underestimate of x_2 , approaching x_2 in the case of a $2 \rightarrow 2$ process when the hadrons carry the full parton momenta ($z = 1, p_{T3} = p_{T4} = p_T$). The results of Fig. 14 show a suppression of J_{dAu} that increases strongly as x_{Au}^{frag} decreases for central d+Au collisions. Little or no suppression is observed for peripheral d+Au collisions. Once again, these observations are qualitatively in agreement with expectations from the effects of gluon saturation. It is interesting that the suppression is seen so strongly in the neutral pion correlations. However, the theoretical interpretation of this result is complicated by possible final state modifications, fragmentation uncertainties, and more generally, the very low values of transverse momentum studied. A similar analysis of isolated γ -jet or γ -hadron coincidences at the LHC offers the opportunity to quantitatively extract the nuclear gluon modification.

1.3 Medium properties in nucleus-nucleus collisions

Jet quenching, which dates back to original ideas from Bjorken in 1982 [28], has been established as a powerful tool to study the dense matter produced in heavy-ion collisions, and its

evolution. Hard (high Q^2) scatterings occur in the initial stage of a high energy nucleus–nucleus collision, producing high p_T partons that must traverse the surrounding matter generated in the collision before fragmenting in vacuum into a jet of hadrons. The scattered partons interact with the matter, losing energy through both radiative [29, 30, 31] and elastic interactions [32, 33, 34], with the magnitude of the energy loss strongly dependent on the density of the medium.

Jet quenching was first observed in the study of inclusive hadron suppression at RHIC. The inclusive yield of hadrons at high p_T , which are expected to originate from hard parton scattering, is suppressed in central heavy-ion collisions by a factor of ≈ 5 compared to expectations from p+p collisions [35, 36, 37, 38]. More directly, jet suppression is observed as a modification of the azimuthal angle correlation between hadrons. For a high- p_T hadron trigger there is a prominent away-side ($\Delta\phi = \pi$) correlation peak of hadrons associated with the recoiling parton (see Fig. 13). This away-side peak is much smaller in magnitude in central Au+Au compared to p+p or d+Au collisions [39, 40].

The observed non-suppression of photons in central Au+Au collisions [41], which do not interact strongly, together with the essential absence of suppression for hadrons in d+Au collisions [42, 43, 44, 45], where no significant amount of dense matter is produced in the final state (see Fig. 10), demonstrate that final state strong interactions must be responsible for the observed suppression of high energy hadrons in A+A collisions. The most likely interpretation of the suppression is thus medium-induced energy loss of fast partons.

Jet quenching has become a standard tool for the investigation of the hot and dense matter produced in heavy-ion collisions at RHIC, and more recently at the LHC. The first LHC measurements have already demonstrated the greater potential of jet quenching studies due to the factor of 30 increase in $\sqrt{s_{NN}}$ relative to RHIC, which provides a huge increase in the kinematic and statistical reach for hard probes. As an example, Fig. 15 shows the nuclear modification factor R_{AA} (see Eq. 9) measured by ALICE [46] for charged hadrons in central Pb+Pb collisions at $\sqrt{s_{NN}} = 2.76$ TeV for different centralities. The suppression shows a significant centrality dependence with the strongest effect at $p_T = 6 - 8$ GeV/ c for the most central collisions. R_{AA} is increasing towards higher p_T but is still significantly lower than 1 for $p_T = 50$ GeV/ c .

The interpretation of measurements of inclusive hadrons and hadron-pair correlations, is complicated by the uncertainties introduced by the fragmentation process, and also by surface biases. Recent studies using fully reconstructed jets from RHIC and the LHC avoid fragmentation issues to some extent. However, jet reconstruction is difficult in heavy-ion collisions due to the fluctuating underlying event. Also, the separation between jet components and energy lost to the medium is to some extent arbitrary. Prompt photons have a clear advantage as a means to trigger on recoiling jets. Direct photons produced in hard processes, through quark-gluon Compton scattering and quark-antiquark annihilation to first order (see Fig. 4), have transverse momentum that is balanced by that of the recoiling parton. The photon measurement thus provides a direct measurement of the parton momentum, allowing the energy dependence of the parton energy loss and fragmentation to be studied directly. Again, isolation cuts can ensure that higher order effects will play a minor role here. In particular, jet quenching studies at forward rapidities will be crucial to interpret other forward measurements sensitive to the dense medium, like that of

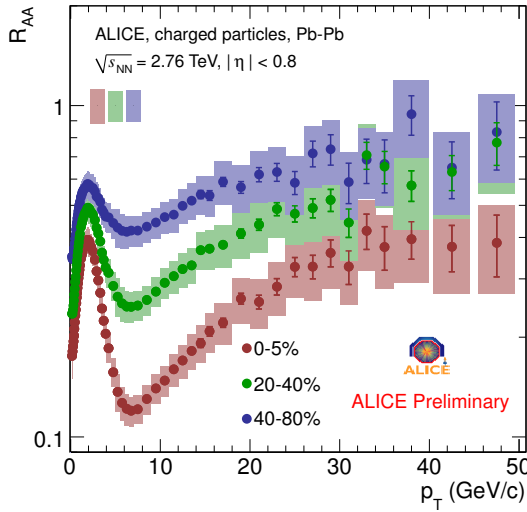


Fig. 15: Nuclear modification factor for charged hadrons in Pb+Pb collisions at $\sqrt{s_{NN}} = 2.76 \text{ TeV}$ for three different centralities from ALICE [46].

quarkonium suppression, as it will provide information on the longitudinal density profile of the matter.

The energy lost by the hard-scattered parton is expected to be carried by softer particles, and in fact di-hadron correlation studies at lower p_T show large qualitative differences between p+p reference measurements and Au+Au results. One particularly remarkable feature is the observation of a significant associated yield on the near side at larger pseudo-rapidity difference $\Delta\eta \gtrsim 0.7$, which is not expected from jet fragmentation. Figure 16 shows the distribution of associated hadrons with $2 < p_{T,\text{assoc}} < 3 \text{ GeV}/c$ in pseudo-rapidity η and azimuthal angle ϕ with respect to a trigger particle with $3 < p_{T,\text{trig}} < 4 \text{ GeV}/c$ in central Au+Au collisions at RHIC [47]. At these p_T , the associated hadrons show not only the jet-like peak around $(\Delta\eta, \Delta\phi) = (0,0)$, but also significant additional associated yield at larger $\Delta\eta$. The additional yield is approximately uniform in $\Delta\eta$, and the effect is therefore referred to as the *ridge*. The ridge-effect is strong in central heavy-ion collisions and is found to be present for trigger hadrons over a large p_T -range (up to at least $7 \text{ GeV}/c$) [47].

The long range of the correlation in $\Delta\eta$ very likely requires a production mechanism at work at very early times. A number of different possible mechanisms have been proposed, e.g. coupling of radiated gluons to longitudinal flow [48, 49, 50], medium heating by the passage of a hard parton combined with longitudinal flow [51] and a radial flow boost to the underlying p+p event, combined with trigger bias [52, 53]. Recently, it has been shown that azimuthal two-particle correlations in heavy-ion collisions can be well described by a Fourier decomposition and that the structures observed beyond the second order (v_2) are consistent with fluctuation in the initial state and a subsequent collective expansion [54].

A possibly related effect has been observed in high multiplicity p+p collisions at the LHC [55]. It is unclear, however, whether these phenomena share a common origin. Whatever the precise

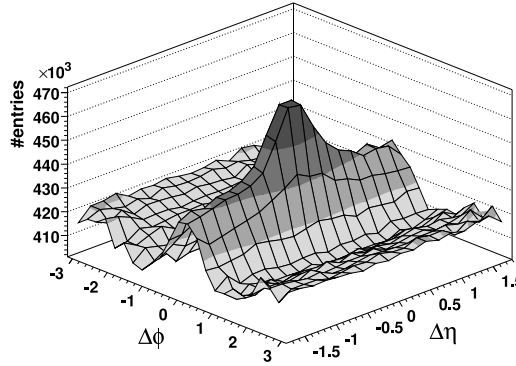


Fig. 16: Distribution of associated hadrons with $2 < p_{T,assoc} < 3$ GeV/c in pseudo-rapidity η and azimuthal angle ϕ with respect to a trigger particle with $3 < p_{T,trig} < 4$ GeV/c in central Au+Au collisions at RHIC [47].

mechanism that is responsible, the understanding of these correlations may shed light on the initial conditions in high-energy collisions. Long-range rapidity correlations involving prompt photons will be an important tool in these studies, because effects visible in prompt photons must relate to initial state effects, while hadron correlations will always be affected by final state modifications.

1.4 The physics case for a forward calorimeter in ALICE

The measurement of direct photons (and neutral mesons, and jets) at forward rapidity in a broad transverse momentum range will give access to unique physics in pp, pA, and AA collisions at the LHC. Forward measurements in general give access to small x parton distributions. The simplest measurements involve single hadrons, which however do not provide much constraint on the initial state kinematics, due the fragmentation process. Measurements of fully reconstructed jets provide better information, however jet measurements are generally feasible only for relatively large p_T and as such probe rather large Q^2 , a region that is not of greatest interest for studies of the modification of nuclear PDFs and the effects of saturation, which should be strongest at low to intermediate Q^2 . Photon measurements can be performed to lower p_T and thus probe the more interesting region of phase space.

The sensitivity of jet or photon measurements is illustrated in Fig. 17 with PYTHIA simulations. The figure shows x -ranges that inclusive measurements of jets or photons would be sensitive to, as a function of rapidity, for likely lowest feasible transverse momentum selections. It can clearly be seen that photon measurements are sensitive to smaller x due to the smaller p_T that can be reached. Single hadron measurements at p_T similar to the photon measurements will probe higher x ranges as they originate from fragmentation of jets of higher p_T .

As discussed above, and shown in Fig. 18, existing DIS and DY measurements with nuclei are limited to values of $x > 10^{-2}$, and measurements in d+Au at RHIC allow to reach to values up to $x \approx 10^{-4}$, albeit for very low Q^2 only. Measurements at the LHC have the potential to

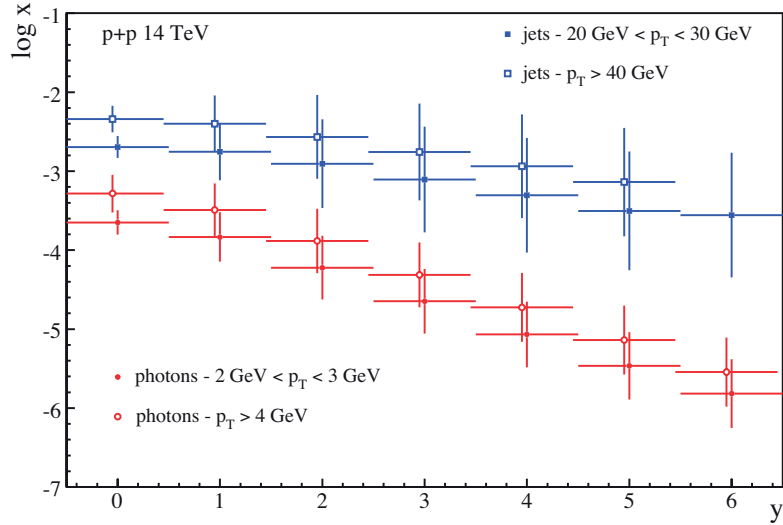


Fig. 17: Mean value of the smaller Bjorken- x (logarithmic scale) of the incoming partons for inclusive measurements of jets and direct photons as a function of the rapidity of the final state particle as calculated with PYTHIA 8 in p+p at 14 TeV. The horizontal bar on each point indicates the rapidity bin width (1 unit) and the vertical bar indicates the spread (1σ) of the corresponding x distributions.

extend the kinematic reach significantly. Measurements of hadrons, isolated photons, and jets with the present capabilities of the ALICE and CMS detectors will provide important additional constraints, as indicated in Fig. 18.

Direct photon measurements in the forward rapidity region with the FoCal detector in ALICE will allow to reach very low values of x in a range of small to intermediate Q^2 (see Fig. 17). Such a detector will add unique capabilities at the LHC to further constrain PDFs in the nucleon and in nuclei. In particular, it will allow measurements over a broad kinematic coverage around the saturation scale (see Fig. 18), which will be important to study the gluon saturation phenomena.

Table 1: Pseudorapidity ranges and granularity of existing forward calorimeters at LHC and the ALICE FoCal proposal.

	ATLAS Inner Wheel	CMS EndCap	LHCb ECAL	ALICE FoCal@3.5m	ALICE FoCal@8m
η range	2.5 - 3.2	1.5 - 3.0	1.8 - 4.3	2.5 - 4.5	3.3 - 5.1
granularity [deg]	5.7	0.5	≥ 0.18	≈ 0.016	≈ 0.007

Table 1 compares the specifications relevant for single photon identification with existing electromagnetic calorimeters at forward rapidity at the LHC, together with those of the proposed FoCal detector. As an example, the CMS endcap calorimeter extends to rapidity $\eta \approx 3$ and its cell size corresponds to an angular separation of $\Delta\psi \approx 0.5^\circ$ as seen from the nominal vertex. To identify the decay photons from a π^0 via reconstruction of two separate showers in such a detector requires a shower separation by at least two cells, which would limit the maximum

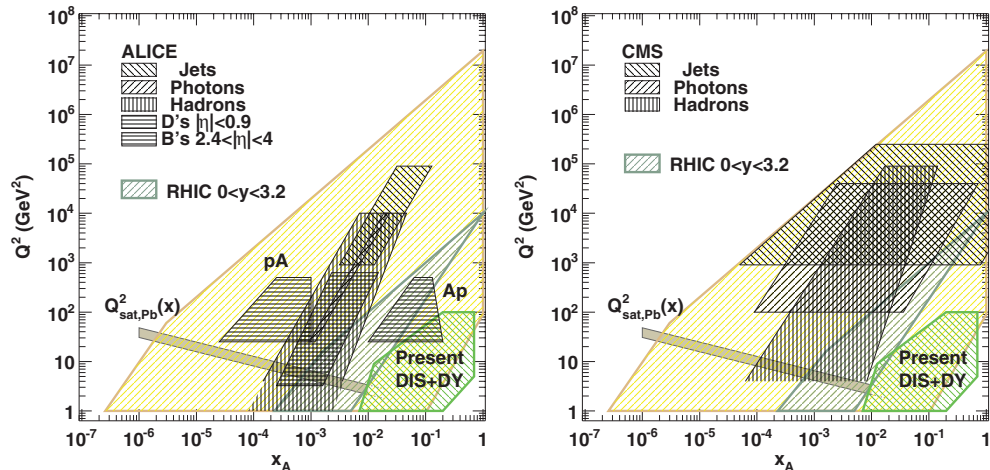


Fig. 18: Kinematic reach in x and Q^2 for $p+\text{Pb}$ collisions at $\sqrt{s_{NN}} = 8.8$ TeV at the LHC for 0.1 pb^{-1} integrated luminosity for jet, photon, and hadron measurements with the existing detectors of CMS (right) and ALICE (left) (from Ref. [18]). The region that can be studied by B meson measurements with the muon spectrometer of ALICE is also shown. Also shown is the kinematic region studied by DIS and Drell-Yan on nuclei, as well as in $d+\text{Au}$ collisions at RHIC. An estimate of the saturation scale Q_s^2 as a function of x is shown as the yellow band. Forward measurements by LHCb, may allow to reach small x , but may be limited in p_T coverage and capabilities for photon and jet measurements.

transverse momentum at $\eta = 3$ to below $p_T \approx 1.5 \text{ GeV}/c$. The LHCb experiment has electromagnetic calorimeter coverage to $\eta = 4.3$. The LHCb calorimeter has coarser cells, but sits at a much larger distance from the vertex, which provides a better angular granularity. This leads to a similar maximum transverse momentum for resolvable π^0 photons of $p_T \approx 1.5 \text{ GeV}/c$ at $\eta = 4$ for LHCb. In contrast, the same limit for pion rejection in the FoCal will occur at $p_T \approx 15 \text{ GeV}/c$ at $\eta = 4$. Furthermore, at the 8m location, the FoCal would provide two-photon separation up to similar p_T at $\eta \approx 5$ (see Fig. 27). While shower shape analysis will push the limit for statistical π^0 identification further out by a factor of ≈ 2 in each case, it is clear that the π^0 rejection capabilities of the FoCal detector with a design granularity of the order of 1 mm^2 leads to a two-photon separation capability that is better by an order of magnitude or more than the other LHC experiments.

The selectivity of the prompt photon measurement is further demonstrated in Fig. 19, which displays the inclusive cross section for measurements of low p_T photons in three rapidity intervals, as calculated with PYTHIA. Although the region of x that contributes for a particular kinematic selection is quite broad for an inclusive measurement, the region of maximum sensitivity is strongly dependent on the rapidity range, with values of $x < 10^{-5}$ dominating for inclusive prompt photon measurements in the rapidity region $4 < y < 5$ accessible with the FoCal in the 8m location.

For a $2 \rightarrow 2$ parton scattering process, such as the QCD Compton process, a coincidence measurement can more tightly constrain the kinematic selection on the initial partons, as discussed

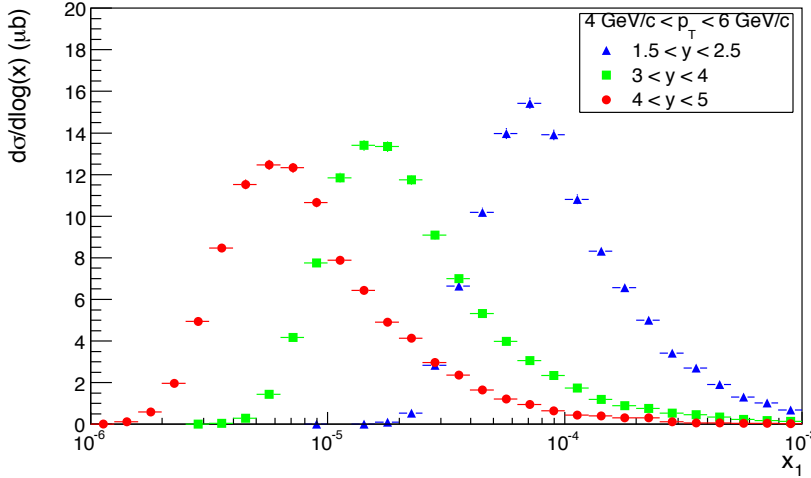


Fig. 19: Cross sections of inclusive direct photon production for different rapidity intervals as a function of the lower Bjorken- x of the incoming partons as calculated with PYTHIA 8 in p+p collisions at 14 TeV. The photon was constrained to have $4 < p_T < 6 \text{ GeV}/c$. The 3 regions of increasing rapidity roughly reflect the region of measurement (see Table 1) possible in CMS, LHCb or FoCal at 3.5m, or FoCal at 8m.

in Sec.1.1. Thus, measurement of the rapidity and p_T of the photon in coincidence with measurement of the direction (pseudo-rapidity) of the recoiling jet (or leading hadron) will constrain the rapidity of the recoiling parton, and allow to extract the x_1 and x_2 of the incoming partons, at leading order (see Eqs. 3 and 4). This is illustrated in Fig 20 which shows the $x_1 - x_2$ values probed by such measurements where the p_T and rapidities of the two outgoing partons can be reconstructed. It's seen that measurements of coincident pairs at low p_T in the forward region allow to probe the x region of $\sim 10^{-5}$, and below, at low Q^2 . Pair measurements at low p_T in the central ALICE detectors probe similar Q^2 , but at x values an order of magnitude greater. This region of higher x values is also probed by low p_T forward-central coincidences, but at higher Q^2 due to the rapidity separation, and correspondingly lower rate (see Fig. 17). High p_T coincidence measurements in the forward region will probe the same region of $x \sim 10^{-4}$ at still higher Q^2 , and lower rate. As has been discussed, the photon+jet measurements will provide the best means to investigate the low Q^2 regions, while the higher rate jet+jet measurements will provide the means to study the large Q^2 regions. Tight selections on the p_T and rapidity of the pairs will allow to more tightly constrain the x and Q^2 region that is probed.

Kinematic relations are less straightforward for fragmentation photons or other higher order processes, which become very important at the LHC, and are not included in the above estimates from PYTHIA. As discussed in Sec. 1.1, only 20 – 40% of the direct photons are produced in the leading order Compton process with the majority produced from fragmentation processes (see Fig. 5), which complicates the simple leading order kinematic interpretation. However, isolation cuts can efficiently suppress fragmentation photons, as shown on the right hand side of Fig. 5,

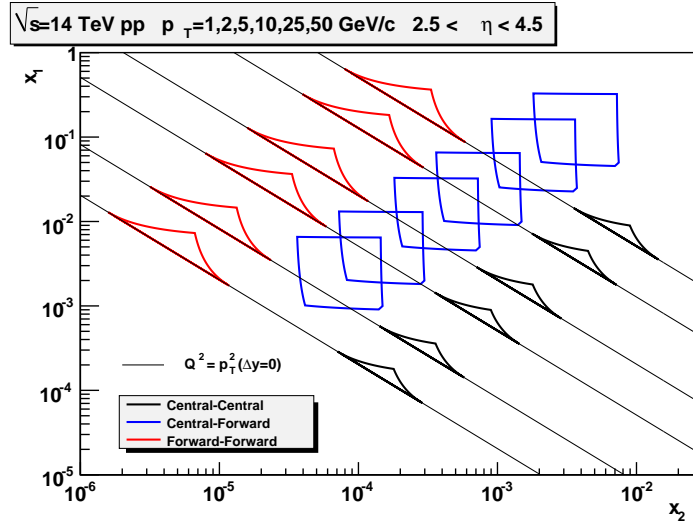


Fig. 20: Correlation in x_1 and x_2 of the incoming partons, for selections on the rapidity and p_T of the outgoing partons of a $2 \rightarrow 2$ parton scattering process for $p+p$ collisions at 14 TeV. The correlation is shown for coincident pairs in the forward region $2.5 < y < 4.5$ (red curves), or both in the ALICE central region $-0.7 < y < 0.7$ (black curves), or for forward-central coincidence pairs (blue curves) for p_T selections of 1 (lowest x values), 2, 5, 10, 25, and 50 (highest x values) GeV/c . For each p_T selection the curves define the $x_1 - x_2$ limits (i.e. region of coverage) for measurements of the outgoing particles at the y_{\min} and y_{\max} acceptance limits of the detectors. For the forward and central pair acceptance regions, the portion of the curves with $\Delta y = 0$ fall on the $Q^2 = p_T^2$ lines (Eq. 5).

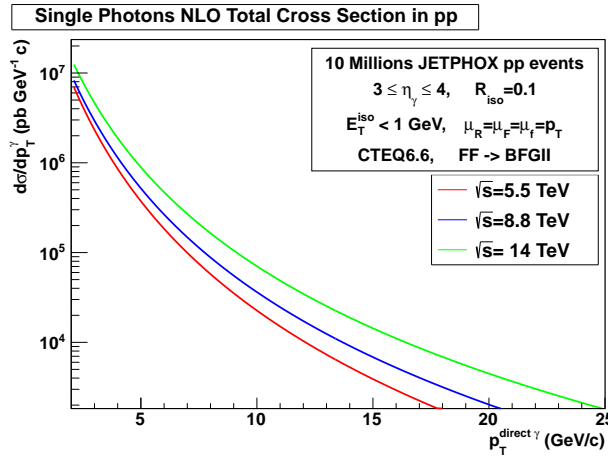


Fig. 21: QCD predictions of the inclusive isolated direct photon cross section for $p+p$ collisions at $\sqrt{s} = 5.5, 8$, and 14 TeV calculated at NLO using the JETPHOX package Ref. [57].

with the result that isolated photons are dominantly produced in the leading order Compton process.

Predictions of the inclusive direct photon cross sections in p+p collisions $\sqrt{s} = 5.5, 8$, and 14 TeV from NLO pQCD calculations [57] are shown in Fig. 21. The expected ALICE integrated luminosities for Pb+Pb, p+Pb, and p+p collisions at each of these energies are listed in Table 2. For the foreseen integrated parton luminosities (i.e. taking into account the nuclear mass A-scaling) and the planned FoCal acceptance of full azimuthal coverage over about 2 units of rapidity, it's expected that the integrated direct photon yield will be similar for the different systems with more than 10^3 photons per GeV/c for p_T of up to about $50 \text{ GeV}/c$.

Table 2: Assumed ALICE integrated luminosity per yearly run period (3 years for Pb+Pb). The parton luminosity is assumed to scale as the product of the nuclear masses of beam A and beam B.

System	Integrated Luminosity (pb^{-1})	A^*B	Integrated parton Luminosity (pb^{-1})
p+p 14 TeV	6	1	6
p+Pb 8.8 TeV	0.05	208	10
Pb+Pb 5.5 TeV	0.01	208^*208	430

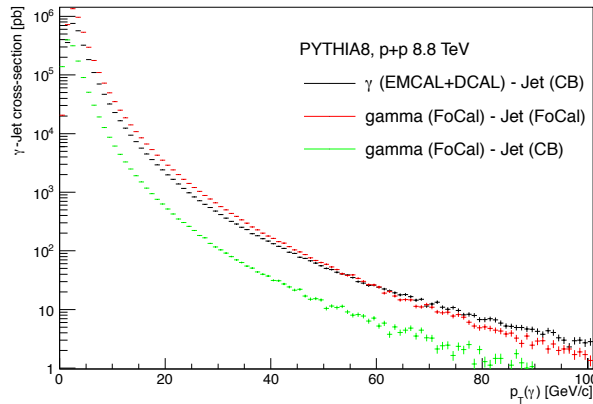


Fig. 22: The gamma-jet coincidence cross section calculated with PYTHIA 8 for 8.8 TeV p+p collisions for different combinations of FoCal and/or the ALICE central barrel (CB). The shift of the *cms* corresponding to a shift of $\Delta y \sim 0.47$ for p+Pb collisions has not been taken into consideration.

The baseline acceptance of FoCal will provide significant rate for gamma-jet coincidence measurements. Fig. 22 shows the gamma-jet coincidence cross section for different detector combinations with photons measured either in the central barrel calorimeters (EMCal, DCal, PHOS with $|\eta| < 0.7$, $0^\circ < \phi < 167^\circ$) or in FoCal ($2 < \eta < 4.3$, $0^\circ < \phi < 360^\circ$) and jets measured in the tracking detectors of the central barrel ($|\eta| < 1$, $0^\circ < \phi < 360^\circ$) or in FoCal. The calculations are shown for 8.8 TeV p+p collisions. As noted above, the expected integrated parton luminosity for p+Pb collisions is $\sim 10 \text{ pb}^{-1}$. Measurements of both photon and jet in the FoCal provide similar yields to a measurement using only the central barrel. For measurements of

photons in FoCal and jets in the central barrel the coincidence yield is somewhat lower, but still significant. As the direct photon identification at forward rapidities is expected to be feasible to lower p_T compared to the mid-rapidity measurement due to the boost, this measurement will be particularly interesting at low p_T . In studies of parton energy loss using photon-jet correlations the kinematics of the recoil jet is well constrained in LO processes, as the parton has to balance the transverse momentum of the photon. However, as discussed above, higher order processes, which become more important for large rapidity separation, will obscure this relation. Still, isolation cuts on the photon will also help here to reduce higher order contributions.

The integrated yield estimates for γ_{dir} and jet processes above a p_T^{min} are shown for Pb+Pb 0-10% central collisions at $\sqrt{s_{NN}}=5.5$ TeV in Fig. 23. The estimates were obtained with Pythia 6.4 simulations at the partonic level¹ assuming the integrated luminosities shown in Table 2. From that we estimate the kinematic reach, defined by requiring 1k events for $p_T > p_T^{min}$, for inclusive jet and γ_{dir} production at $3 < \eta < 4$ (left panel). The kinematic reach for all systems is summarized in Table 3. Analogously, we estimate the kinematic reach for coincidence measurements γ_{dir} -jet and jet-jet at forward rapidities (F-F) (integrated over $\eta = 3 - 5$) and forward–mid-rapidity ($|\eta| < 0.7$) (F-M)², shown for Pb+Pb 0-10% central collisions in Fig. 23 (right panel), and summarized for all systems in Table 3.

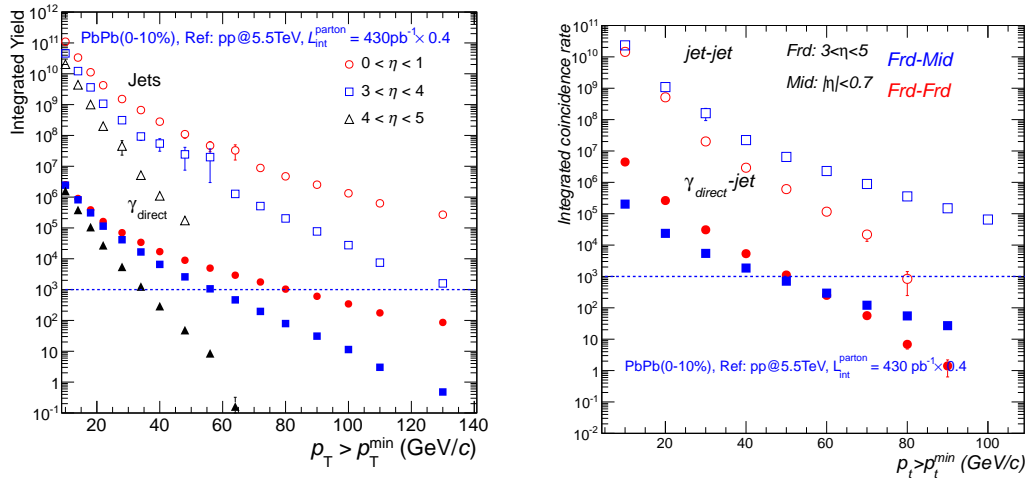


Fig. 23: Integrated yield estimates above p_T^{min} in Pb+Pb 0-10% central collisions at $\sqrt{s_{NN}}=5.5$ GeV. Left: Inclusive jet and γ_{dir} for different η bins. Right: Jet-jet and γ_{dir} -jet coincidence rates at forward-forward (F-F) and forward-mid-rapidity (F-M) ($|\eta| < 0.7$).

For the lighter p+p and p+Pb systems, the rates for the F-M γ_{dir} -jet coincidence measurements are kinematically limited to around 20 GeV, whereas the F-F γ_{dir} -jet correlation measurement is feasible up to 30 GeV, sufficient to reach a high enough Q^2 to be unambiguously in the perturba-

¹Pythia simulations including a jet-finding algorithm and comparisons to NLO calculations will be performed in the near future.

²For these rate estimated we assumed 2π at mid-rapidity ($|\eta| < 0.7$). With the present EMCal/DCal azimuthal coverage the rates will be reduced by a factor of approximately 2. The current rates would reflect coincidence measurements with charged only jets in the TPC.

System	\sqrt{s} [TeV]	γ_{dir}^{max} [GeV]	Jet p_T^{max} [GeV]	Coinc. Type	γ_{dir} -Jet p_T^{max} [GeV]	Jet-Jet p_T^{max} [GeV]
p+p	14	35	110	F-M	20	> 100
				F-F	30	70
p+Pb	8.8	40	120	F-M	20	> 100
				F-F	30	70
Pb+Pb (0-10%)	5.5	60	130	F-M	50	> 100
				F-F	50	80

Table 3: Kinematic reach p_T^{max} [GeV] defined as an integrated yield of 1k for the inclusive γ_{dir} and jet measurements (for $3 < \eta < 4$) as well as for γ_{dir} -jet and jet-jet coincidence measurements for forward-forward rapidity (F-F) (integrated over $\eta = 3 - 5$) coincidences and forward–mid-rapidity (F-M) coincidences.

tive QCD regime, important to map out experimentally the transition from pQCD to saturation dominated physics. For the coincidence measurements the inclusion of the hadronic calorimeter is crucial to be able to extend the kinematic leverage by enabling the jet-jet coincidence measurements F-M > 100 GeV and F-F up to 70 GeV.

In Pb+Pb collisions (0-10% central) the kinematic reach for inclusive and coincidence measurements (γ_{dir} and jet) is sufficiently high to perform these measurements even in the presence of the heavy-ion background, a non-trivial complication in jet and γ_{dir} reconstruction in heavy-ion collisions.

In summary, direct photon measurements at forward rapidity are an ideal observable for the investigation of parton distributions at small x , and in particular to study effects such as gluon saturation in p+p and p+Pb collisions. Photon-jet coincidence measurements will allow to constrain the initial state kinematics more precisely than inclusive photon or jet measurements. In addition, the measured p_T of the photon in a photon-jet coincidence measurement provides the initial p_T of the outgoing recoil parton and can thus contribute to parton energy loss studies in Pb+Pb collisions.

Furthermore, the kinematic conditions at forward rapidities have a distinct advantage for photon measurements. While photons of a given p_T will deposit very high energy easily measurable in a calorimeter, the energy deposited by hadrons carrying a similar p_T will typically be concentrated around minimum ionization, and in general at a relatively much smaller energy. The irreducible background from these particles to photon detection will be much smaller than for a comparable measurement at mid-rapidity, and the systematic uncertainty of direct photon measurements is thus potentially smaller at forward rapidity compared to mid-rapidity for the same transverse momentum.

However, direct photon measurements suitable for these studies are extremely challenging. At very high p_T isolation cuts should allow to obtain a pure sample of direct photons. Going somewhat lower into the intermediate range ($p_T < 10\text{GeV}/c$), photon identification via isolation cuts will likely not be sufficient and neutral meson identification and rejection on an event-by-event basis will be crucial to obtain a clean prompt photon signal. For these, the very large lab

momenta imply very small opening angles of the two decay photons in particular from a π^0 (see Fig.27), and the ability to resolve the decay photons will require very high granularity going significantly beyond the capabilities of existing experiments.

2 Conceptual Design

2.1 General Design Considerations

The measurement of direct photons at large rapidities over a large range of transverse momentum is the main observable necessary to achieve the desired physics goals enabled by the FoCal detector, and is the driving force in its design. The photon detector – an electromagnetic calorimeter – must be able to discriminate single photons from neutral pions at high energy, which requires high granularity. Furthermore, it should cover a large part of the pseudorapidity region $\eta > 3$ and enable the direct photon measurement over a broad range of transverse momentum.

The rapidity region opposite the ALICE muon spectrometer is ideally suited to be adapted to an ALICE forward direct photon detector upgrade. To cover the largest rapidities possible and simultaneously keep the particle density to a tolerable level it is preferable to move to a large distance from the interaction point. The preferable option will thus be the location of a high performance FoCal-E electromagnetic calorimeter at about 8m from the IP, which is as far downstream as reasonably feasible. This option would in addition enable the installation of a hadronic calorimeter immediately behind the FoCal-E. Another possibility, with minimal modification to the ALICE setup would be to replace the existing Photon Multiplicity Detector with the FoCal-E. This installation option is shown in Fig. 24. Because of its simplicity the latter option has been studied first, also in this document, but from the result of these studies is considered the second best solution.

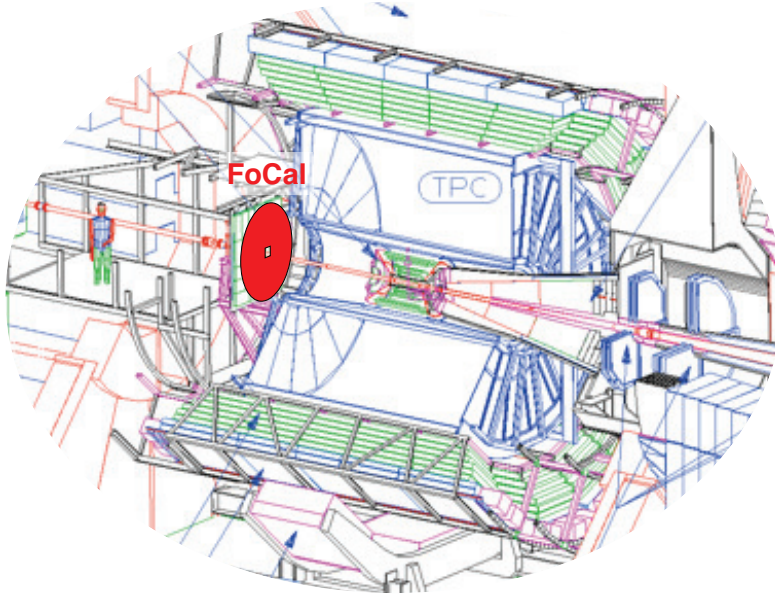


Fig. 24: Setup of the ALICE experiment with the FoCal-E at a possible location opposite the muon arm at a distance of 3.5 m from the interaction point, presently the location of the PMD.

The range of acceptance in pseudorapidity of the FoCal depends on its physical location: for a given minimum radial distance from the beam the z -distance from the interaction point directly

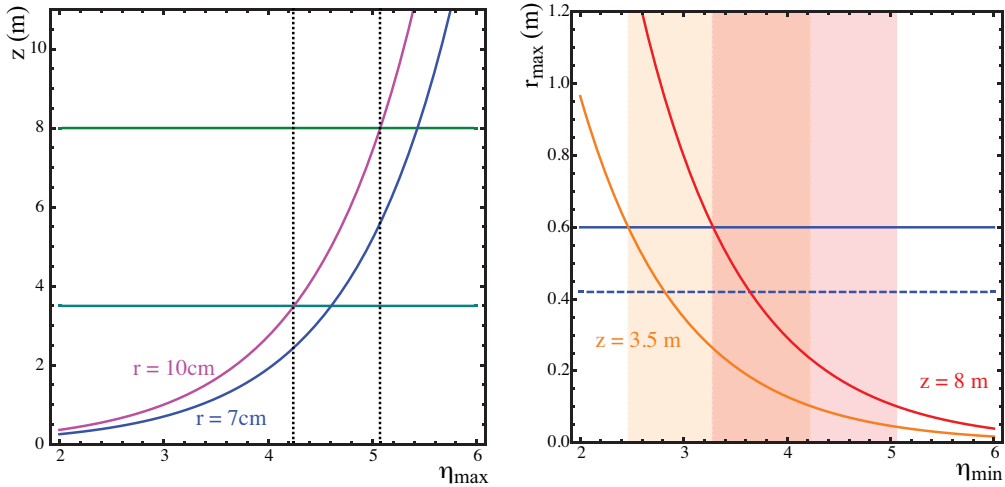


Fig. 25: Left: z -distance as a function of maximum pseudorapidity for two minimal radial separations from the beam. Two potential positions in z are indicated as horizontal lines. Right: Outer radius of the detector as a function of the minimum pseudorapidity for two values of z . Two possible radii are also shown. The shaded areas indicate the possible η -coverage of the two potential geometries.

limits the maximum pseudorapidity η_{\max} . The left hand side of Fig. 25 shows the relation between η_{\max} and the distance z . As the default configuration the FoCal could be positioned at a distance of 8 m. For this position and an inner radius of 10 cm a value of $\eta_{\max} = 5$ could be reached. In the alternative scenario, placing the detector at a distance of $z = 3.5$ m (replacing the PMD in the current ALICE setup) would shift the coverage under similar conditions down to $\eta_{\max} = 4.2$. The left hand side of Fig. 25 displays the dependence of the required outer radius on the minimum pseudorapidity η_{\min} . For a detector at $z = 8$ m an outer radius of $r = 0.6$ m would cover up to $\eta_{\min} = 3.3$, while the same detector at $z = 3.5$ m would reach $\eta_{\min} = 2.5$.

An important consideration for photon measurements at large η (i.e. small θ) is the dramatic increase in the amount of material that particles traverse on straight-line trajectories from the IP to the detector. Fig. 26 shows the conversion probability in an Al beam pipe as a function of pseudorapidity. At the possible maximum pseudorapidities the probability reaches values of ≈ 0.2 ($\eta = 4.2$) and ≈ 0.4 ($\eta = 5$). Although these conversion probabilities are significant, they will occur very close to the detector, from highly boosted photons, and so may not distort the photon showers in the FoCal-E as much as one might naively think. The effects of beam pipe materials have fully been taken into account in the performance simulations presented in this document. Other materials in front of the FoCal, which are particularly relevant for the larger z -distance, are under investigation - from the status of the discussion it appears that a reduction of the currently existing material budget to a tolerable level will be possible, but will require a reworking of some of the existing structure in the experiment.

For optimal performance at forward rapidities in the environment of a high areal density of particles incident on the detector, and in particular for γ/π^0 discrimination, a highly granular lateral segmentation of the FoCal-E is required. To achieve this, a material of small Molière

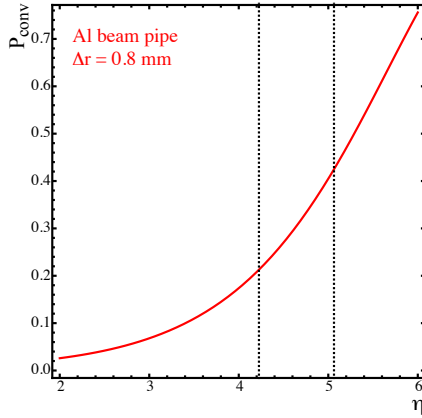


Fig. 26: Probability for photon conversion in an Al beam pipe of 0.8 mm wall thickness as a function of η . The maximum η values for the two FoCal options under consideration are indicated as vertical lines.

radius R_M should be used, and the sensitive part of the detector should have very fine granularity.

The most effective way to enhance the selection of direct photons is to reject the background photons from 2γ decay of the π^0 and η by measurement of the decay photons and rejection of both photons when their invariant mass reconstructs to that of a π^0 (or η). The ability to measure both photons and perform an invariant mass rejection, at a given p_T , improves dramatically at forward rapidity due to the focussing effect on the acceptance as the π^0 is boosted, as shown in Fig. 27. On the other hand, for the same reason the separation between the photons decreases with increasing energy and rapidity to the point that the two decay photon showers can no longer be resolved, after which the two decay photons are indistinguishable from a single photon, setting an upper p_T limit for direct identification of the decay photons. As presented below, the FoCal-E will be designed with the capability to identify showers with separation as small as a few mm, allowing to identify symmetric ($\alpha = 0$) π^0 decays up to ~ 300 GeV/c, or ~ 750 GeV/c, π^0 momentum at the 3.5 m, or 5 m, location options, respectively, as seen in Fig. 27. The large acceptance and fine granularity will allow efficient rejection of decay photons to allow the direct photon measurement over a large range of rapidity and transverse momentum.

Isolation cuts must be employed at high transverse momenta when the decay photons can no longer be resolved and identified efficiently. Isolation cuts are also necessary to discriminate between prompt QCD-Compton single photons and fragmentation photons. To further improve the direct photon measurement with the FoCal it should also allow efficient isolation cuts. A hadronic section of the forward calorimeter would further enhance the efficiency of isolation cuts, and would additionally allow to measure the hadronic energy of jets to provide added capability for jet measurements.

The FoCal should have good energy resolution and linearity. With the boosted forward kinematic conditions an intrinsic energy resolution term for the FoCal-E of better than $\sigma_0 \sim 20\%$ would be sufficient for the photon and neutral meson measurements of interest. Similarly, an intrinsic resolution for the FoCal-H of better than $\sigma_0 \sim 70\%$ would be sufficient for the isolation

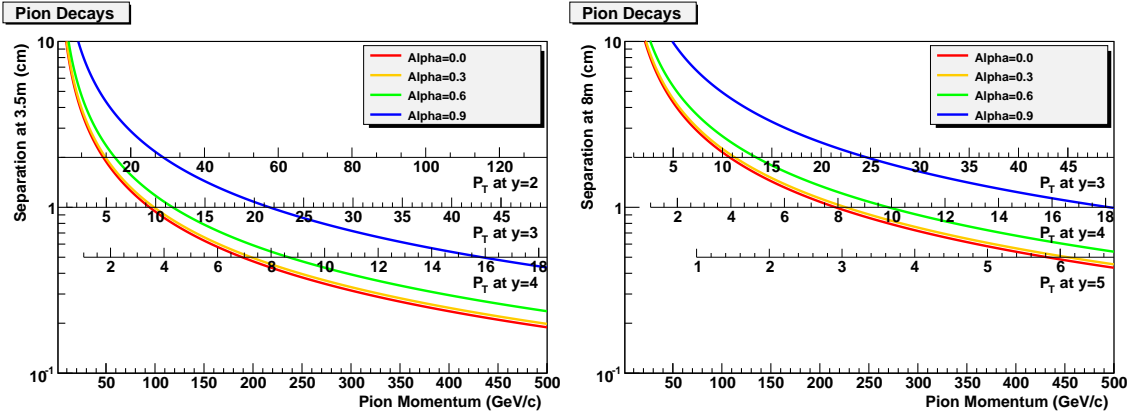


Fig. 27: Separation distance in cm between the two photons from π^0 decay, as a function of the total pion momentum, for varying decay asymmetries, $\alpha = |E_{\gamma_1} - E_{\gamma_2}| / |E_{\gamma_1} + E_{\gamma_2}|$, at 3.5 m (Left), or 8 m (Right), from the decay vertex. As a reminder, the π^0 decays are uniform in α with e.g. 90% of the π^0 decaying with $\alpha < 0.9$. The transverse momentum corresponding to the total momentum is shown for various rapidities. For η decays the momentum scales would be scaled by the η/π^0 mass ratio.

requirements and jet measurements.

Fulfilling the above requirements for the direct photon measurement will also allow measurements of

- neutral mesons (π^0 , η , ω etc.) and
- fully reconstruct jets (with FoCal-H).

While these measurements will certainly be possible in p+p and p+A collisions, the most important systems for the study of gluon saturation, the high granularity should also make measurements in Pb+Pb collisions possible. However, because of the high particle density in A+A collisions, the FoCal performance will be degraded by overlapping shower effects with the result that some measurements will be limited to a higher region of transverse momentum than in p+p or p+A.

2.2 The FoCal Design

Since the intrinsic energy resolution requirements of the FoCal are very moderate, a sampling calorimeter design is well-suited for both the electromagnetic and hadronic detector components of the FoCal.

2.2.1 The FoCal-E Design

For the electromagnetic calorimeter a small shower size is essential to minimize occupancy effects and to optimize the photon shower separation. Therefore, tungsten is the absorber material of choice due to its small Molière radius R_M and radiation length X_0 , with values of

$$R_M = 9 \text{ mm}$$

and

$$X_0 = 3.5 \text{ mm}.$$

In order to maintain a compact electromagnetic calorimeter with small effective Molière radius and to implement a fine lateral granularity readout the FoCal-E has been designed as a Si+W sampling calorimeter. Since the energy resolution requirement for the FoCal-E is not very stringent, a rather coarse sampling layer thickness of $\approx 1 X_0$ has been chosen to minimize cost.

The transverse cell size should at most be of the order of R_M , however, simulations show that a granularity as fine as ~ 1 mm is still useful for π^0 identification. High granularity will in addition enhance the capabilities to resolve multiple hits in a high multiplicity environment. However, employing the minimum cell size in all layers and reading them all out independently leads to a prohibitively large data volume and would dramatically increase the cost. Longitudinal segmentation adds further capability for particle identification and background rejection. Therefore the design under consideration has longitudinal segments with cells of moderate size summed longitudinally, interspersed with layers with very high granularity.

The FoCal-E detector will consist of a Si+W sampling calorimeter hybrid design using two different Si readout technologies:

1. low-granularity layers (LGL) with transverse cell sizes of $\approx 1 \text{ cm}^2 \approx R_M^2$, which are combined longitudinally into segments, and
2. high-granularity layers (HGL) of an effective granularity of $\approx 1 \text{ mm}^2$, i.e. much smaller than the Molière radius, read out independently.

The schematic view of the longitudinal structure of the FoCal-E is shown in Fig. 28. All layers will consist of W sheets of $\approx 1 X_0$ followed by active silicon sensors. Fig. 28 shows a FoCal-E structure with 3 LGL segments, each longitudinally summed and independently read out, with 2 HGL layers interspersed at sampling layers 5 and 10. The preferred number and location of HGL is still under investigation, but the configuration shown in Fig. 28 is likely to be close to the optimal design. Placement of the HGL layer(s) close to the shower maximum would profit from the larger signal height, however, the position of the shower maximum is energy dependent, and furthermore it fluctuates from event to event. In addition, electromagnetic showers develop a broader distribution at large depths, such that the position resolution, and in particular the two-shower separation capability may be better at a depth smaller than at the shower maximum. Therefore, there may not be a single optimal location for the HGL and having 2 HGL layers allows to alleviate these effects.

The favored option for the silicon sensors in the HGL is that of monolithic active pixel sensors (MAPS). As these are based on CMOS technology, they will be relatively cheap. The most advanced technological route can provide binary signals from pixels of sizes down to $20 \times 20 \mu\text{m}^2$. In our present design we envisage an on-chip processing of the binary signals to count the number of pixel hits within logically constructed macro-pixels, or mini-pads, of $1 \times 1 \text{ mm}^2$. These mini-pad counts are then used as effective signals for the HGLs.³

³Other effective pad sizes and other data reduction algorithms will also be investigated.

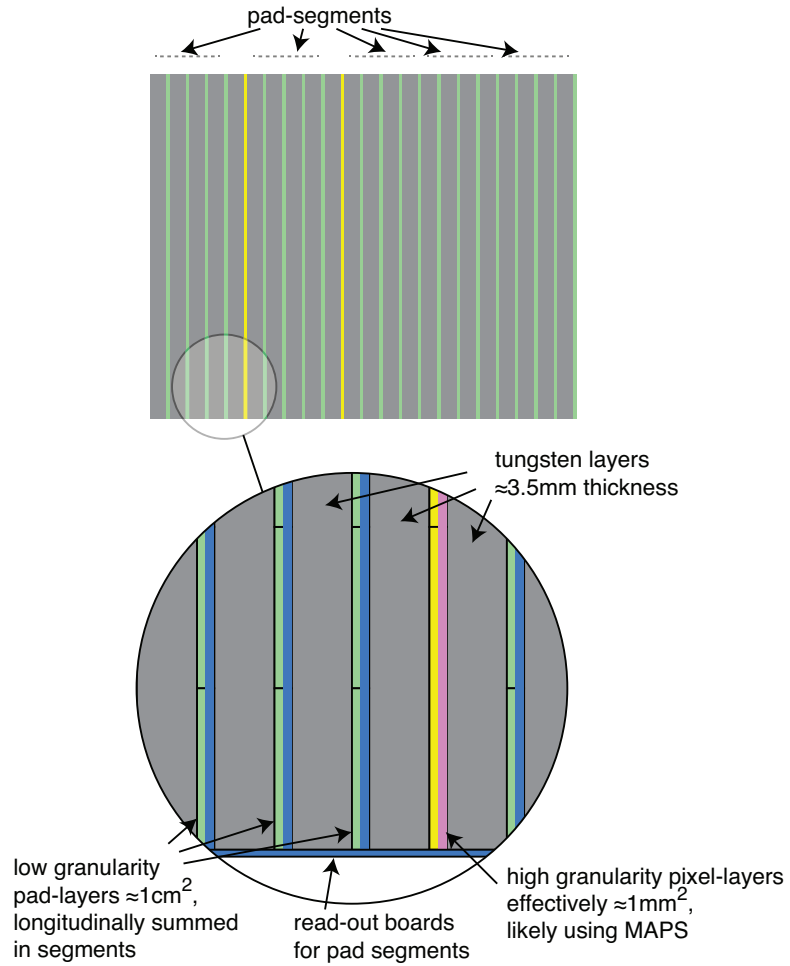


Fig. 28: Schematic view of the longitudinal structure of the FoCal-E detector.

The MAPS readout is intrinsically slow and cannot provide a trigger signal, which will likely be desirable in p+p collisions, where the interaction rate will be high. Secondly, while their envisaged integration time, in the range of $5\mu\text{s}$, should be short enough to properly separate different events in Pb+Pb collisions with maximum interaction rate of $\sim 50\text{ kHz}$, pile-up will occur in p+p collisions where interaction rates of 200kHz or higher are envisaged. These effects will be disentangled by matching clusters in the HGL and LGL layers in position and time.

The LGL will use conventional silicon pad sensors. It is foreseen to sum the analog signals of pads at the same transverse location from different layers within a segment. The sum signals would be routed out of the detector and digitized. The LGL readout will also provide trigger capability. Section 5 gives further details on the construction and readout of the FoCal-E.

2.2.2 The FoCal-H Hadronic Calorimeter Design

Optionally, the electromagnetic calorimeter of FoCal (FoCal-E) will be complemented with a hadronic calorimeter (FoCal-H), which would significantly improve both photon isolation and jet measurements. Ideally, the FoCal-H should cover the same range in pseudorapidity as the FoCal-E. It should be located as close as possible behind the FoCal-E to minimize the FoCal-H size, and to avoid blow-up of showers which start in the FoCal-E. Due to support and access constraints, it appears that the most feasible location to install a FoCal-H would be at a distance of $\sim 10\text{m}$ from the IP, in the present location of the ALICE compensation magnet. This will require modification of some of the general infrastructure in the ALICE experimental cavern, including movement of the compensation magnet to a new location. This then argues for the location of FoCal-E to be moved further downstream from the IP close to FoCal-H, i.e. to a distance of $\sim 8\text{m}$. Practical consideration for the FoCal-H installation therefore favor the "8 m" option for the FoCal geometry. The installation of the FoCal-E and FoCal-H is indicated in Fig. 29.

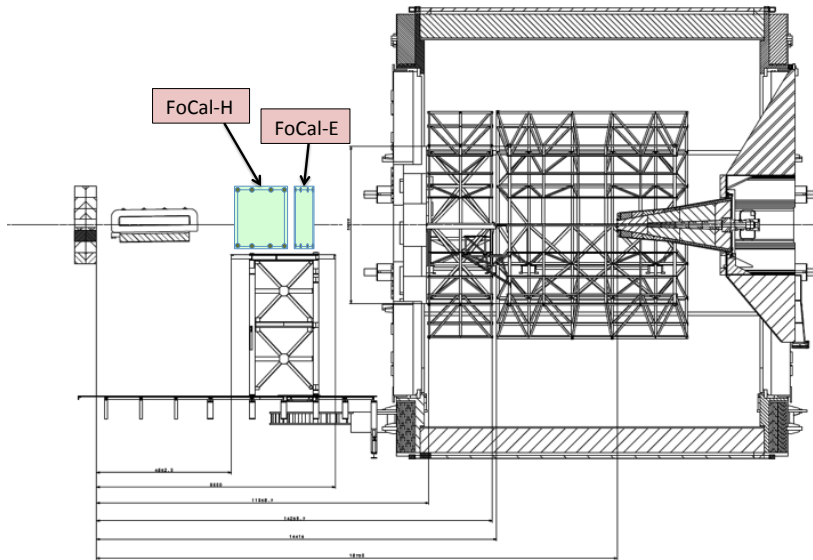


Fig. 29: Installation of the FoCal at 8m location with FoCal-H detector included.

FoCal-H would be built as a conventional sampling hadronic calorimeter with a total thickness of $\sim 8\lambda_{\text{had}}$ and an extent of $\Delta z \sim 1.5\text{m}$. The detector would be of similar size as FoCal-E. With outer dimension $r \sim 0.7\text{m}$ the total weight would be $\sim 15\text{t}$. While FoCal-H would consist of relatively conventional technology, the weight and size impose constraints on the location and support structure. Section 5 gives further details on the construction and readout of the FoCal-H.

2.3 The FoCal Configuration for Simulations

A realistic evaluation of the FoCal performance with respect to its capabilities for rejection of decay photons and possible degradation of performance due to various backgrounds requires a full GEANT simulation of the detector response, with realistic implementation of a complete analysis chain, including cluster and shower finding algorithms, with optimization of the decay photon rejection algorithm. These procedures are still evolving. The details of the methods that have been implemented for the Monte Carlo studies presented in this document are described in Sec. 3.1.

The algorithms have been developed, and results will be shown, for MC simulations of the FoCal-E longitudinal structure shown in Fig. 28. The detector begins with a segment of four LGL (Seg0) with the pad signals from the four consecutive layers summed analytically to form a pad-sized tower for the segment, followed by a HGL (Seg1) which is located at a depth of $5X_0$. The next two segments again consist of four LGL summed (Seg2) and a HGL (Seg3). The rest of the detector is made of 10 LGL combined into two equal segments (Seg4 and Seg5). Depending on the performance limits for very high energy photons the total thickness of the detector can be increased to minimize shower leakage.

The FoCal implemented in the simulations has an approximately circular hole of 8 cm radius around the beam pipe, and covers a radial distance up to $r = 0.8\text{ m}$. MC studies have been performed for both location options.

The most important difference between the two locations is the rapidity coverage; the placement at $z = 8\text{ m}$ moves the rapidity coverage by 0.8 units of rapidity more forward compared to the $z = 3.6\text{ m}$. In the common rapidity range, $3 < \eta < 4$, the particle density per unit area in the detector will be smaller for the $z = 8\text{ m}$ position than for the $z = 3.6\text{ m}$ position.

At fixed radial distance from the beam pipe, the particle density per unit area is rather independent of the position of the detector, so that the density in the most forward regions ($\eta = 4.5$ for $z = 3.6\text{ m}$ and $\eta = 5.3$ for $z = 8\text{ m}$) is similar in both cases.

The FoCal-H has not yet been included in the full GEANT description of the FoCal – its performance is included via a parameterised response, which is considered sufficient for the purpose of this document.

3 Standalone Performance

3.1 MC simulation and analysis algorithms

For the performance studies presented in this document we have implemented the FoCal detector design described above in the GEANT3 based ALICE detector simulation software package, ALIROOT v4-20-Rev-32. The details of the implementation and the single particle standalone performance of the FoCal are described in this section. The simulated performance in full physics events is described in the next section.

3.1.1 GEANT3 Model

For the design studies of the FoCal it has been implemented with uniform azimuthal coverage over the radial region from 8 cm to 80 cm. The two different locations have both been investigated: at $z=360$ cm from the ALICE IP corresponding to a pseudorapidity coverage from $2.5 < \eta < 4.5$, and at $z=800$ cm to $3.3 < \eta < 5.3$. It is constructed as a Si+W sampling calorimeter consisting of 50 identical layers each having the composition given in Table 4, and each being approximately one radiation length thick (only 20 layers ($20X_0$) have been used in the analyses presented here).

Table 4: Single sampling layer composition in GEANT3 implementation of FoCal.

Volume	Material	Thickness [cm]
Wolfram	Pure W	0.35
Glue	G10	0.05
SiPad	Silicon	0.05
Glue	G10	0.05
Wiring	Cu	0.01
Gap	Air	0.05
Total		0.56

Hits are stored from the "SiPad" volumes in a mesh of $100 \mu\text{m} \times 100 \mu\text{m}$ unit size. The LGLs (Low Granularity Layers) and HGLs (High Granularity Layers) are then implemented in the FoCal digitizer by summing the mesh into a coarser pad structure (e.g. $1 \times 1 \text{ cm}^2$ pads for LGLs and $1 \times 1 \text{ mm}^2$ pads for HGLs), and summing pads longitudinally in the LGL segments to implement the tower structure. This implementation allows to explore different configurations/parameters of LGLs and HGLs using the same set of simulation data. The results presented here have been performed with the readout structure shown in Fig. 28 and described in Section 2.3 with 2 HGLs of 1 mm pad size at layers 5 and 10 (i.e. at $5X_0$ and $10X_0$).

3.1.2 AliROOT configuration

The single-particle simulations were done with the existing ALICE detector (including only parts relevant for the forward region FoCal studies). For PYTHIA simulations, a slightly modified version of the AliROOT simulation package has been used to allow to trigger on interesting events. PYTHIA simulations were done with the full ALICE setup.

3.2 Analysis framework

The first step of the analysis is the digitization of hits. This is performed within the analysis framework (not the ALIROOT simulation framework) to allow to study different combinations/parameters of the LGLs and HGLs, as described above.

The LGL implementation follows the classic pad response where the signal is proportional to the deposited energy in the volume. That is, the signals from all $100 \times 100 \mu\text{m}^2$ mesh-pixels within a $1 \times 1 \text{ cm}^2$ LGL pad are summed. The LGL pad signals are then summed longitudinally to form the digitized LGL pad tower signals.

The HGL implementation is done according to the MAPS design where the signal in the $100 \times 100 \mu\text{m}^2$ mesh-pixel is first converted to a binary "hit" digit which is then summed for all mesh-pixels within a $1 \times 1 \text{ mm}^2$ HGL pad. Due to memory limitations, a $100 \times 100 \mu\text{m}^2$ mesh-pixel size is used rather than the current MAPS sensor pixel size of $20 \times 20 \mu\text{m}^2$.

An example of the simulated response of the FoCal to a high energy π^0 is shown in Fig. 30. The simulated signals on the two HGL pad layers are shown for a 200 GeV π^0 . The clusters of the two photons from the π^0 decay are clearly identifiable even though the cluster centroids are only $\sim 5 \text{ mm}$ apart. This suggests that it should be feasible to use the high granularity cluster information to identify and reject the decay photons to high energies. It is also apparent that the tail of the photon shower is diffused when viewed with high spatial granularity. The cluster algorithm must take into account those hit pads in the diffuse tail of the shower, so as to include them in the total cluster energy and avoid to create fake low energy photons from pad clusters in the tail of the shower. At the same time, the algorithm must resolve the two showers in order to identify them as π^0 decay photons.

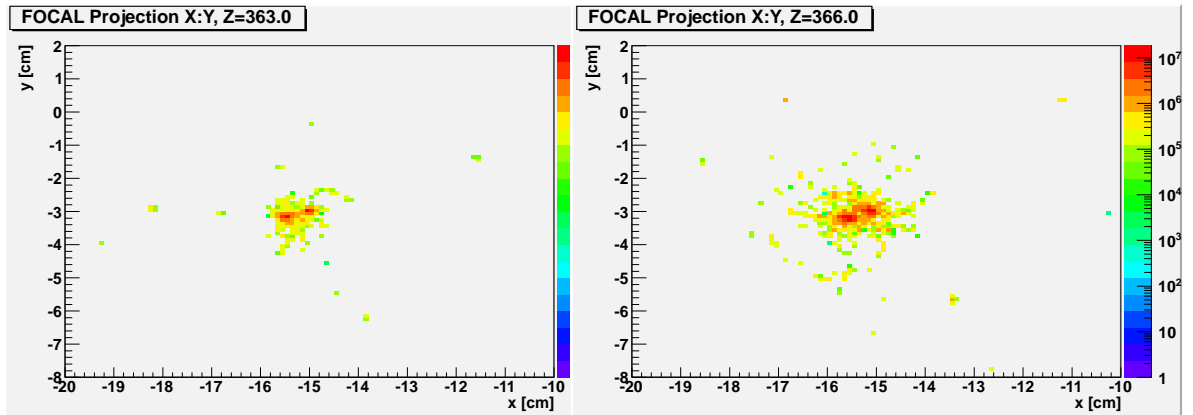


Fig. 30: The FoCal response to a single π^0 of 200 GeV incident energy on the High Granularity Layers at $5X_0$ (left) and at $10X_0$ (Right).

3.2.1 Clustering algorithm

The next step in the analysis chain is the clustering of the digitized information on each readout pad plane. A custom algorithm has been developed to handle the significant fluctuations within

a shower as seen on the high granularity layers. The algorithm also must deal with the high occupancy of the AA environment. The same algorithm is also used for the low granularity layers. The algorithm parameters may be tuned for optimum performance depending on the granularity and occupancy.

The cluster algorithm specification and parameters (for each readout segment) are the following:

1. Search for cluster seeds on an energy-sorted list of digits from the segment.
2. Digit must be above a minimum energy (SeedThreshold) to become a seed.
3. Digits within cluster radius (MaxRing) of a higher energy seed are included in cluster.
4. Cluster seeds cannot be closer than a minimum separation distance (MinRing).
5. Create, merge, and split clusters based on weights assigned by seeds to all nearby digits.
6. Weights are calculated using a shower shape "weighting function":
 - (a) Shower shape is approximated by a Cauchy-Lorentz function with squared exponential tail.
 - (b) Input: SeedEnergy and Distance of digit from the seed.
 - (c) Shower shape parameters are extracted from single-photon events for each segment separately.

Each segment can be handled separately. It is also possible to give a list of pre-seeds - positions where to expect clusters. Seeds created in such a way cannot be rejected. For HGL segments, we used segment 1 to get a list of pre-seeds, for the LGL segments we used segment 2.

The algorithm is very fast - $O(n)$, but requires the digits to be sorted, which is $O(n \log(n))$. Its advantage is that it splits/merges clusters as it creates them, based on the definition of the weighting function, which is tuned to reproduce the shape of an electromagnetic shower. The drawback is the many parameters that it uses (Min/MaxRing, RejectionRatio, SeedThreshold, and 2 parameters for the weighting function).

3.2.2 Shower reconstruction algorithm

After the clusters have been found on each of the segments, it is necessary to determine which clusters on each segment belong to the same shower, and to combine those clusters to determine the total energy of the shower and its position. An iterative algorithm is used to combine information from different segments. This algorithm first loops over LGL and then HGL segments separately and finally combines LGL and HGL to find the final clusters. If more than one cluster is found on a HGL segment within a single cluster on a LGL segment, the LGL segment cluster is split into the corresponding number of HGL clusters, with energy partitioned according to the relative energies of the clusters found on the HGL segment. The total shower energy is obtained

as the sum of all longitudinal segments of the matched clusters. The final shower position is calculated as the average of the two HGL segment positions.

It should be noted that the above algorithms and their parameters, which are described in more detail in appendix A, may be optimized differently for different analysis purposes. For the purpose of the π^0 and η yield analyses, which would be performed on a statistical basis by extraction of the integrated yield of the mass peak in the photon-pair invariant mass distributions, after subtraction of the underlying combinatorial background, the efficiency and resolution of the clustering algorithm would be emphasized, while effects that would create additional combinatorial background would not be of significant concern. On the other hand, for the purpose of efficient identification of non-decay photons on an event-by-event basis the clustering algorithm must minimize the production of fake background, as from shower tails, in order to minimize the rate at which photons are falsely attributed to be one of a decay photon pair, and falsely rejected as a prompt photon.

The FoCal simulation studies to date have emphasized the investigation and optimization of the FoCal towards efficient identification of prompt photons since this is the most important and most challenging task for the FoCal. Although the optimization of these algorithms is still in progress and further improvements may be expected, the algorithms already demonstrate a satisfactory performance, as demonstrated by the results shown below. These algorithms will be used in upcoming studies to confirm the optimization of the FoCal-E detector design, in particular with respect to the number and locations of the High Granularity Layers.

3.3 Single photon reconstruction

The performance of the FoCal detector and reconstruction algorithm has been evaluated using simulated events with single particles (photon or π^0). The simulations incorporate the full geometry of ALICE, including the material of the beam pipe, and the T0 and VZERO detectors which are currently mounted in front of the nominal FoCal location.

Figure 31 shows the photon reconstruction efficiency as a function of the generated photon energy using the clustering algorithm parameters optimized for the prompt photon identification. The reconstruction efficiency is unity for photons with energy $E_\gamma > 10$ GeV, with a drop in efficiency for lower energies.

Figure 32 shows the FoCal-E energy resolution for single photons with the design described above with 20 sampling layers. The energy deposited in the active volume of the Low Granularity readout layers has been summed, while the energy deposited in the two HGL's has been neglected.⁴ The energy resolution can be parametrized as:

$$\frac{\sigma(E)}{E} = \sqrt{\left(\frac{\sigma_1}{\sqrt{E}}\right)^2 + \sigma_0^2}$$

with $\sigma_1 = 20.7\%$ and $\sigma_0 = 1.1\%$ obtained for the fit to the simulation data shown by the curve in Fig. 32.

⁴A possible improvement of the energy resolution from including the HGL's will be investigated in the future.

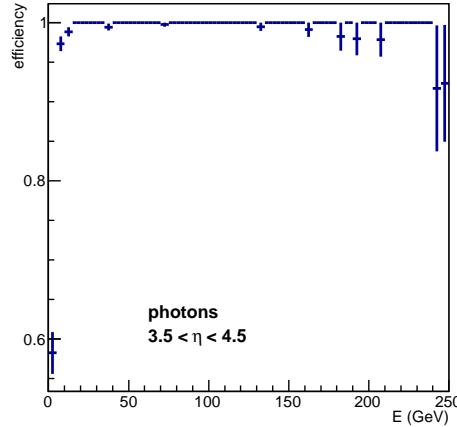


Fig. 31: Efficiency for photon detection as a function of generated photon energy.

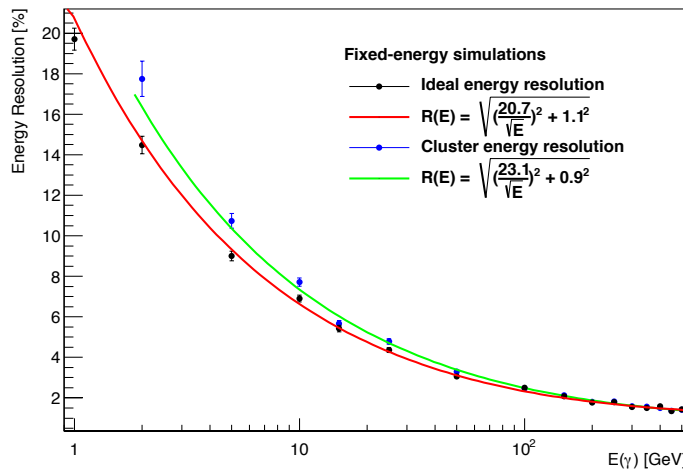


Fig. 32: The FoCal-E energy resolution as a function of photon energy obtained without clustering algorithm by summing the deposited energy on all 20 layers, excluding the two High Granularity Layers. The fit parameters $\sigma_1 = 20.7\%$ and $\sigma_0 = 1.1\%$ are obtained. The energy resolution obtained with the clustering algorithm used for the present analysis is shown by the blue points and is seen to provide a worsened energy resolution at low energy ($\sigma_1 \sim 23\%$).

Figure 32 also shows the FoCal-E energy resolution obtained using the cluster algorithm and parameters that have been used for the prompt photon identification in the results presented below. It's observed that this cluster algorithm provides a moderately degraded energy resolution than could optimally be obtained. As discussed in the previous section, this suggests that the

potential exists to further improve the cluster algorithm, which will certainly be done for the π^0 and η yield analyses.

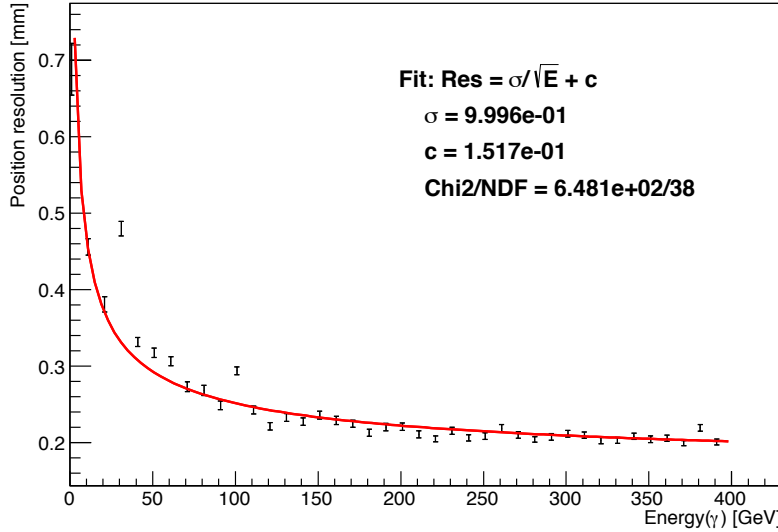


Fig. 33: The photon shower position resolution in the transverse coordinate as a function of the photon energy.

The photon shower position resolution in the transverse coordinate of the FoCal-E is shown in Fig. 33. The position is calculated from the cluster information on the High Granularity Layer segments alone ($1 \times 1 \text{ mm}^2$ pad size). The figure shows the σ of a Gaussian fit to the distribution of residuals between the calculated position and the known position of incidence of the photon (from MC) in the x-coordinate, then increased by $\sqrt{2}$ to represent the result for the transverse coordinate. The resolution is fit to the form:

$$\frac{\sigma(E)}{E} = \frac{\sigma}{\sqrt{E}} + c$$

with $\sigma = 1.0 \text{ mm}$ and $c = 0.15 \text{ mm}$ obtained for the fit to the simulation data shown by the curve in Fig. 33.

3.3.1 Photon identification

Electromagnetic showers from photons⁵ can be separated from other particles by using the characteristic energy deposition in the detector. Firstly, for a given incident particle energy, a photon will deposit essentially all of its energy in the electromagnetic calorimeter, while hadrons, like charged pions or protons, in general will deposit only a small fraction of their energy. This leads to a natural suppression of high energy hadrons in an electromagnetic calorimeter. In addition, hadrons can be further suppressed by employing cuts on the shape of the spatial distribution of the deposited energy shower. In particular, with the FoCal-E we will make use of

- the lateral width of the shower, and
- the longitudinal distribution of deposited energy as measured in the different longitudinal segments.

Figure 34 shows the lateral and longitudinal shower shape variables for clusters from direct photons, decay photons, and hadrons (charged pions) for two different selections on the cluster transverse momentum from fully simulated PYTHIA p+p events with $\sqrt{s} = 14$ TeV. The upper four panels show lateral shower widths (major and minor axis). The shower widths are calculated using only information from the low-granularity layers. It can be seen in the figure that the lateral shower width for hadron showers is larger than for direct photons, as expected. Moreover, the clusters from decay photons show a larger width than direct photons. A cut on the latter shower shape will therefore remove hadronic showers as well as decay photons.

The lower two panels of Figure 34 show the distribution of the ratio of the energy deposited in segment 5 (layers 16–20) to the energy in segments 2 and 4 (layers 5–9 and 11–15), which is a measure of the longitudinal energy distribution. It can be seen that this ratio is smaller for electromagnetic showers (both direct and decay photons) than for hadrons. A cut on this ratio will therefore reduce the hadronic contribution to the measured clusters.

Figure 35 illustrates the effect of the cuts on these shower shape parameters via the relative contamination of non-photons in the cluster samples as a function of cluster p_T . Already without any additional cuts, the contamination, which originates dominantly from hadrons, is suppressed, because for these forward measurements the p_T values correspond to relatively high energies, which are very infrequently reached by the deposited energy of hadrons. Shower shape cuts are useful to reduce this contamination even further. Starting from a contamination of the order of 10%, both cuts individually reduce this significantly, the combined application of both cuts leads to a contamination of 3–4%.

⁵If not explicitly indicated, all identification arguments about photon showers apply almost equally well to electrons and positrons, we will therefore use the term *photon* here as implying any electromagnetic shower and will not always specifically mention electrons and positrons.

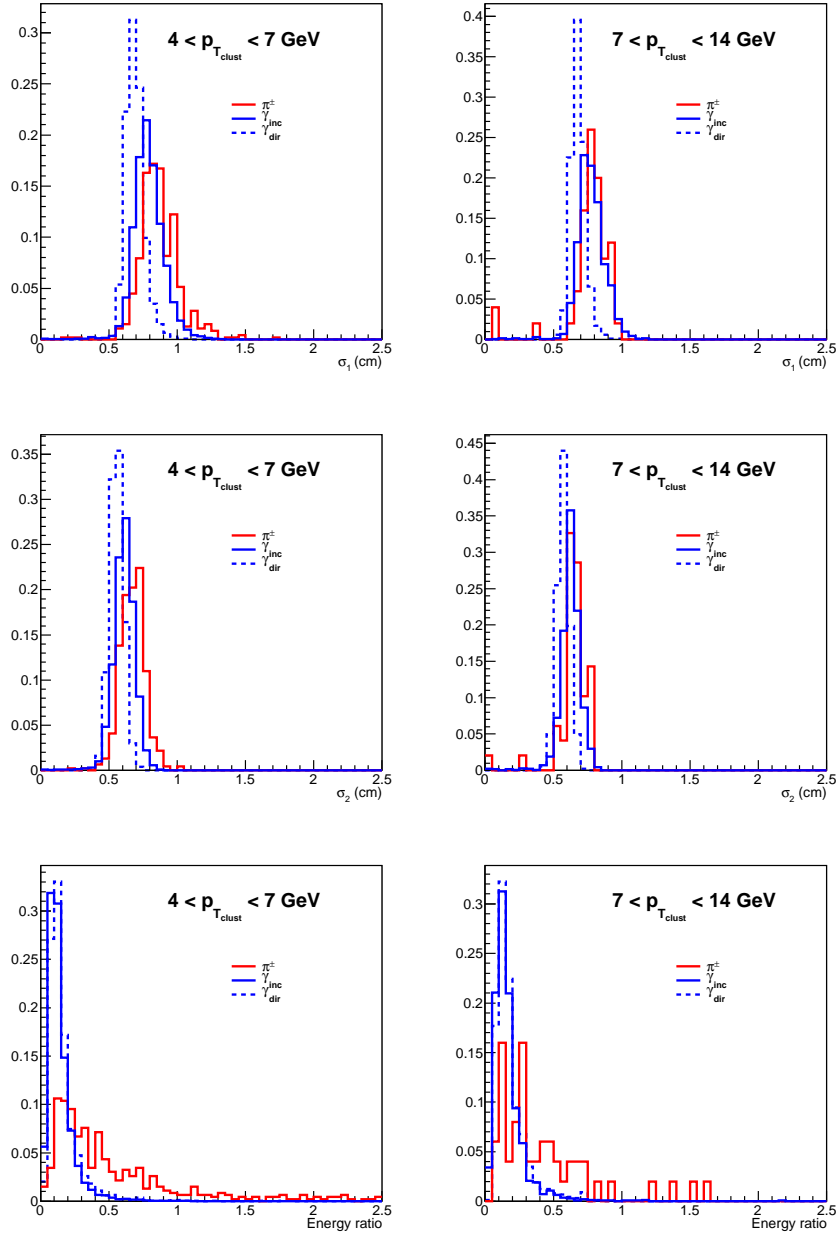


Fig. 34: Shower shape distributions for reconstructed clusters from direct photons (dashed blue), decay photons (solid blue), and charged pions (solid red) for two different selections on reconstructed p_T : $4-7 \text{ GeV}/c$ (left panels) and $7-14 \text{ GeV}/c$ (right panels). Upper panels: width σ_1 along major shower axis. Middle panels: width σ_2 along minor shower axis. Lower panels: longitudinal energy ratio (energy deposited in segment 5 divided by energy deposited in segments 2 and 4).

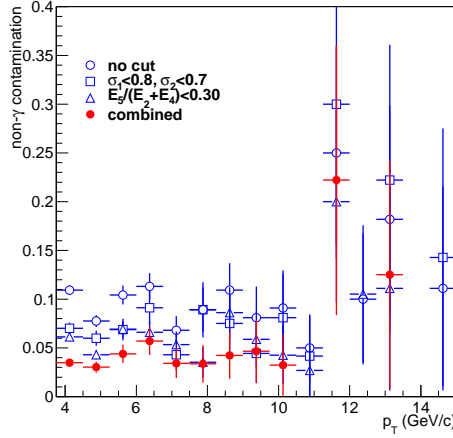


Fig. 35: Contamination of the photon sample (fraction of clusters from non-photonic origin), as a function of p_T , before and after shower shape cuts.

3.4 Neutral meson reconstruction

Examples of the reconstructed photon-pair invariant mass distributions for simulated single π^0 's of incident energies of $100 < E < 150$ GeV and $200 < E < 250$ GeV are shown in Fig. 36. The π^0 mass peak is clearly observed, despite the high incident energy of the π^0 and the close proximity of the photon showers which have spatial separations of ~ 1 cm or less (see Fig. 27). For these energies the two photons are not resolved as separate showers in the LGL segments. Instead, the two photons are identified in the HGL segments and the energy of the single cluster measured with the LGL segments is partitioned to the two photons according to the asymmetry of the two HGL clusters.

The p_T dependence of the π^0 mass peak and its width are shown in Fig. 37 for simulated single π^0 's in the nominal FoCal acceptance. The calculated mass is observed to drop with p_T , while the resolution increases slightly. In particular the decrease in the position of the mass peak is a sign that the cluster finding and cluster splitting algorithm has not been optimised for π^0 measurements yet. While these observations demonstrate the capabilities of pion reconstruction and allow to estimate a corresponding efficiency as discussed below, they also suggest that further improvements can be expected.

To enhance the sample of prompt photons, decay photons are to be identified and rejected on an event-by-event basis when they are found to reconstruct to a π^0 when combined with any other photon in the event. Fig. 38 shows the reconstruction efficiency for single π^0 's as a function of the π^0 energy (left panel) and transverse momentum (right panel). A π^0 is considered to be reconstructed if at least two clusters are found and at least one pair of clusters has a reconstructed invariant mass of $0.07 < m_{rec} < 0.18$ GeV. The π^0 identification efficiency is observed to drop at low energy, or p_T , due to loss of acceptance to find both photons in the FoCal with cluster energies sufficiently large to be identified efficiently (see Fig. 31), and drops at high energy, or

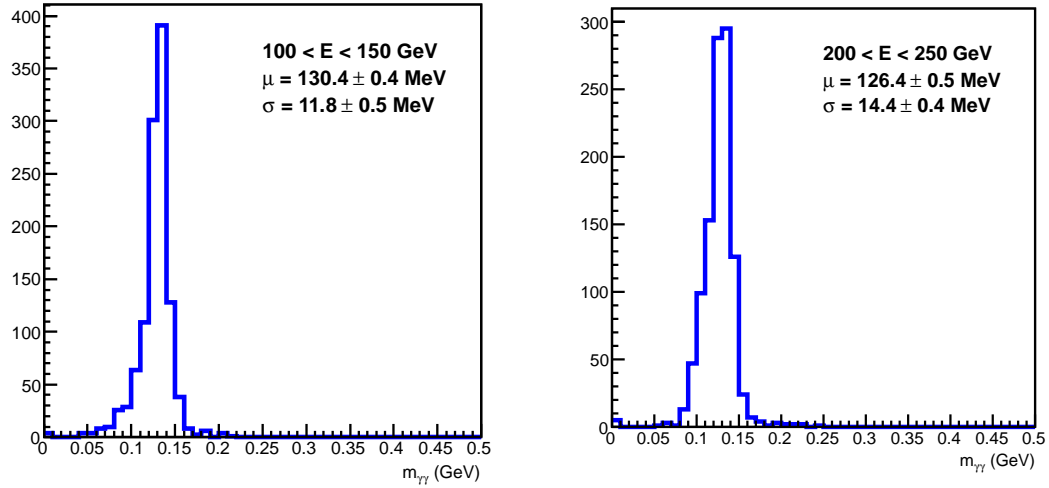


Fig. 36: Invariant mass distribution of reconstructed cluster pairs from simulated π^0 decays. The listed values for the mean μ and width σ are determined from a gaussian fit to the measured peak.

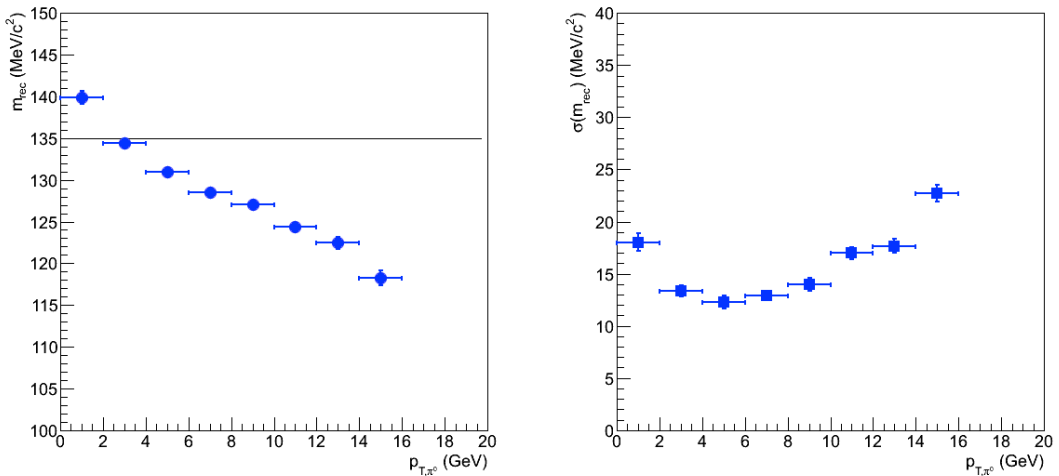


Fig. 37: Fitted mean value (left) and resolution (right) of the invariant mass peak for neutral pions as a function of the pion energy.

p_T , when the two photon clusters are no longer resolvable in the HGL segments.

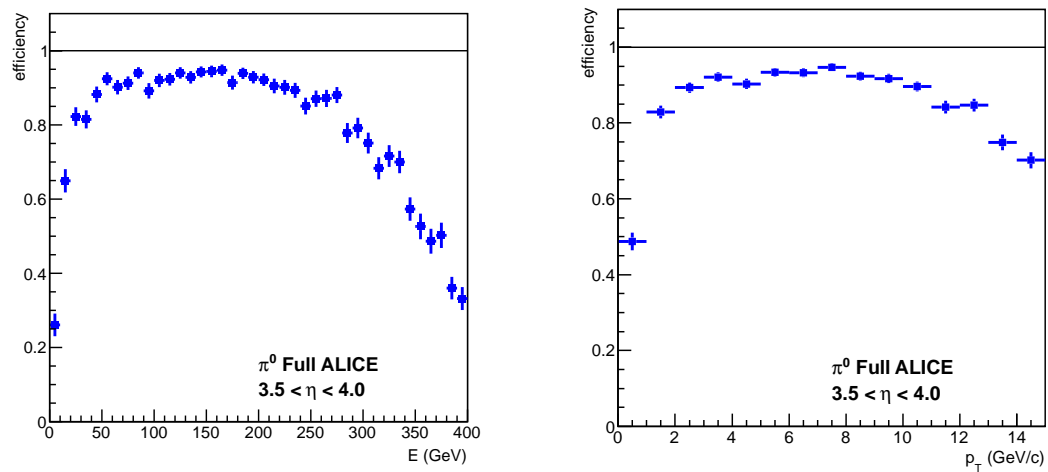


Fig. 38: Efficiency for neutral pion identification as a function of pion energy (left) and transverse momentum (right). The inefficiency includes the loss of π^0 's due to acceptance (i.e. are not identifiable because one or both photons are not in the FoCal acceptance).

4 Performance in p+p, p+A, and Pb+Pb

4.1 Efficiency in p+p

The performance of the FoCal with realistic event backgrounds was studied using PYTHIA p+p events at $\sqrt{s} = 14$ TeV. The particles were transported through the full ALICE detector setup using GEANT3 and the standard ALICE simulation software in AliRoot with the addition of the FoCal simulation geometry.

Two scenarios were investigated:

- **FoCal at 8m**

In this scenario the FoCal is positioned with the front face of the detector at $z = 800$ cm. With a radial coverage of $8 < r < 80$ cm, this gives a rapidity coverage of $3.0 < \eta < 5.3$.

- **FoCal at 4m**

In the other scenario, the FoCal is positioned at the location of the current PMD detector. The front face of the detector is at $z = 360$ cm. With a radial coverage of $8 < r < 80$ cm, this gives a rapidity coverage of $2.2 < \eta < 4.5$.

The full (current) ALICE detector is included in the simulation. The current beam pipe has a number of flanges and valves at $380 < z < 800$ cm. The existing material was found to give unacceptable backgrounds for the 8 m location. To a large extent this material can likely be removed or relocated to other positions, where it is not harmful. However, the reworking of the existing structures will require a significant amount of work and the solution may also impact the installation procedures of the inner detectors, so a careful study of the consequences is under way. After discussion with ALICE Technical Coordination it was decided for this document to remove the additional material from the simulation to study the feasibility of the more forward rapidity coverage that this location would make possible. The simulations thus performed should provide good performance estimates for solutions, where no significant structures in addition to the beam pipe will shadow the detector. Detailed simulations using the actually planned installation will be performed as soon as this is known.

For each case, a large sample of hadronic events was generated, based on the Pythia Minimum Bias settings. Events were selected to have at least one primary particle (charged hadron or π^0) or a (decay) photon with $p_T > 4$ GeV/c in the fiducial acceptance of the FoCaL before transporting them through the detector setup. A separate sample of direct photon events was generated using PYTHIA with the appropriate hard process selection (MSEL=10) and the same selection on the final state.

4.1.1 Direct photon yield expectations

The main simulation samples are based on PYTHIA events, which is based on leading order (LO) perturbative QCD with a shower Monte Carlo. However, it is known that there are significant next-to-leading order (NLO) corrections to the direct photon production cross section. For the final performance estimate, we therefore also use a NLO direct photon spectrum calculated using JETPHOX [15].

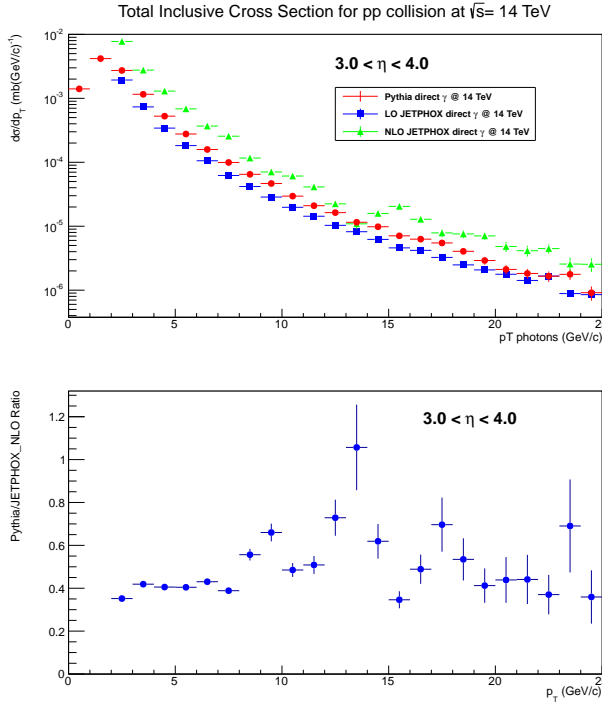


Fig. 39: Comparison of the direct photon spectrum from PYTHIA (LO) (red points) and JETPHOX both at leading order (LO, blue histogram) and NLO (green histograms) for p+p collisions at $\sqrt{s} = 14 \text{ TeV}$ for $3 < \eta < 4$. The lower panel shows the ratio between PYTHIA and JETPHOX.

Figure 39 compares the direct photon spectrum from PYTHIA and JETPHOX for p+p collisions at $\sqrt{s} = 14 \text{ TeV}$ and $3 < \eta < 4$. The difference between the calculated yields is about a factor 2.5, with little or no p_T -dependence. We will use both PYTHIA and JETPHOX predictions for the prompt photon signal, as representative of the uncertainty on the magnitude of the signal.

The JETPHOX NLO calculations are expected to be closer to reality than the PYTHIA predictions, which are based on LO calculations. This has been confirmed for p+p collisions at $\sqrt{s} = 7$ at high p_T , where measurements from ATLAS [14] and CMS [9, 10, 11] agree well with JETPHOX calculations.

4.1.2 FoCal at 4m

Figure 40 shows the transverse momentum spectrum of all clusters in PYTHIA simulation events for Minimum Bias p+p collisions at $\sqrt{s} = 14$. The clusters were matched to the nearest track. Most of the reconstructed clusters originate from photons from π^0 decays (red line). The contribution of hadronic showers is about 10% (dashed black line). The contribution of direct (non-decay) photons, shown by the red dashed curve, is small compared to the other sources of clusters.

The rejection of decay photons was implemented by calculation of the invariant mass for all

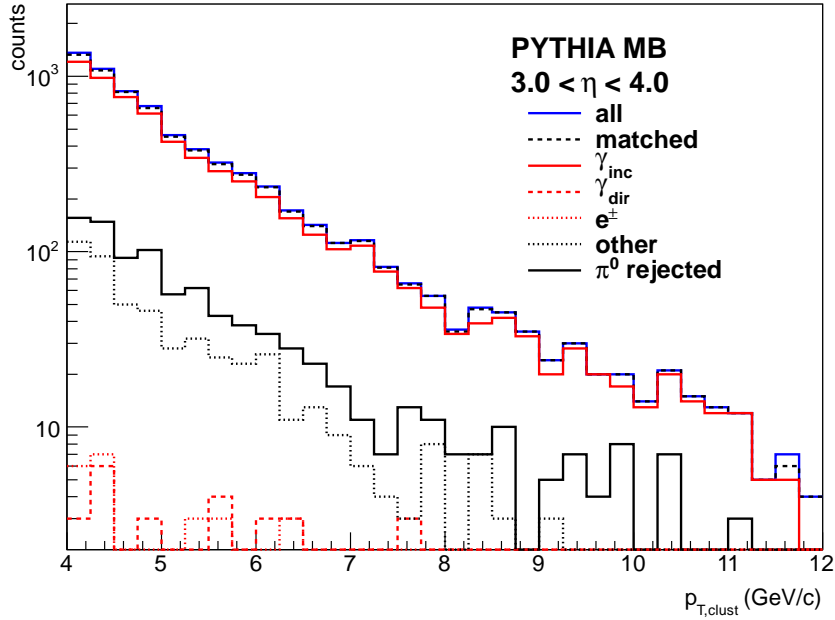


Fig. 40: Reconstructed cluster p_T spectra from minimum bias PYTHIA events ($p+p$ at 14 TeV). The different lines indicate different sources of clusters.

photon cluster pairs in the event, and rejecting photon pairs that fall within the π^0 mass peak region. Figure 41 shows an example of the cluster-pair invariant mass distribution from the PYTHIA events for several p_T bins in the kinematic region of interest. If a photon cluster participates in any pair that falls within the invariant mass window for π^0 decay, the photon is considered to be a decay photon and rejected as a prompt photon. It is clear from Fig. 41 that there is a sizable combinatorial background in the invariant mass distribution which will lead to ‘false’ rejections, decreasing the prompt photon identification efficiency. The resulting cluster spectrum after decay photon rejection is shown as the solid black line in Fig. 40.

An isolation cut is used to further improve the rejection of decay photons which originate from neutral pions and η mesons, as well as charged hadrons, that are typically jet fragmentation products. Further details and examples of the isolation energy distributions can be found in Section 4.2 (Fig. 50) where a comparison is made to $p+\text{Pb}$ events as well. For the present studies, we have applied an isolation cone with radius $R = 0.4$ with rejection of the photon as an isolated or prompt photon when the measured electromagnetic energy in the cone exceeds a threshold of $p_{T,\text{iso}} > 1 \text{ GeV}/c$.

Figure 42 shows the efficiency to correctly identify reconstructed clusters from direct photons (right panel) as well as the efficiency to incorrectly identify clusters from other sources (such as decay) as being direct photons (left panel). Results are shown using π^0 rejection based on the photon-pair invariant mass and shower shape (open triangles), an isolation cut (open squares),

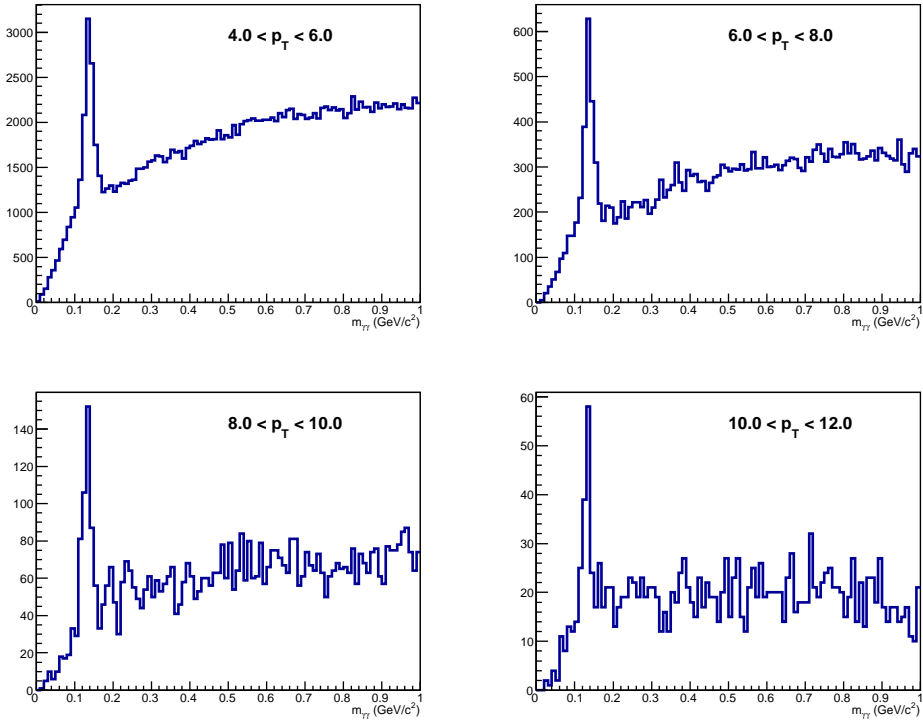


Fig. 41: Reconstructed invariant mass distributions from minimum bias PYTHIA events (p+p at 14 TeV), for pairs with $3.0 < \eta < 4.0$.

and the combination of both (solid squares). In the right panel, it can be seen that the decay rejection falsely rejects $\sim 20\%$ of the direct photon clusters. The effect of the isolation cut on the direct photon sample is smaller (about 5% rejection).

The left panel of Fig. 42 illustrates the efficiency of the decay photon rejection using the invariant mass and shower cuts (open triangles) and the isolation cut (open squares). The invariant mass and shower shape cuts are most effective at lower p_T , where they reject about 90% of the non-prompt photon clusters (efficiency $\sim 10\%$). The isolation cut rejects between 80 and 85% of the decay photons. The combined effect of both cuts (solid squares) is a 96 – 97% rejection of decay photons (efficiency 0.03 – 0.04), independent of p_T in the range studied, while the efficiency for direct photons remains large ~ 0.8 .

Figure 43 shows the ratio of direct photon clusters to all clusters in $3 < \eta < 4$ as a function of p_T for p+p collisions at $\sqrt{s} = 14$ TeV from PYTHIA simulation. The direct photon fraction is observed to be of the order of $\sim 1\%$, decreasing sharply in the region below $p_T \sim 5$ GeV/c. The ratio improves by about a factor ~ 20 when applying both the isolation cut and the direct rejection of decay photons, as expected from Fig. 42. When applied independently the isolation cut and the direct rejection provide similar improvements on the direct photon ratio, with more

than a factor of 2 improvement when combined.

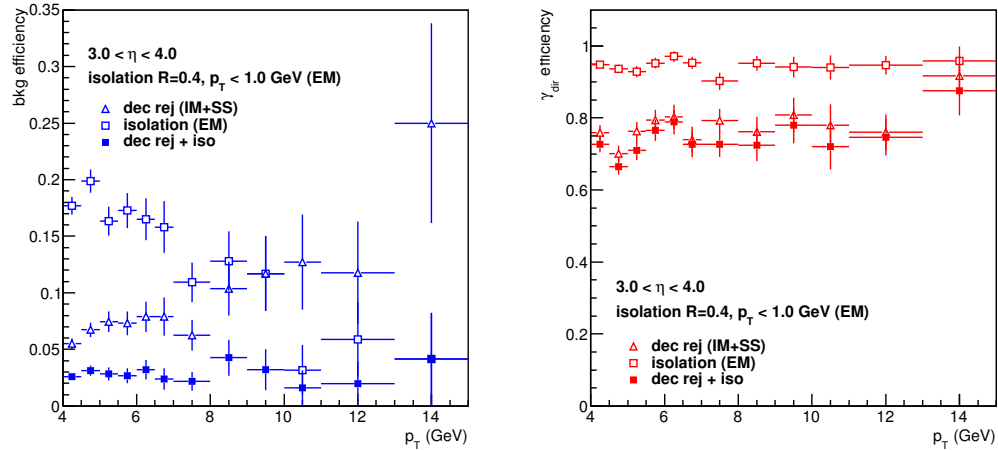


Fig. 42: Efficiency for direct photon clusters in the region $3 < \eta < 4$ to be identified correctly (right) and non-direct photons to be mis-identified as direct photons (left) using π^0 rejection based on the cluster-pair invariant mass and shower shape cuts (open triangles), an isolation cut (open squares), and the combination of both (solid squares) for the FoCal at 4 m.

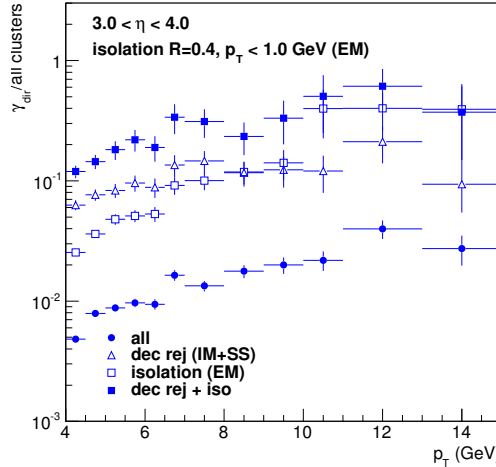


Fig. 43: Ratio of direct photon clusters to all clusters in the FoCal for $p+p$ collisions at $\sqrt{s} = 14$ TeV from PYTHIA, without cuts (solid circles), with π^0 rejection based on invariant mass (open triangles), or an isolation cut (open squares), or the combination of both (solid squares) for the FoCal at 4 m.

Given predictions for the prompt photon cross section (signal), and for the non-prompt photons from decays and jet fragmentation (background), one can calculate the signal/background ratio

and use the expected integrated luminosities (from Table 2) to calculate the expected yield of the isolated photon signal and the statistical error on the signal after background subtraction. The systematic error on the isolated photon signal will have a contribution from the uncertainty on the background that must be subtracted, which will be the dominant systematic error when the background is very large. Application of the background rejection methods using the π^0 rejection and/or isolation cut can suppress the background with some loss of efficiency (as shown in Fig. 42) to improve the signal/background ratio and decrease both the statistical and systematic errors of the isolated photon measurement.

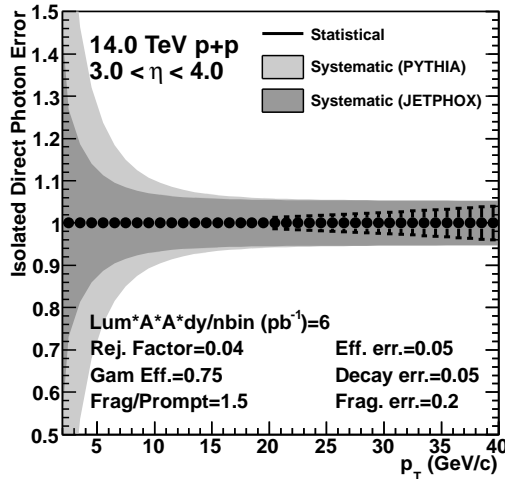


Fig. 44: Estimated relative uncertainties on the direct photon measurement in p+p collisions at $\sqrt{s} = 14$ TeV, based on direct photon spectra from JETPHOX (dark band) and PYTHIA (light band), background spectra from PYTHIA events and the efficiencies shown in Figure 42. Statistical uncertainties are shown as error bars and the systematic uncertainty is shown as a band.

The estimated statistical and systematic uncertainties on the isolated photon p_T spectrum over $3.0 < \eta < 4.0$ measured with the FoCal at 4 m for p+p collisions at $\sqrt{s} = 14$ TeV are shown in Fig. 44. At low p_T , the dominant systematic uncertainty is due to the subtraction of the decay photon background. The uncertainty was estimated using a parametrized fit to both the NLO predictions of JETPHOX (dark grey band) and the LO+shower predictions from PYTHIA (light gray band). The decay photon spectrum was obtained as a fit to the PYTHIA predictions. The non-prompt photons were assumed to be suppressed by a factor of 25 (0.04 efficiency of Fig. 42) with a photon identification efficiency of 75%, with a 5% systematic uncertainty. It was assumed that the decay photon spectrum (mostly π^0 's) would be measured with at 5% systematic error. In addition, fragmentation photons were assumed to be an additional background contribution to be rejected with a cross section that was 150% that of the prompt photon cross section with a 20% systematic error on correction for the remaining background. It was assumed that the various systematic uncertainties added in quadrature.

Under these assumptions, and based on the simulated FoCal performance results above, it's expected that the isolated photon measurement in p+p collisions at $\sqrt{s} = 14$ TeV will be feasible with FoCal with the expected ALICE integrated luminosities with small uncertainty over the region from a few p_T , limited by the systematic error on the decay background, to roughly 50 GeV/c, limited by the statistical uncertainties, as demonstrated in Fig. 44. The exact limit for the direct photon measurement at low p_T depends critically on the direct photon (and decay photon) production cross section, as can be seen from the difference between the uncertainty band based on the PYTHIA and JETPHOX direct photon spectra, which differ by a factor ~ 2.5 (see Fig. 39).

4.1.3 *FoCal at 8m*

With the FoCal located at the 8 m location, the rapidity coverage shifts forward by about one unit of rapidity. For the common region of rapidity coverage ($3 < \eta < 4$) the occupancies will be lower for the 8 m location, and the spatial separation of the decay photons from π^0 's at a particular p_T will be greater at 8 m. This suggests that the rejection of decay photons will be improved for the forward location. This expectation is confirmed by the simulation results for the 8 m location shown in Fig. 45, to be compared with those for the 4 m location shown in Fig. 42. When compared to those results, the rejection of decay photons with the invariant mass cut is seen to be greater at 8 m (left panels). On the other hand, the direct photon identification is slightly worse (right panels), possibly due to additional rejection from the inclusion of clusters in the region of additional rapidity coverage ($4 < \eta < 5$) and the increased combinatorial background.

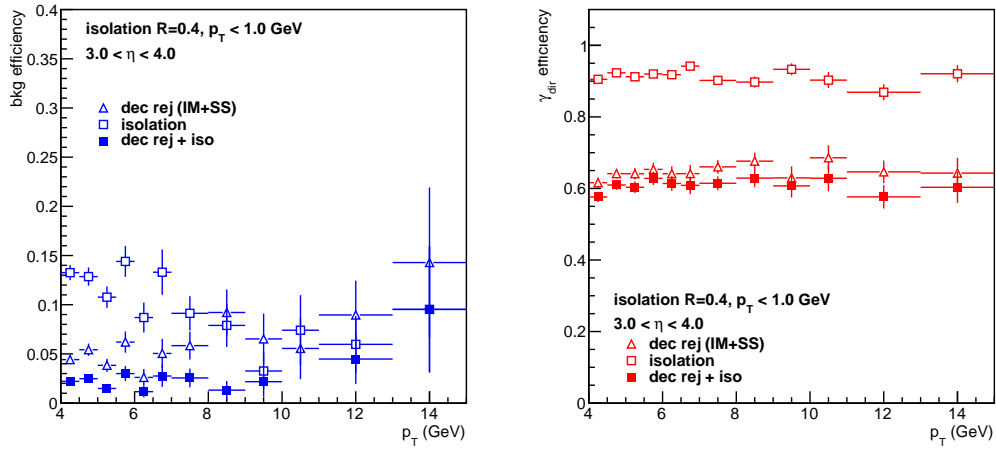


Fig. 45: Same as Fig. 42, but for the FoCal at the 8 m position.

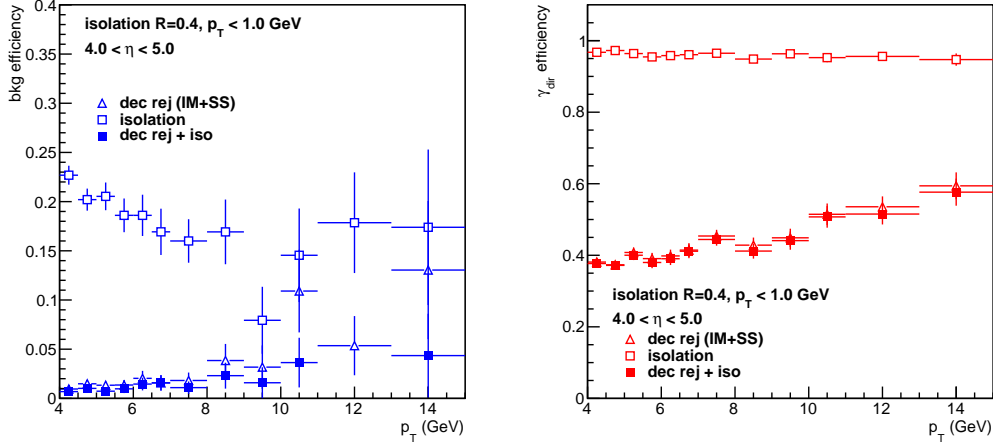


Fig. 46: Same as Fig. 42, but for the FoCal at the 8 m position and $4 < \eta < 5$.

Figure 46 shows the photon efficiency/rejection for photons at the more forward rapidity $4 < \eta < 5$ with the FoCal at the 8 m position. When compared to the lower rapidity selection ($3 < \eta < 4$, Fig. 45), a larger rejection is seen for both decay photons and direct photons. This is due to larger combinatorial background in the invariant mass spectra. However, the combinatorial background will be measured when doing the statistical analysis for the π^0 measurement in real data, from which the false rejection efficiencies can be determined, and therefore the lower efficiency is not necessarily detrimental to the overall performance for the measurement. Furthermore, further improvement may be obtained by additional optimization of the clustering and π^0 rejection algorithms, as well as using the shower shape cut, as was done for the 4 m analysis.

Figure 47 shows the fraction of direct photon clusters as a function of p_T from PYTHIA for p+p collisions at $\sqrt{s} = 14$ TeV with FoCal at the 8m position. For the rapidity range $3 < \eta < 4$ (left panel), the signal fraction is similar for the FoCal at the 4 m position (see Fig. 43). For the larger rapidity region of $4 < \eta < 5$ (right panel Fig. 47), the signal to background is observed to be greater by about a factor ~ 2 .

The expected uncertainties on the isolated photon measurement for the FoCal at the 8 m location are shown in Fig. 48. For the rapidity interval $3 < \eta < 4$ (left panel) the systematic uncertainties are similar or slightly improved as compared to the results expected at the 4 m position (see Fig. 44) due to the small improvement in the signal/background in going to 8 m (see Fig. 47). More importantly, the simulations indicate that the isolated photon measurement is feasible in the very interesting region of $4 < \eta < 5$ (right panel) with the FoCal at the 8 m location.

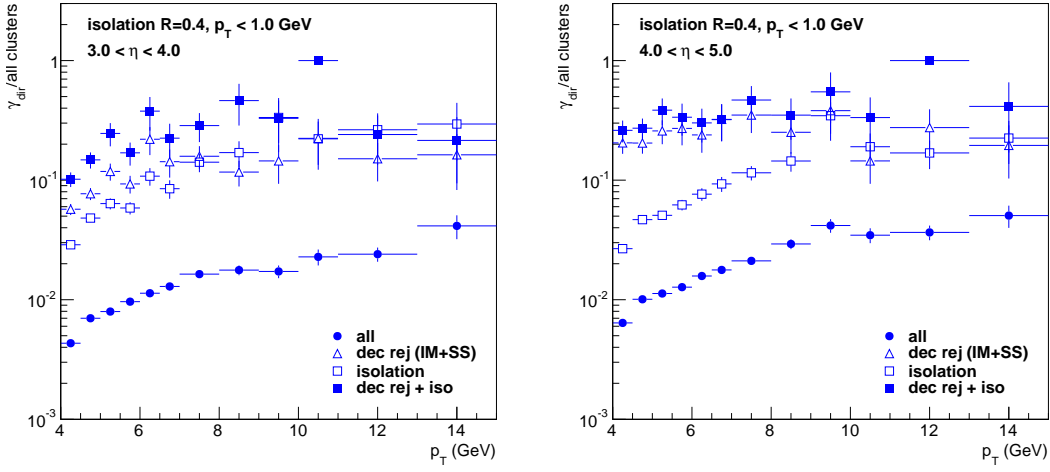


Fig. 47: Same as Fig. 43 for the FoCal at the 8 m position for $3 < \eta < 4$ (left) and $4 < \eta < 5$ (right).

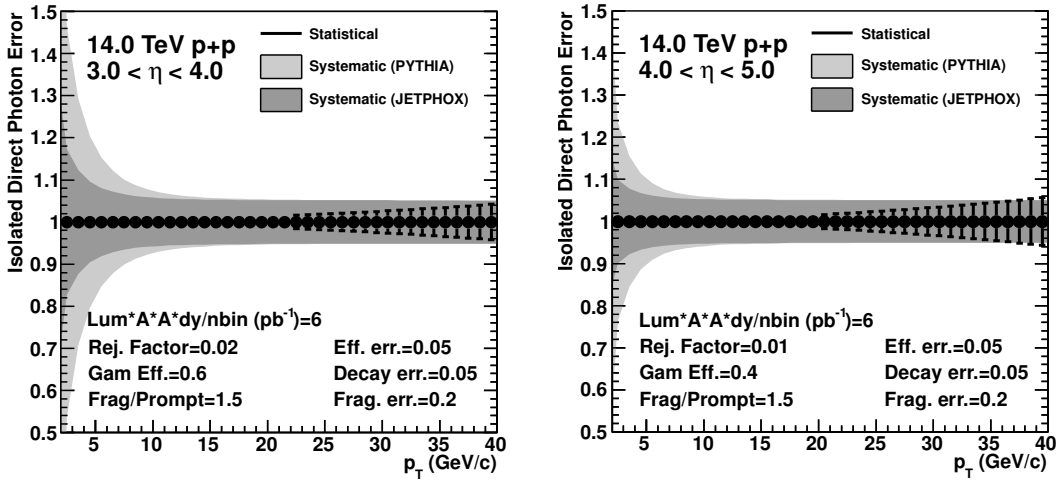


Fig. 48: Estimated relative uncertainties on the direct photon measurement in pp collisions at $\sqrt{s} = 14$ TeV, for FoCaL at 8m and two rapidity ranges $3 < \eta < 4$ (left) and $4 < \eta < 5$ (right). Statistical uncertainties are shown as error bars and the systematic uncertainty is shown as a band.

4.2 Efficiency in p+Pb

Detailed studies of the FoCal performance in p+Pb collisions at $\sqrt{s_{nn}} = 8.8$ TeV are still in progress. However, since the particle multiplicity in the forward (proton-going) rapidity region in p+Pb collisions is not expected to be much higher than that in p+p collisions, the performance of the FoCal in p+Pb collisions is expected to be similar to that in p+p collisions. This

expectation is confirmed by comparisons of the discrimination capabilities in these two reaction systems.

Figure 49 compares the fraction of all reconstructed clusters that pass the π^0 rejection cut for p+p PYTHIA events at $\sqrt{s} = 14$ TeV to p+Pb HIJING events at $\sqrt{s_{nn}} = 8.8$ TeV. The fraction of rejected clusters is similar for the two cases, indicating that there is not a significant difference in the probability to reconstruct photons and π^0 's.

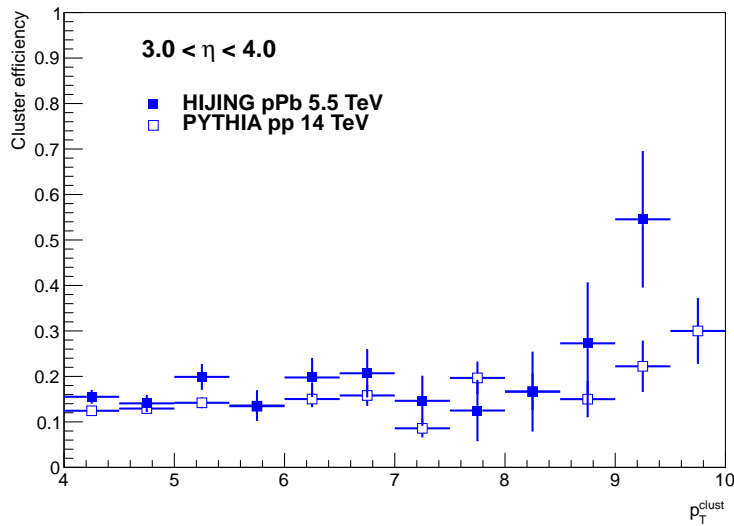


Fig. 49: The fraction of all reconstructed clusters that pass the π^0 rejection cut based on the invariant mass of all cluster pairs in the event for PYTHIA p+p (open symbols) and HIJING p+Pb events (filled symbols).

Similarly, one can also compare the effect of isolation cuts on the photon samples for the two systems. Figure 50 shows the distribution of measured transverse momentum p_T^{iso} in a cone with $R = 0.4$ around clusters with $p_T > 4$ GeV/c (left panel) and $p_T > 8$ GeV/c. It can be clearly seen that direct photons (red line) typically only have a small energy deposit in the isolation cone, while other clusters (decay photons and hadron showers) have a larger energy in the cone. The typical energy in the cone for those cases increases with p_T . The isolation energy distribution in p+Pb events ($\sqrt{s_{nn}} = 8.8$ TeV) is similar to p+p events ($\sqrt{s} = 14$ TeV), indicating that the isolation cuts should provide similar rejection of non-prompt photon cluster in the two cases.

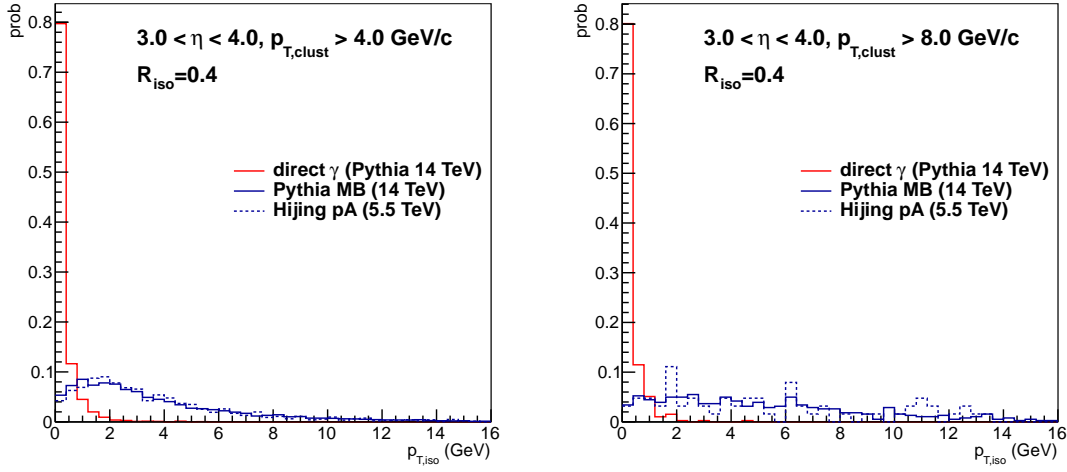


Fig. 50: Measured transverse momentum in an isolation cone with $R = 0.4$ for direct photon events, hadronic PYTHIA events, and HIJING p+Pb events, for two different cluster transverse momenta cuts: 4 GeV/c (left) and 8 GeV/c (right).

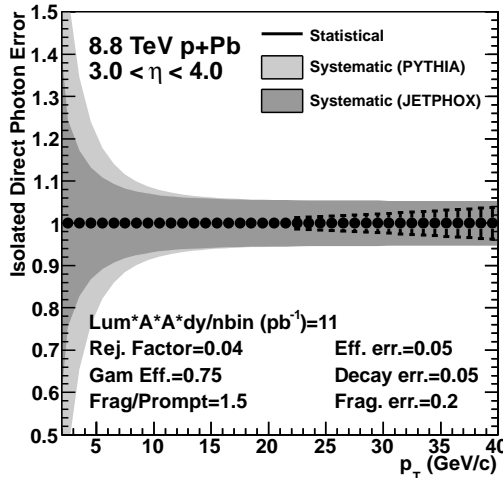


Fig. 51: Estimated relative uncertainties on the direct photon measurement in p+Pb collisions at $\sqrt{s} = 8.8 \text{ TeV}$, based on direct photon spectra from JETPHOX (dark gray band) and PYTHIA (light gray band), background spectra from PYTHIA events, and the efficiencies shown in Figure 42. Statistical uncertainties are shown as error bars and the systematic uncertainty is shown as a band.

Figure 51 shows the relative uncertainties on the direct photon measurement in p+Pb collisions at $\sqrt{s} = 8.8 \text{ TeV}$, based on the spectra from PYTHIA and JETPHOX. The same decay photon

rejection and direct photon efficiency performance as used as for p+p collisions at 14 TeV was used for the p+Pb measurement, as argued above. This assumption will be confirmed with more complete p+Pb simulations.

4.3 Isolation cuts with FoCal-H

Installation of the FoCal at the 8 m location would additionally allow for the installation of a hadronic calorimeter (FoCal-H) immediately behind the FoCal-E. Besides the added capability for a total energy jet measurement that would enable gamma-jet coincidence measurements, the FoCal-H would provide added rejection of non-prompt photons through a total energy isolation cut.

Figure 52 shows the efficiency for reconstructed clusters with $3 < \eta < 4$ from direct photons (right panel) and other sources (left panel) with π^0 rejection based on invariant mass, an isolation cut and the combination of both (solid squares) and the FoCal at the 8m position. The effect of the FoCal-H can be seen as the difference between the solid triangles and solid squares.

Figure 53 is the same as Figure 52, but for the more forward rapidity interval $4 < \eta < 5$.

Figure 54 shows the signal/background ratio for the combination of FoCal-E and FoCal-H at the 8m position, using PYTHIA p+p events with $\sqrt{s} = 14$ TeV. This figure can be directly compared to Fig. 47 without FoCal-H. The improvement in the signal/background ratio with the addition of FoCal-H is about a factor of 2 at $p_T < 7$ GeV/c, where the decay background is the largest.

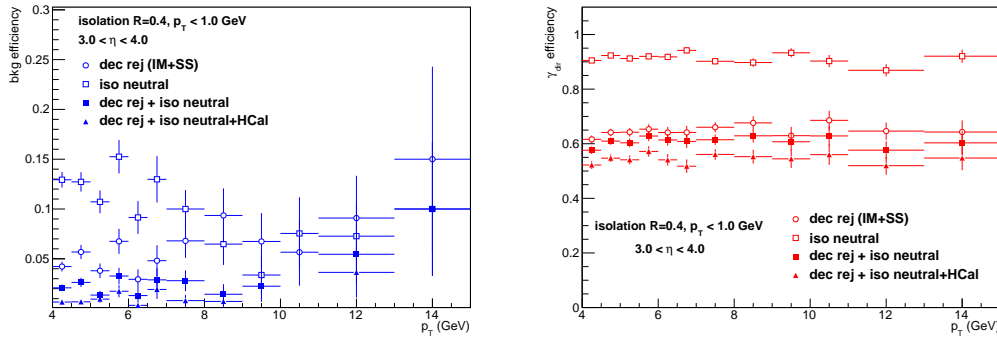


Fig. 52: Efficiency for direct photon clusters in the region $3 < \eta < 4$ to be identified correctly (right) and non-direct photons to be mis-identified as direct photons (left) using π^0 rejection based on the cluster-pair invariant mass and a shower shape cut (open circles), an isolation cut (open squares), or the combination of both (solid squares), or in combination including the FoCal-H in the isolation cut (solid triangles) for the FoCal at 8 m.

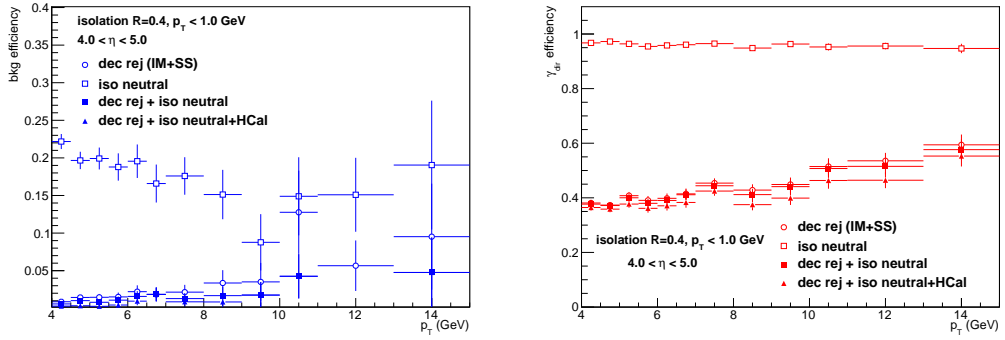


Fig. 53: Same as Fig. 52 for reconstructed clusters with $4 < \eta < 5$.

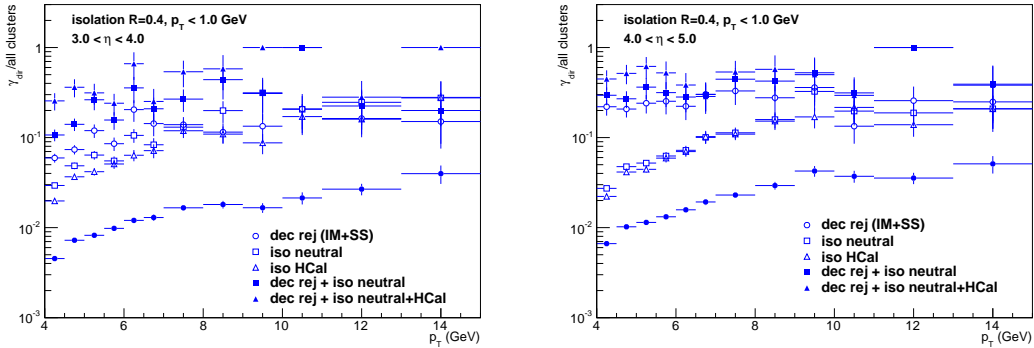


Fig. 54: Ratio of direct photon clusters to all clusters in the FoCal for p+p collisions at $\sqrt{s} = 14$ TeV from PYTHIA, without cuts (solid circles), with π^0 rejection based on invariant mass and shower shape (open circles), or a FoCal-E isolation cut (open squares), or a FoCal-H isolation cut (open triangles), or the combination of π^0 rejection and FoCal-E isolation (solid squares), or for the combination of π^0 rejection and isolation cuts with the FoCal-E and FoCal-H, for the FoCal at 8 m. The left panel shows the results for $3 < \eta < 4$ and the right panel for $4 < \eta < 5$.

4.4 Performance with reduced granularity

To quantify the performance gained from the fine granularity (1 mm^2) of the FoCal design, we have performed simulation studies using only the Low Granularity Layers, with 1 cm^2 granularity. This granularity at 4 m from the interaction point is expected to be approximately equivalent to that of the LHCb calorimeter, which is positioned at $z = 1249 \text{ cm}$ (i.e. 3.5 times farther away) and has a granularity of 4.04 cm . The Moliere radius for the LHCb lead-scintillator calorimeter is also 3-4 times larger than that for FoCal.

Figure 55 shows the efficiency for decay photon identification/rejection using transverse and longitudinal shower shape cuts (as discussed in Sec. 3.3.1) and by direct rejection from invariant mass reconstruction. Results using the full FoCal (left panel) are compared with results using only the low granularity layers (right panel). The figure shows that the invariant mass analysis with the coarse granularity information alone would be very inefficient to reject decay photons above about $p_T > 8 \text{ GeV}/c$, improving to about 0.4 inefficiency to reject π^0 decay clusters at $p_T = 4 \text{ GeV}/c$. The shower shape cut can be used to identify π^0 decay clusters with an efficiency of about 0.5, which is the limit of the decay photon rejection at high ($p_T \geq 10 \text{ GeV}$).

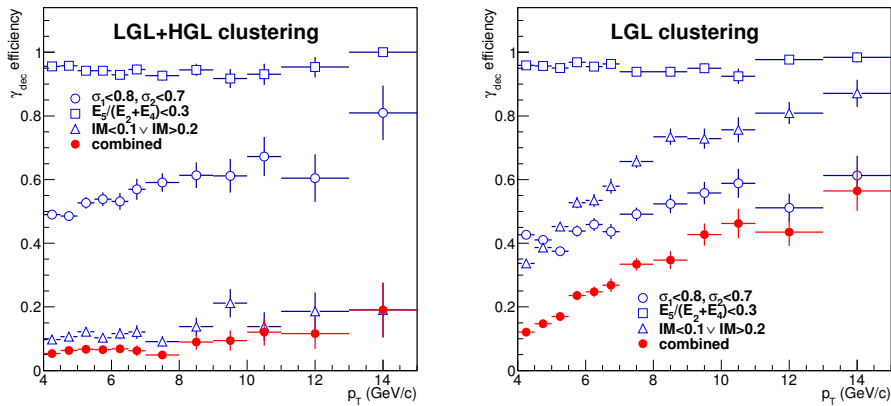


Fig. 55: Comparison of the efficiency with which decay photons would be mis-identified as direct photons using selections on the transverse shower shape (open circles), or longitudinal shower shape (open squares), or on the reconstructed invariant mass (open triangles) for the full FoCal (left) and in the case that only the low granularity layers are used (right).

Figure 56 shows the efficiency for non-prompt photon clusters to be mis-identified as prompt photons (left panel) and the efficiency for photon identification (right panel) for p+p PYTHIA events at $\sqrt{s} = 14$ using only the information from the low-granularity layers of the FoCal. For the isolation cut, we also included a simple parametrised HCAL response, since LHCb also has a forward HCAL. When compared to the results obtained using also the HGL of the FoCal (Fig. 42), it can be clearly seen that the decay photon rejection is much less efficient with the lower granularity. In particular, for $p_T > 8 \text{ GeV}/c$, where the efficiency for decay photon rejection is around 50 %. The isolation cut helps the rejection of the non-prompt background when using

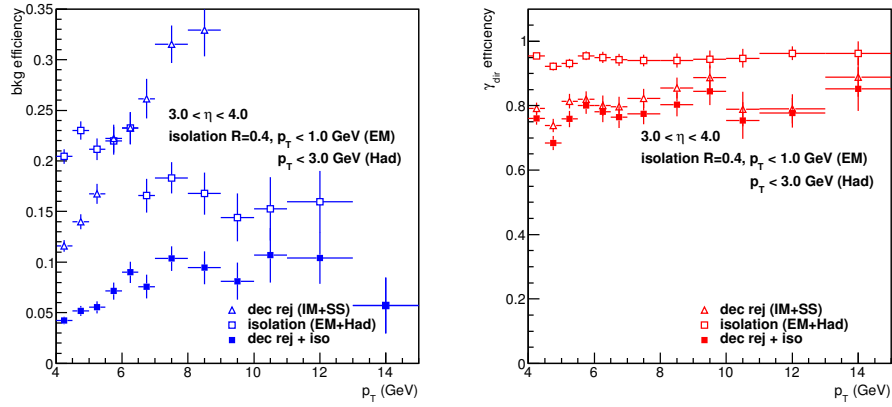


Fig. 56: Efficiency for direct photon clusters in the region $3 < \eta < 4$ to be identified correctly (right) and non-direct photons to be mis-identified as direct photons (left) using only the low granularity layers of FoCal and a parametrised response for a hadronic calorimeter in the isolation cuts. Results are shown using shower shape cuts and π^0 rejection based on the cluster-pair invariant mass (open triangles), or an isolation cut (including parametrised HCAL response; open squares), or the combination of both (solid squares).

just the LGL information and further reduces the non-direct- γ contribution, but the remaining fraction is about 3-4 times larger than obtained with the HGL at high p_T .

Figure 57 shows the prompt photon fraction after cuts, for PYTHIA p+p events at $\sqrt{s} = 14$ TeV, using only the low-granularity layers. When comparing this figure to the case with the full detector using the HGLs (Fig. 43), there are two clear differences. Firstly, the signal/background before cuts is lower by about a factor of ~ 2 with the LGL information only due to the merging of decay photons into a single cluster with resulting higher p_T of the cluster. In addition, the rejection of the non-direct- γ contribution is less efficient (see Fig. 56). As a result, the signal fraction is only ~ 0.07 for $p_T < 10$ GeV/c and rising slowly for higher p_T , while the signal fraction for the full detector is 0.10 at $p_T = 4$ GeV/c and around 0.4 at $p_T = 8$ GeV/c.

Using the efficiency estimates of Fig. 56 the statistical and systematic uncertainties of the prompt photon measurement can be estimated for a low granularity calorimeter, such as the FoCal without high granularity layers, which is roughly equivalent to the performance expected for the LHCb calorimeter, the best of the existing electromagnetic calorimeters in the forward rapidity region at the LHC. The expected uncertainties for such a low granularity detector are shown in Fig. 58, where it is observed, that the measurement would only become feasible above $p_T = 15$ –20 GeV/c.

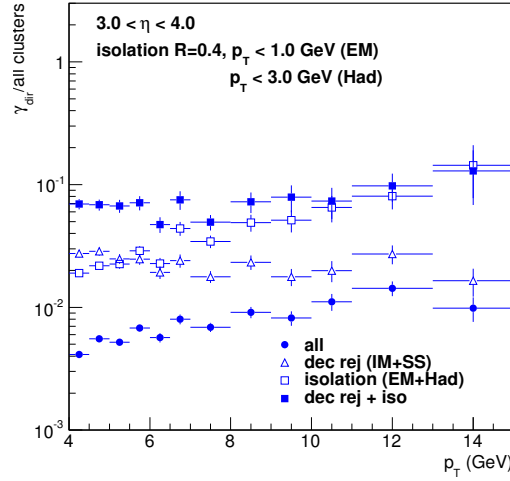


Fig. 57: Ratio of direct photon clusters to all clusters in the region $3 < \eta < 4$ from PYTHIA events for p+p collisions at $\sqrt{s} = 14$ TeV, without cuts (solid circles), or with π^0 rejection based on invariant mass and shower shape cuts (open triangles), or an isolation cut (including parametrised HCAL response, open squares), or the combination of both (solid squares).

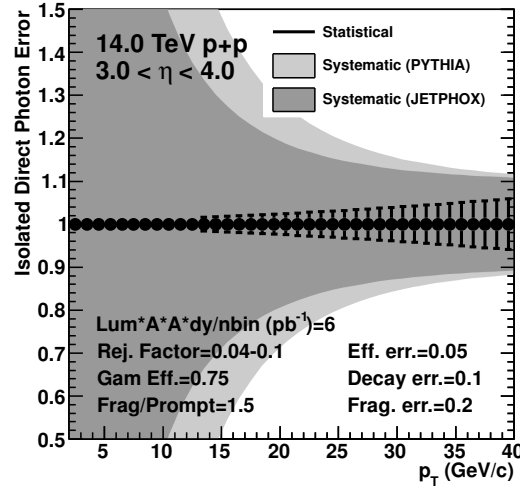


Fig. 58: Estimated relative uncertainties on the direct photon measurement in pp collisions at $\sqrt{s} = 14$ TeV, based on direct photon spectra from JETPHOX or PYTHIA, background spectra from PYTHIA events, and the efficiencies shown in Fig. 56 using only the low-granularity layers of the FOCAL and a parametrised response for an HCAL. Statistical uncertainties are shown as error bars and the systematic uncertainty is shown as a band.

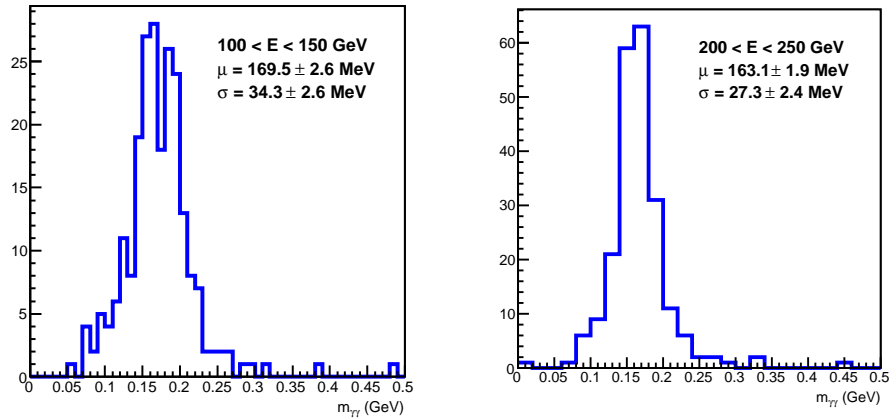


Fig. 59: Invariant mass distribution of reconstructed clusters from π^0 embedded in central HIJING Pb+Pb events. The listed values for the mean μ and width σ are determined from a gaussian fit to the measured peak.

4.5 Efficiency in Pb+Pb

Simulation studies to investigate of the FoCal performance in Pb+Pb collisions have just begun. The conditions for direct photon measurements in central Pb+Pb collisions will be much more challenging, and will require further optimization of the algorithms which have been developed for the p+p and p+Pb measurements. In addition, the production of Pb+Pb simulation events is computationally intense.

The performance of the FoCal in Pb+Pb collisions has begun to be investigated using a sample of events with π^0 's embedded in HIJING Pb+Pb events, and using the algorithms which have been developed for the p+p and p+Pb studies. First results shown in Fig. 59 demonstrate that the π^0 's are clearly reconstructable, although degraded in resolution due to shower overlaps from the high particle density.

Fig. 60 shows the detection efficiency for π^0 in those events, selecting photon clusters with a reconstructed invariant mass of $0.1 < m_{\gamma\gamma} < 0.25$ GeV/c^2 . With this mass selection, the efficiency is larger than 0.8 over a broad p_T range.

Figure 61 shows the estimated relative uncertainties on a π^0 measurement in central 0-10% Pb+Pb collisions using the full 10 nb^{-1} luminosity. The statistical uncertainties are based on the expected production rates and an efficiency of 80% over the full p_T range. The dominant systematic uncertainty at low p_T is due to the combinatorial background. This background was estimated using HIJING Pb+Pb events and it is found that at 4 GeV, the signal to background ratio may be as low as 0.5%. We have assumed a conservative systematic uncertainty on the background subtraction of 0.25%. At high p_T , the measurement will be limited by the decreasing efficiency for π^0 detection due to shower merging and the ability to use shower shape measurements to identify π^0 . This has not yet been investigated in detail.

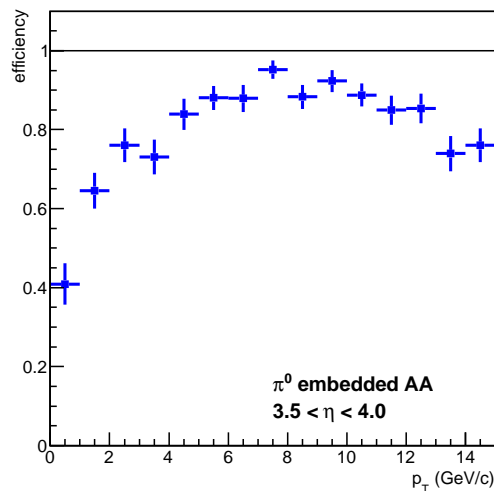


Fig. 60: Efficiency for π^0 detection in central Pb+Pb collisions.

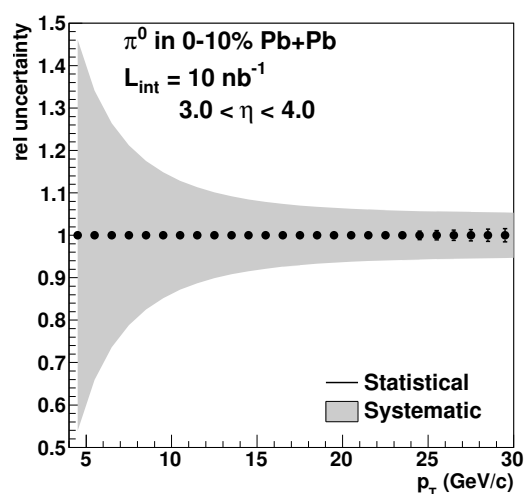


Fig. 61: Expected relative uncertainty on a π^0 measurement in 0-10% Pb+Pb collisions.

4.6 γ_{dir} and jet measurements in Pb+Pb collisions

Given the large kinematic reach for inclusive and coincidence measurements of γ_{dir} and jets in Pb+Pb collisions (see Fig. 23), we expect that these measurements are feasible even with the large uncorrelated background in heavy-ion collisions. The performance for such measurements has not been evaluated in detail, but we can give some estimates. Based on CMS measurements of the transverse energy [63] and ALICE measurements of the charged particle multiplicity at forward rapidities [64] one can estimate that the overall background level at $\eta \approx 4$ is reduced by a factor of two with respect to mid-rapidity. More importantly, the background fluctuations are also expected to be reduced by a factor of about 2, due to a combination of the reduced overall background and a reduction in the mean p_T of the background.

The current ALICE jet measurements at central rapidity have a lower p_T cut-off around 30–40 GeV, because of the background fluctuations. It is therefore reasonable to conjecture that at forward rapidities jet reconstruction in central Pb+Pb will be feasible down to $p_T = 20 \text{ GeV}/c$ (even lower at larger η).

A similar argument applies to γ_{dir} measurements at larger p_T where isolation cuts are needed, but they are also affected by background fluctuations (current ATLAS measurements for γ_{dir} at mid-rapidity go as low as 40 GeV in central collisions). With this estimate (more quantitative simulation studies will be pursued in the near future) and the expected rates in Pb+Pb collisions, the kinematic reach is sufficient to perform inclusive and coincidence measurements for γ_{dir} and jets with the Focal-(E+H).

4.7 Physics Performance Summary

In the preceding Sections, we have shown the expected performance of the FoCal detector for direct photon measurements. At high p_T , where the signal fraction (ratio of direct photons to all non-direct-photon clusters) is close to unity or even above 1, the uncertainties on the measurement are driven by the uncertainty on the photon detection efficiency, which can be expected to be about 5% or better. At lower p_T , the signal fraction decreases and the measurement becomes more challenging. The measurement becomes impossible when the signal fraction becomes 0.05 or lower, which is the expected uncertainty of the decay background estimate.

With FoCal-E we can reject up to 97% of the decay photon background using a combination of π^0 rejection and isolation cuts, thus improving the signal fraction by a factor of ≈ 20 . This enables the measurement of direct photons at lower p_T , from $p_T \approx 5 \text{ GeV}/c$. The exact p_T reach at low p_T depends critically on the direct photon production rates, which have a rather large uncertainty in this range, see Section 4.1.1. We have also explored the performance of FoCal at two different positions: at 4 m and 8 m location.

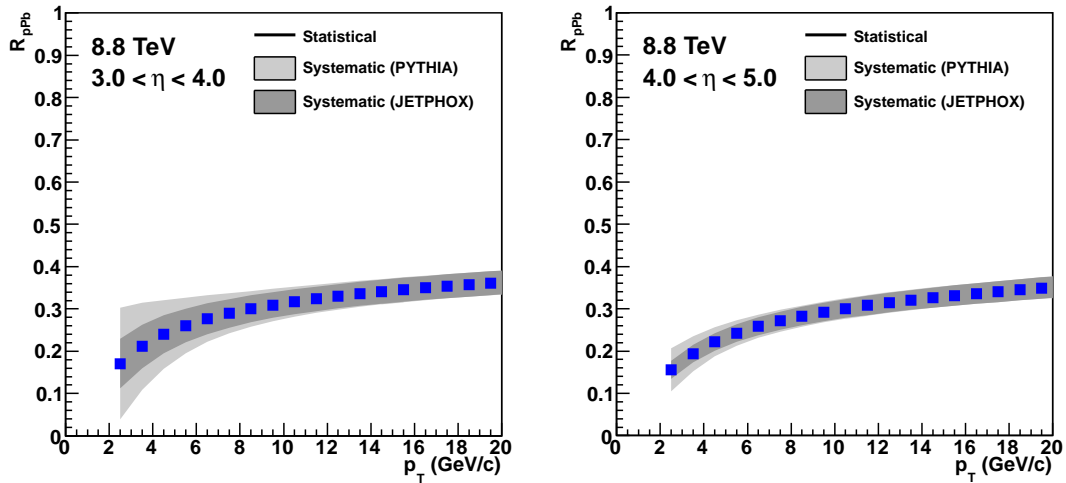


Fig. 62: Simulated measurement of the nuclear modification factor R_{pPb} for inclusive direct photons $3 < \eta < 4$ (left panel) and $4 < \eta < 5$ (right panel) using the prediction from a gluon saturation model as input (see Fig. 9). The grey bands indicate the expected systematic uncertainties, using signal fractions from PYTHIA (light gray) and JETPHOX (dark grey)

The implication of the FoCal performance for a measurement of the nuclear modification factor R_{pPb} of direct photons is illustrated in Figure 62, which shows the expected precision of such a measurement for p+Pb collisions at 8.8 TeV, at $3 < \eta < 4$ (left panel) and $4 < \eta < 5$ (right panel). The higher rapidity interval can only be reached with the FoCal at the 8m position.

For the physics performance, the 8m position is clearly preferred, because it extends the acceptance of the detector to more forward rapidity, which means lower x reach, into the region

$4 < \eta < 5$, which is not covered by any LHC experiment. In addition, for the larger η interval the signal fraction is larger allowing for a better measurement, because the direct photon fraction produced in the collisions is larger and the detector performance does not strongly change with rapidity.

Moreover, placing the FoCal-E at 8m would allow to add a hadronic calorimeter, which further improves the decay photon rejection (by isolation cuts, see Figs 52 and 53) as well as jet measurements.

However, constructing FoCal at 8m requires a significant redesign of the beam pipe infrastructure. From current discussions it is likely that the disturbances of the measurement can be kept at a minimum with redesigned beam pipe and supports, such that this clearly unique option should be feasible.

The FoCal location at $z = 360$ cm provides a more modest alternative. The forward rapidity coverage at this position will be limited to $\eta < 4.5$, but a high-quality direct photon measurement with discovery potential for CGC effects is still possible. The LHCb experiment has a forward calorimeter that covers the same rapidity range, but with much lower granularity than FoCal-E. We have explored the performance of such a detector by using only the LGL segments of FoCal-E (see Section 4.4) and shown that such a calorimeter is not capable of performing a high-precision measurement of direct photons in the forward rapidity interval. This would give this second solution, although not quite as attractive, also a unique status at the LHC.

In Pb+Pb collisions, a measurement of π^0 spectra and R_{AA} is possible for $p_T > 7$ GeV/ c (see Fig. 61) up to at least $p_T = 20$ GeV/ c (see Fig. 60). The p_T reach can be extended by improving the reconstruction algorithms and using shower shapes to identify π^0 . The abundant statistics can also be used to measure recoil jet suppression using π^0 - π^0 correlations.

There is also a clear potential for the direct photon measurement in Pb+Pb collisions. The decay photon rejection in Pb+Pb collisions is more problematic than in p+p events, so the low p_T reach for the measurement will be limited. At high p_T it is likely to be feasible with a modest decay background rejection.

5 Technical Implementation

5.1 Mechanics

As discussed above, two options are under consideration for the location of the FoCal. In one option, the FoCal would be located at $z = 3.6$ m from the IP (the "4m position"), replacing the PMD detector. Figure 63 shows the present situation at the Miniframe with the PMD replaced by the FoCal in the tower geometry. While the beamline is supported by the Spaceframe, FoCal needs to be supported by the Miniframe. This makes it dangerous to come too close to the beamline and 8 cm ($\eta = 4.5$) from the beam is considered the minimum. A separate inner section with circular geometry and supported from the Spaceframe would allow to reach ≤ 5 cm ($\eta \geq 5$), but this option is not worked out yet, neither mechanically, nor in terms of detector performance.

FoCal-H with its weight of ≈ 150 kN cannot be mounted on the Miniframe. Given the mechanical constraints an installation of FoCal-H in this location seems very difficult.

The other option is to place the detector at $z = 8$ m, where both FoCal-E and FoCal-H can be installed. This would require the compensator magnet to be moved to $z \geq 10$ m, while its support could be used for FoCal-H. The construction of the FoCal-E would likely be the same in either location and is discussed in the following section.

5.1.1 FoCal-E Mechanics

With an inner radius of 8 cm and an outer radius 0.6 m, FoCal covers 1.13 m^2 . The detector will consist of $\approx 20 - 25$ layers of $\approx 1X_0$ equivalent thickness each. This corresponds to 3.5 mm thick tungsten per layer, plus the active material. To avoid costly machining of tungsten one may choose a layer thickness corresponding to the nearest industry standard. Two options for the mechanical structure of FoCal-E are under consideration (see Fig. 64):

1. The full detector matrix consists of identical independent blocks of full longitudinal depth.
2. The detector consists of horizontal slats, each comprising a few layers only.

The block geometry (Fig. 64 left) is very flexible. It can be assembled in a staged approach. All blocks are identical and individual faulty blocks can be replaced by spares (presuming the blocks are independently supported). However, all services (cables and cooling) have to be routed to the back of the detector for every block. This requires significant gaps ≈ 1 cm in the $x - y$ plane⁶ without active detector material, which would degrade the detection efficiency and resolution. In z the space for sensors and services can be small ≈ 1.5 mm, leading to a compact detector with a depth of ≈ 12.5 cm, independent of the type of layers. However, as all services go out along z , the *total* depth required will at least be double this number.

The slat geometry (Fig. 64 right) allows to bring the services within the layers to the side of the detector, which reduces the transverse gaps to a minimum. However, the Δz gaps between the

⁶We use the ALICE coordinate system.

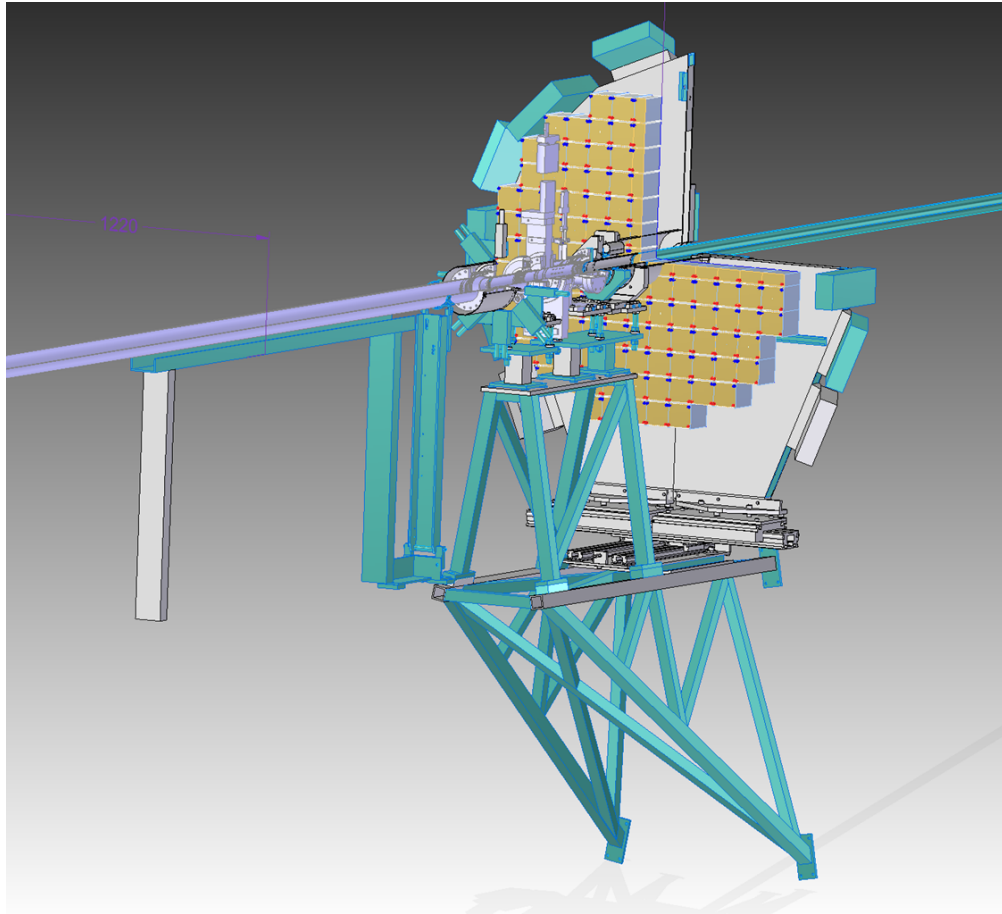


Fig. 63: FoCal replacing the PMD in the present layout of the beamline. View towards the interaction point.

segments need to be as much as ≈ 1 cm for the high granularity layers where cooling and more complex read-out is required. These gaps with large X_0 material will increase the Molière radius. The full thickness of the detector will thus depend on the number of high granularity layers. The size of the slats is determined by the services: all cooling and cabling from the sensors at the inner radius have to pass over those of the outer radii. Apart from the increase in thickness, the limitation comes from the maximum allowable length of the cables (cross talk, signal and power loss) and cooling lines (pressure loss, temperature rise). For the MAPS considered in the HGL this gives a maximum slat length of ≈ 0.3 m. For these conditions the simple layout of figure 64 may not be feasible and a two-tier set-up might be preferred, where the innermost slats are behind (*i.e.* at larger z than) the outermost, such that services of the former do not obscure the latter, see figure 65. The resulting smaller size of the units has the additional advantage of lower mass and easier handling. The four units, left/right, front/rear could be suspended from rails analogous to the PMD.

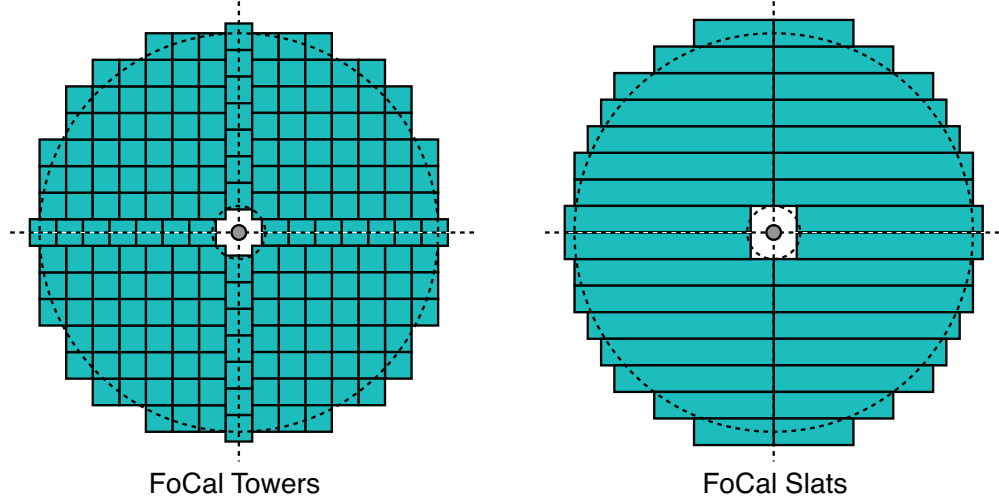


Fig. 64: Schematic sketch showing frontal views of the two options considered: block geometry (left), and slat geometry (right). The dashed circular lines indicate radial positions of 8 cm and 60 cm, respectively, corresponding to $\eta = 4.5$ (5.3) and 2.5 (3.3) for $z = 3.6$ (8) m.

The height/width of a block or slat will have to be carefully chosen, in order to accommodate the active areas of the HGL and the LGL. In the HGL it needs to be a multiple of the size of the MAPS sensor, presently 1×3 cm 2 . Here one also has to take into account the overlap of the active area of the chip. In the LGL it needs to be a multiple of the size of a padsensor. Here two options remain: 93 mm (6" wafer) or 62 mm (4" wafer). With these options still open and the fact that the final sensor chip is not available yet, all layouts are provisional.

For the slat geometry considerable space (≥ 0.5 m) in the x or y direction is required, especially when one considers to remove individual slats in between others. In order to reduce the thickness of the slats, it is advantageous to combine a few layers in units with common cooling and cabling connections, as these tend to be rather bulky. To allow for sufficient cooling of single layer slats, the spacing between them required for (dis)mounting of the connectors would need to be very large, such that multiple MAPS layer may be preferable. A possible design with 3 MAPS layers is shown in figure 66. Its power and cooling are designed for 0.5 kW, the present estimate for MAPS. For the Low Granularity Layers (LGL) the summing board connecting several layers in z excludes the possibility of the removal of individual layers. For horizontal slats these boards run in the $x - z$ -gaps between adjacent slats and cannot be disconnected *in situ*. A solution is being worked out to remove the HGL while the LGL remain in place. It is obvious that the slat option with mixed HGL and LGL, the former read out from the sides and the latter interconnected in z , is mechanically complex. The minimisation of the fraction of dead (non instrumented) zones in the $x - y$ plane, needed for connections and support, will be an important boundary condition of the final design.

The total weight of FoCal-E is determined mainly by the total amount of tungsten used, which amounts to ≈ 19 kN, depending on the exact mechanical layout.

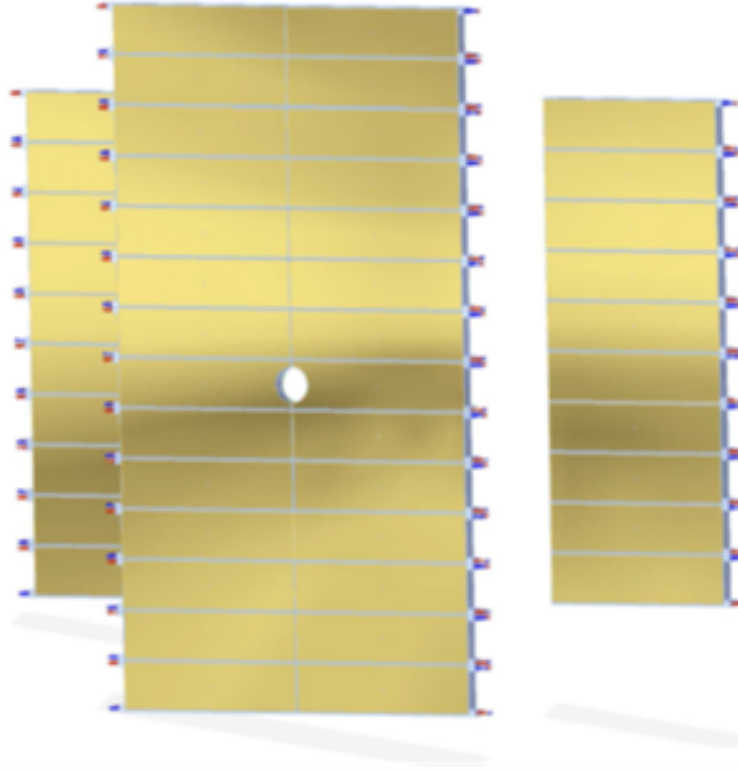


Fig. 65: Two tier layout with 0.3 m slats. View towards the interaction point. For a better view, the z scale is expanded, the real distance between the tiers is ≈ 0.1 m.

The detector units for both options will be built as mechanically self-supporting, so that they can be stacked within a support frame allowing the removal of individual units. There is a price to pay here, however: the configuration with mixed technologies already being quite complex by itself, becomes more complex because of this requirement of *in situ* replacement. One could imagine to take out a full quarter of FoCal outside the cavern and repair/replace units in USX with the help of special jigs. The total construction would be simpler, at the cost of not being able to repair during runtime.

5.1.2 *FoCal-H Mechanics*

Overview The FoCal-H is a sampling hadronic calorimeter designed to mount behind FoCal-E and provide photon isolation by direct detection of high energy hadrons lying close to the trajectory of the candidate direct photon. In addition, the detector will provide a direct measure of jet production in the same phase space that FoCal-E will provide direct photon measurements. For the above applications and limited to the forward rapidity region occupied by the FoCal, we are interested in very high energy hadrons where the constant term in the calorimeter response will dominate. In such a detector, the constant term is driven by the Electro-Magnetic to Hadronic (EM/HAD) fluctuations in the hadronic shower. As an absorber material, Pb has

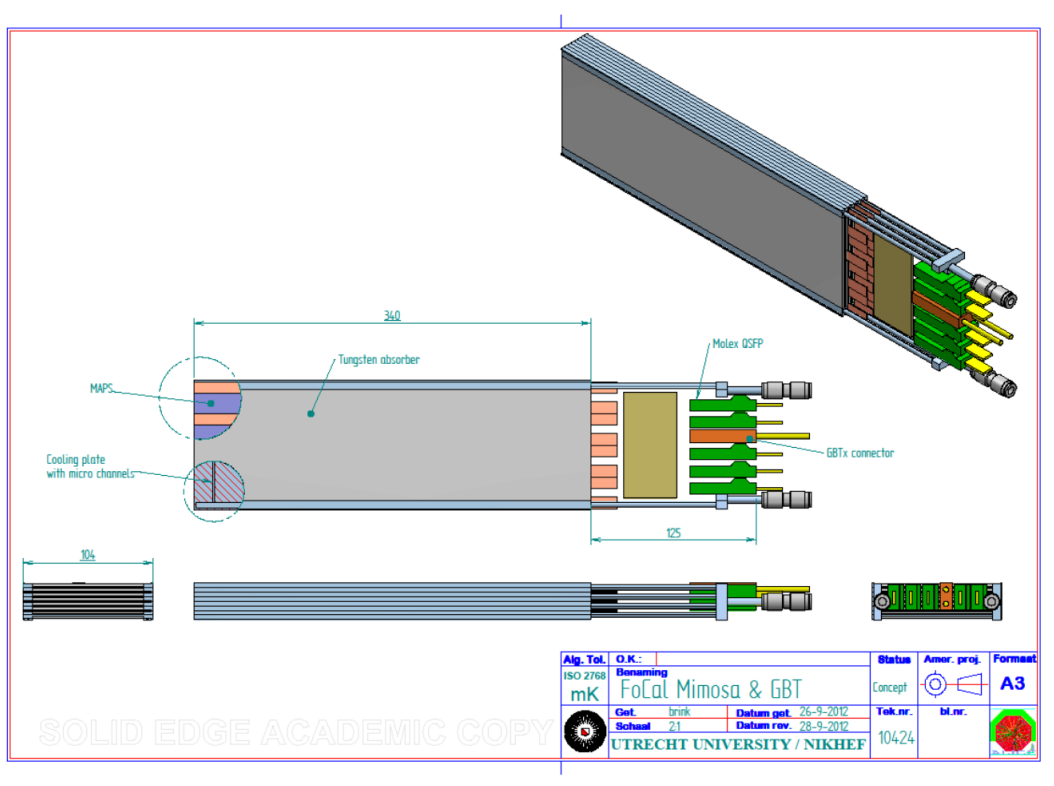


Fig. 66: Three MAPS layers in a slat of 300 mm active length and 100 mm height with combined connectors for cooling and cabling. The total thickness is 28 mm.

been shown in theoretical calculations by Wigmans [65] and confirmed by experimental studies by Bernardi *et al.* [66] and subsequently in a large prototype by the SPACAL collaboration [67] to allow reasonable EM/HAD compensation and good hadron resolution through the selection of the correct Pb to scintillator volume ratio. Thus, at the high energies relevant for FoCal, a properly designed Pb/scintillator sampling calorimeter is expected to yield a good hadron performance.

Members of the FoCal collaboration have significant experience with Pb/scintillating fiber spaghetti calorimeter technology, both hadronic and electromagnetic, that includes the STAR Barrel Electromagnetic Calorimeter, the PHENIX Electromagnetic Calorimeter, the ALICE EMC and most relevant to the present case, the AGS E864 Hadronic Calorimeter.

For application in FoCal, we choose the Pb/scintillating fiber spaghetti calorimeter technology first prototyped by the SPACAL Collaboration [67] and later utilized in a first large-scale application in AGS E864 [68]. This detector has excellent hadronic electromagnetic and hadronic resolution and good compensation. A single module is shown in Fig. 67. The dimensions W, L and S may be easily varied to suit a particular application. In AGS E864 we used W=10 cm, L=177 cm and S=42 cm and, as it turns out, these dimensions match well the needs of the FoCal application. In AGS E864, however, each module was configured as a single 10 cm × 10 cm

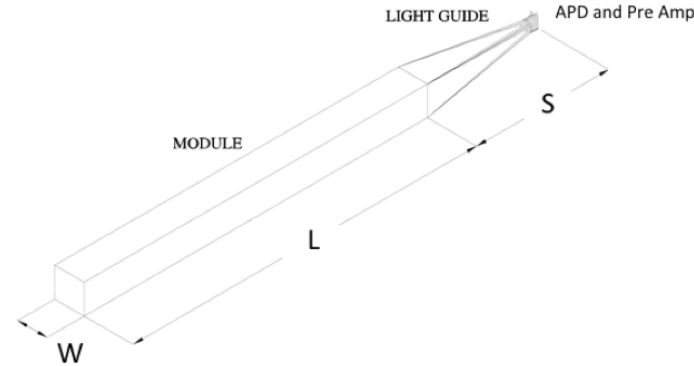


Fig. 67: An example of a hadronic calorimeter module with front face dimensions $W \times W$, active length L and a single light diffuser/mixer of length S .

tower. However, with 4 light collector/diffusers, each module then provides 4 separate, optically isolated towers of $5\text{ cm} \times 5\text{ cm}$. This latter approach is the preferred solution for FoCal. We successfully used this configuration of 4 towers per $10\text{ cm} \times 10\text{ cm}$ module in the FermiLab Tevatron MiniMax experiment [69].

Figure 68 shows the end view of a $10\text{ cm} \times 10\text{ cm}$ module as used in E864. Because every scintillating fiber is optically isolated from its neighbors, the tower geometry within a given module is completely defined within some reasonable geometric restrictions by how many fibers are grouped together to a single light collector/diffuser leading to a single photo-sensor. The scintillating fiber density shown in Figure 68 (and accounting for glue layer that holds the module together) corresponds to a Pb to scintillator ratio of 4.55:1 by volume. This is the value found to be optimum by the SPACAL collaboration and confirmed at low energies in the test beam studies by the E864 collaboration.

Construction and assembly The mechanical structure of the module shown in Fig. 67 is easily achieved. The module is built up from stacked Pb plates. A 1% admixture of antimony is added to harden the lead to a sufficient mechanical rigidity to permit easy handling while having a negligible impact on the calorimeter performance. Bicron BCF-12 scintillating optical fibers are used as the active sampling material. They were selected for their good specific light yield (50% of the yield obtained with anthracene), good transmission ($1/e$ length $\sim 2.2\text{ m}$), and fast response (decay time $\sim 3.2\text{ ns}$). The scintillating fibers are laminated between the lead plates and glued with Bicron BC-600 epoxy [70]. The fibers at the tower front faces are diamond polished and then coated with a sputtered aluminum surface to produce a highly uniform mirror. After assembly of the module, the aluminum coating is then covered with a light absorbing (black) epoxy paint to protect the mirror from damage and avoid light leaks at the corners of the fibers. One or more tapered light collector/diffuser is glued at the back of the module to the

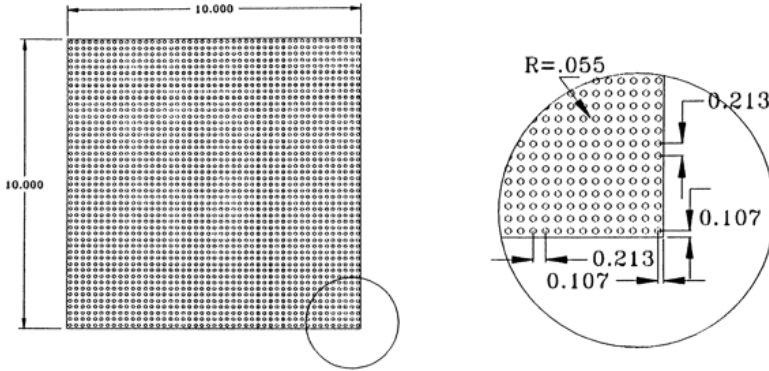


Fig. 68: An end view of the Pb/Scintillating fiber sampling hadronic calorimeter module with front face dimensions 10 cm \times 10 cm. The scintillating fiber density shown here (accounting for glue) corresponds to a Pb to scintillator ratio of 4.55 : 1 by volume. All dimensions are in cm.

diamond polished fiber group belonging to a single tower using an optically coupling adhesive (Bicron BC- 600) as illustrated in Fig. 67. The light guide shape and dimensions are optimized by optical ray tracing calculations to enable uniform photon collection and transmission to the photo-sensor from all fibers within a given tower. Ultra-violet absorbing lucite will be employed for the fabrication of the light guides in order to reduce Cherenkov light created within the light guide reaching the photosensor and deteriorating the energy response. Cherenkov light is generated by fast shower particles (e.g. electrons) produced at the back of the calorimeter. The BCF-12 scintillator optical emission peaks at much longer wavelengths, 420 nm, than the Cherenkov radiation. The scintillation light suffers very little attenuation in the lucite and thus, only a small fraction of the true signal is absorbed while signal contamination is greatly reduced. As noted above, the towers have a lead to fiber ratio of 4.55 : 1 by volume similar to that used in the SPACAL prototype. Based on measurements in the literature, this is expected to provide for good calorimetric compensation and resolution. Given the module parameters to be adopted for FoCal, the average tower density is 9.6 g/cm³. The effective radiation length (X_0) is 7.8 mm. The nuclear interaction length (Λ_{had}) and the Moliere radius (R_M) are 19.7 and 2.2 cm respectively.

Several spaghetti calorimeter mechanical construction techniques have been described [67]. Studies have shown that the energy response depends critically on the uniformity of the fiber lattice. An irregular fiber lattice leads to sampling non-uniformities translating into a response which depends on the particle entry point and degrades the energy resolution. A practical construction technique was thus sought to ensure a good lattice uniformity with no irregular gaps between the fibers and the lead. The construction technique adopted is based on the lamination of lead plates and scintillating fibers.

The modules consist of a stack of lead sheets with rolled semi-circular grooves sandwiching the scintillating fibers. The Pb sheets are produced commercially by the lead foundry to high mechanical tolerances to minimize gaps and non-uniformities in the lead to scintillator ratio as well as optimizing the fiber lattice uniformity. In particular, stringent tolerances of 0.01 mm are applied on the shape and size of the grooves, and on the groove to groove distance. The rolling

machine consists of a free-rotating circular die with the negative profile of the desired grooves rigidly supported above a moving flat bed die 150 cm long which also had the negative profile of the grooves. Flat extruded lead (Pb) plates with a 1% antimonial admixture are placed on the lower die and rolled by pushing the lower die under the circular die. The lower die is driven by the saddle of a precision mechanical slide with a hydraulic force of 10,000 lb. It is found that the 1% antimony admixture produced roll-able plates while preserving enough mechanical strength and rigidity to permit handling during stacking. We propose to utilize the E864 module dimensions in FoCal. The completed modules will then have a mass of about 100 kg each and an active depth of approximately $9 \Lambda_{had}$. Figure 69 shows a module stacking geometry that utilizes 372 modules producing 1488 towers. The configuration is approximately circular, 1 meter in radius, and has a total mass of approximately 40 metric tons.

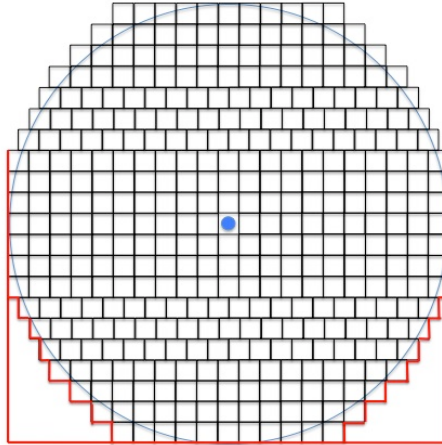


Fig. 69: A conceptual arrangement of Focal-H modules. A total of 372 modules are illustrated allowing 1488 towers of $5 \text{ cm} \times 5 \text{ cm}$ in a nearly circular geometry approximately 1 meter in radius.

5.2 Sensors and Electronics

5.2.1 Silicon pad sensors and electronics for the LGL

Low granularity pad layers: The Si sensors would have a size⁷ of $8 \text{ cm} \times 8 \text{ cm}$ with a thickness of either 500 or 300 μm and with a pad size of $1 \times 1 \text{ cm}^2$ for 64 readout pads per layer. The silicon sensor is attached to the tungsten plate with a sensor PCB mounted on top of the wafer. The n-doped Si sensor has common cathode biased to ground and negative bias (-100 V as full depletion voltage) supplied to each pad through a bias resistor. The signal from the pad is read out through a coupling capacitor. The signals from all pads are brought off the sensor readout board via ribbon cable. All sensor layers within a segment are connected to a

⁷Yet to be determined, for ease of discussion we assume one value.

passive summing board that runs along the bottom side of the segment. The summing board performs a passive longitudinal sum of the signals for each pad at the same location on all of the individual sensor layers. The result is $64 \text{ } 1 \times 1 \text{ cm}^2$ block signals from the multi-layer segment. Further details how this is done in practice can be found in Sec. B.1.

In the case of the block geometry, the summing board brings the signals from each of the longitudinal segments to the back of the FoCal-E block where the LGL readout board will be located. In the case of the slat geometry, the sensors, sensor PCB boards, and summing boards are the same as used for the block configuration, but several sensor boards will be mounted adjacent to each other on the long W slat. The signals will be brought to the back of each segment via the summing board where the LGL readout card is attached. The readout card can sit atop of, or be integrated with, the last sensor layer PCB of the segment. The basic elements of the LGL readout card would be the same in the block or slat configuration, although the form factor would obviously be different.

The LGL readout board: The readout board performs the following functions: it conditions the signals for input to a signal processing chip which shapes the signal and samples it, stores the sampled signal in an analog memory, and then transmits the analog signal to a digitization board on receipt of an event accept trigger. Efforts at CNS and ORNL related to development of a signal processing chip are described in Sec. B.1. It is intended that a multi-input chip is used to receive input signals from multiple readout channels, and multiplex the sampled outputs to an off-detector digitization board. More explicitly, the Beetle chip, which was developed for the LHCb experiment, is being considered as the chip used to perform the described functions on the readout board. The Scalable Readout System, described in the next section, is being considered to provide the off-detector signal digitization and processing functions. A readout board based on the Beetle chip is already under development by CMS for use with the SRS system.

The Beetle chip provides a low-noise charge-sensitive preamplifier and shaper for up to 128 signal inputs. In analog mode, the shaped signal is sampled at the 40 MHz clock frequency and stored in a ring-buffer pipeline that is up to 160 samples ($4 \mu\text{s}$) deep. In addition, there is a de-randomizing event buffer that is 16 events deep. The Beetle chip multiplexes the analog output of the 128 channels onto 1, 2, or 4 output lines at the 40 MHz clock speed, to be digitized off-chip, with a maximum deadtimeless readout rate of 1.1 MHz when using all 4 outputs. The Beetle chip also provides a per channel comparator with the binary result (trigger decision) of 4 adjacent channels OR'd together and brought off-chip to be available for trigger purposes.

In order to accommodate the large dynamic range required for the FoCal-E energy measurement, the LGL block segment signal will be split into two signals with a fixed relative gain (or attenuation) factor and then input to two separate inputs of the Beetle (or alternative similar chip). Fig. 70 demonstrates that with a full scale setting corresponding to 2 TeV for the block segment, a dual gain range measurement with 9-bits digitization and a factor of 8 between the two ranges, the digitization contribution to the resolution would remain well below the intrinsic resolution of the FoCal-E.

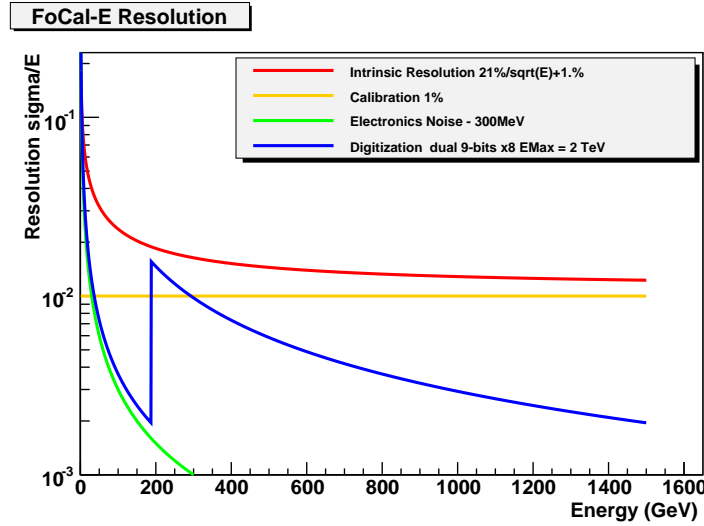


Fig. 70: The various contributions to the FoCal-E energy resolution. The terms shown include the intrinsic resolution, the calibration term assumed to be 1%, an electronic noise term assumed to be 300 MeV, and the digitization resolution for a dual gain range system with 9-bits resolution on each digitization range and a factor of 8 gain difference between the two gain ranges, with the full-scale gain range set to 1.5 TeV.

SRS readout: The readout of the FoCal-E will be based on the Scalable Readout System (SRS) which has been developed as part of the CERN RD51 project.⁸

The SRS topology is shown in Fig. 71, and consists of three stages. Signals from the detector elements are conditioned and analog buffered on an analog readout (or FEE) board (see above for more detail), which may also generate trigger primitive information. When an event is read out, the analog FEE board transmits the analog levels as multiplexed signals to the front-end card (FEC), where they are digitized and assembled as sub-events, buffered, and then transferred to the DAQ system upon receipt of the readout request from the ALICE trigger system. The transfer from the analog FEE board to the FEC is carried across commercial standard HDMI-format cables, and can accommodate a separation of up to 20 meters from a detector-mounted analog board to the crate-mounted FECs. In parallel, the FECs can continually receive trigger signals from the analog FEE boards on the same HDMI-format cables. The FEC's can also process the digitized data to form trigger primitives (such as local region energy sums) which can then be passed from the FEC to a Scalable Readout Unit (SRU) which can run trigger algorithms (such as high energy photon or jet algorithms) with information from the entire FoCal detector, including both FoCal-E and FoCal-H data. The SRU readout is currently being implemented for the readout of the ALICE EMCal extension to be installed in 2013, and as an upgrade of the readout of the entire EMCal. The SRS readout has already been incorporated into the ALICE DAQ system DATE.

⁸Further details on the SRS system can be found at the RD51-SRS webpage: <https://espace.cern.ch/rd51-wg5/srs/default.aspx>.

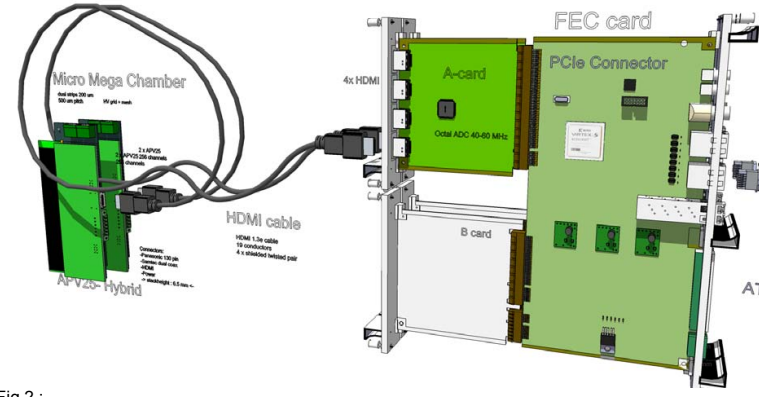


Fig. 71: The SRS system topology.

With the existing SRS implementation, each FEC can accept 2 ADC daughter boards, with each ADC board servicing 8 analog FEE boards. The SRS readout system is in the process of being commercialized to be produced by EICSYS (Embedded Integrated Control Systems) in the ATCA crate standard. In the EICSYS implementation each FEC accepts up to 2 ADC daughter boards of 12 analog FEE board inputs each. The EICSYS crate accepts up to 11 FEC cards, for readout of up to 264 analog FEE boards. The communication with the EiCSYS crate, for detector control or readout, is via Ethernet, currently at 10 Gb/s but foreseen to be at 40 Gb/s in the near future.

The readout of 192 FoCal-E blocks (or equivalent in the slat geometry) with 3 (or 4) longitudinal segmentations, and two gain ranges would require 576 (768) Beetle chips. If each single Beetle chip was connected to a SRS FEC input, 24 (32) SRS FEC cards, or 3 SRS crates would be required for readout of the full FoCal-E. If 2 or 3 Beetle chips were daisy-chained to the same FEC input, the number of FEC cards required would be decreased by the same factor of 2 or 3, at the cost of the same factor in the readout speed.

The Beetle chip multiplexes the analog output of the 128 channels on 1, 2, or 4 lines at the 40 MHz clock speed, allowing to transmit the analog data at rates of up to 275 kHz, 550 kHz, or 1.1 MHz, respectively. The SRS system has only two data lines for input to the FEC card, and so a maximum data (deadtimeless) transmission rate of 550 kHz is achievable with the Beetle chip based SRS readout, well above the maximum p+p collision rate of 200 kHz planned for ALICE.

5.2.2 Monolithic Active Pixel Sensors for HGL

The main option considered for the HGL are Monolithic Active Pixel Sensors (MAPS). MAPS are CMOS chips incorporating both a sensitive layer for ionizing radiation and some front-end electronics [71]. An advanced realization of this technology is the MIMOSA series of chips developed by IPHC Strasbourg, which is the main avenue we presently consider. Other technology paths, which are also being investigated for the ALICE ITS upgrade ([72]), will be monitored as possible fallback solutions. As the requirements in terms of read-out speed and power are similar in both projects, FoCal can profit from the MAPS developments for the ITS,

which is more advanced at present.

The MIMOSA chip has a thin epitaxial layer ($\approx 20\ \mu\text{m}$) from which charge is collected by diffusion onto a diode. Sensors of $11 \times 11\ \text{mm}^2$ size with a pixel pitch of $18 \times 18\ \mu\text{m}^2$ have been produced for the EUDET project [73]. These sensors read out the analog signal per pixel via the so-called rolling-shutter technique, where sequentially all rows are connected to discriminators in the digital part of the chip. The rolling shutter speed is the limiting factor in the rate capabilities of the chips, as the pixels integrate charge over a full rolling-shutter period. Present developments in IPHC, like in-pixel discrimination and multiple rolling shutters, aim at a read-out speed of the order of $5\ \mu\text{s}$, which would be sufficient to handle the maximum interaction rate for Pb+Pb collisions with minimal pile-up. In low-multiplicity events (p+p and p+A) pile-up can be disentangled off-line with time-stamping from the faster LGL. It is to be noted here that although the integration time of an individual pixel is, let's say $5\ \mu\text{s}$, the starttime of this integration window is determined by the row read-out clock which ticks at $0.2\ \mu\text{s}$.

In a high-energy electromagnetic shower the pixel occupancy of a chip will be much higher than in a tracking detector, the original application area of MAPS. Therefore, a very different data compression scheme has to be implemented in the digital part. In addition, for use in a calorimeter spatial information is useful down to about a tenth of a Molière radius, but certainly not to the scale of the pixel size in the MAPS. One possible strategy for data reduction is therefore a subdivision of the pixel matrix into macro-pixels of $\approx 1\ \text{mm}^2$, as it has been implemented also for the performance simulations. Other data reduction strategies will be investigated.

For the above algorithm, a count of the number of fired pixels within a macro-pixel will be obtained on-chip, and these pixel-counts will provide the analog signal for the calorimetry measurement. For a typical⁹ pixel size of $22 \times 33\ \mu\text{m}^2$ and 32×32 pixels in a macro-pixel this corresponds to signal values up to 1024, i.e. 10 bits, which may be reduced to 8 bits to account for the typical cluster size generated by a single particle.

For a calorimeter application one will encounter situations where further zero-suppression is not at all effective because of the high occupancy, like near the shower core at the layer of shower maximum. We therefore have to prepare to be able to read out the full macro-pixel matrix for a given event. For a sensor of $1 \times 3\ \text{cm}^2$ and a readout time of $5\ \mu\text{s}$,⁹ this corresponds to a data rate of 600 MBit/s.

Further data reduction could be achieved by combining the individual signals into clusters corresponding to single showers – this is however not possible on chip, as it may require to combine information from several chips. A first clustering step may be performed in front-end electronics close to the detector.

As an example, a read-out scheme has been worked out for the 3-layer slat shown in figure 66. Such a slat would have, per layer, 80 sensor chips with 640 Mb/s output rate each. As a GBTX chip has ten 320 Mb/s input links 20 GBTX chips per layer are needed. Each GBTX output is 4 Gb/s. Twelve are coupled to a 12 VCSEL array, so for the 3-layer slat nine 12-fiber MTP/MPO cables are needed. One third of these are inputs to the sensors: clock, event number, slow control.

⁹As proposed for the pixel layers in the Upgraded ITS.

This solution is more or less of-the-shelf, radhard and available via Cern. Disadvantage is the large number of GBTX chips needed and the associated power. A more advanced solution would be based on Si optical modulators. Such modules are commercially available¹⁰ and have four 8-10 Gb/s channels in a commercial QSFP+ package with a MPO 4-fiber connector. A slat would need 4-5 modules (160 Gb/s) for data output. One multiple input channel would be used for clock, event number, slow control, etc. Between the sensors and the modulator a 16-to-1 10 Gb/s multiplexer is needed, not available of-the-shelf. The advantage of this solution is the low power consumption as all optical power is generated outside, as opposed to the GBTX. However, today's commercial modules are not qualified as radiation hard.

The connectors of both solutions are of such a size that they just fit on the side of a 3-layer slat. For a single layer the connectors would take disproportionately more space, as a minimum space is required for mounting and connecting and for mechanical rigidity. A single MAPS layer would thus increase the local Molière radius of the full detector, which will have to be taken into account in the design.

5.2.3 *FoCal-H sensors and electronics*

The photo sensor for the hadronic calorimeter would likely be either an Avalanche Photodiode (APD), the same as used for the ALICE electromagnetic calorimeters, or a SiPMT. In either case, the FoCal-H would also use the SRS readout, with a similar readout board as developed for the FoCal-E, but modified as required to match the signal dynamic range to that of the multiplexing (e.g. Beetle) chip. Use of the SRS readout would allow the FoCal-H information to be combined with the FoCal-E information in an SRU module for trigger purposes, such as to provide a jet trigger based on the total jet energy. With a dual-gain range system of less than 1000 readout towers, the FoCal-H readout would require less than a single SRS readout card.

5.3 DAQ

To estimate the data volume and required readout bandwidth we consider the case of Pb+Pb collisions at the maximum planned interaction rate of 50 kHz. We estimate the total number of particles measured in the FoCal from the existing measurements of the minimum bias pseudorapidity density at mid-rapidity in Pb+Pb collisions for the lower beam energy, which is $dN_{ch}/d\eta \approx 500$ by assuming Bjorken scaling in pseudorapidity and a scaling with beam energy by $s^{0.15}$. This yields:

$$N_\gamma(5.5 \text{ TeV}) \approx N_{ch}(5.5 \text{ TeV}) \approx 1.6 \cdot 1.23 \frac{dN_{ch}}{d\eta}(2.76 \text{ TeV}) \approx 1000. \quad (12)$$

Assuming an additional factor of two, which should account for the charged particles, which would most often fire just single pixels in a layer, additional background particles, and some safety margin we will assume a hit density of 2000 particles per unit of rapidity.

¹⁰Molex Luxtera

5.3.1 LGL Readout

The FoCal-E LGL readout with the equivalent of 192 blocks consists of $192 \times 64 = 12288$ towers. With 2 gain ranges, and 3 (or 4) longitudinal segments digitized with 12-bits, the total FoCal-E LGL readout data volume is 110 kBBytes (150 kB). With the Focal-E coverage of 2 units of rapidity and 12288 towers in the LGL readout, the 2000 photon hit density in Minimum Bias Pb+Pb collisions corresponds to a 16 % photon hit occupancy. Taking into account the fact that photon showers spread over a region of $N \times N$ towers with N increasing with photon energy, the tower occupancy is expected to be essentially 100 %. At the full 50 kHz Pb+Pb interaction rate the total LGL data rate is expected to be 5.5 GB/s (7.4 GB/s) for 3 (4) longitudinal segments. With gain-range selection in the SRS FEC the volume would be reduced by a factor of 2.

5.3.2 HGL Readout

At a frame rate of 200 kHz (for 5 μ s readout time) the uncompressed raw data (10^6 8-bit values) of a single HGL of 1 m² yield a raw data rate of 200 GB/s, which is shipped to FPGA processors for immediate reduction. If every photon produces a signal in 10 \times 10 macro pixels, these would produce 10^5 fired pixels per layer. One would have to deal with an occupancy per minimum bias Pb+Pb event of 20 %. (As the multiplicity in central events is higher by approximately a factor of 3, the occupancy in these events would also be higher by the same factor.) For the readout to DAQ, it is relevant that the maximum interaction rate is 50 kHz, 1/4 of the frame rate, such that the data rate after zero suppression would be ≈ 10 GB/s.

Obviously, this will need further data reduction. A cluster algorithm implemented either in dedicated FPGA processors or in the general event processors should easily reduce the amount of data to ≈ 8 Byte for each of ≈ 2000 clusters to be measured, i.e. 16 kB/event, which yields a factor > 10 further reduction. So, after clustering, a data rate of ≈ 800 MB/s per layer could be achieved.

5.4 Integration

In most of this document the present layout of the A-side is used. However, due to the ITS upgrade, the A-side will have to be modified. In particular, the beam pipe will be extended by 0.7 m. This entails at least modifications of all support structures of forward detectors and beam line. For the FoCal location at $z = 8$ m even more significant modifications will be needed. For any scenario of FoCal it is essential that conversions are kept to a minimum, not only in the direct line-of-sight, but also near to it. It is important to take these boundary conditions into account when designing new structures – of course one will have to investigate the impact of such new structures in dedicated simulations. (In the present situation, the outer angular range of the PMD suffers from radiation generated in the services of the ITS.)

Also the interaction of other forward detectors (e.g. possible future versions of the V0 or the FMD) with FoCal has to be carefully studied. In this context a possible synergy can be exploited, because with proper segmentation and positioning the charged particle measurements could be used for trigger purposes and standalone multiplicity measurements as well as for the identification of charged particles in FoCal.

For FoCal at the $z = 8$ m position the possibilities to minimise the material budget shadowing FoCal are currently being studied. Other significant modifications are needed, which involve significant work on structures in the ALICE setup, in particular the relocation of the compensator magnet and associated beam line equipment and the installation of the support structure for the 170 kN FoCal-H.

6 Project Management and Organisation, Participating Institutes, Cost Estimates and Time Schedule

6.1 Project Management and Organisation

The ALICE Forward Calorimeter Project, in short FoCal, is a proposed upgrade for the ALICE experiment. Once approved within the ALICE collaboration it will be organized according to the ALICE Collaboration rules and constitution. The institutes that have already contributed or expressed an interest to contribute to the FoCal are listed in Table 6. The contributions and responsibilities of the participating institutes, as well as the manpower and funding resources, are being discussed and will be defined in the MoU that will be set up at the time of the Technical Design Report, which is planned for early 2014.

6.2 Participating Institutes

Table 5: List of Institutes taking part in the FoCal project

Short Name	Full Name	Representative
Amsterdam	Nikhef, Amsterdam, Netherlands	T. Peitzmann
Bergen	University of Bergen, Bergen, Norway	D. Röhrich
Copenhagen	Niels Bohr Institute, Copenhagen, Denmark	J.J. Gaardhoje
Detroit	Wayne State University, Detroit, USA	T. Cormier
Jyväskylä	University of Jyväskylä, Jyväskylä, Finland	J. Rak
Knoxville	University of Tennessee, Knoxville, USA	K. Read
Kolkata	Department of Atomic Energy, VECC, Kolkata, India	T. Nayak
Livermore	Lawrence Livermore National Laboratory (LLNL), Livermore, USA	R. Soltz
Mumbai	Bhabha Atomic Research Centre (BARC) Mumbai, India	T. Nayak
Oak Ridge	Oak Ridge National Laboratory (ORNL), Oak Ridge, USA	T.C. Awes
Prague	Czech Technical University of Prague, Prague, Czech Republic	V. Petracek
São Paolo	University of São Paolo, São Paolo, Brasil	M. Munhoz
Tokyo	University of Tokyo, Graduate School of Science, Center of Nuclear Study (CNS), Tokyo, Japan	H. Hamagaki
Utrecht	Utrecht University, Utrecht, Netherlands	T. Peitzmann

Table 6: Institutional responsibilities and contributions (preliminary).

Project Component	Participating Institution(s)
FoCal-E	
HGL sensors	Amsterdam, Bergen, Prague, Utrecht
HGL module	Amsterdam, Utrecht
cooling	Amsterdam, Prague, Utrecht
HGL readout	Amsterdam, Bergen, Utrecht
LGL sensors	Detroit, Knoxville, Kolkata, Mumbai, Oak Ridge, Prague, Tokyo
LGL FEE/TRG	Detroit, Knoxville, Kolkata, Mumbai, Oak Ridge, São Paolo, Tokyo
LGL modules	Detroit, Knoxville, Kolkata, Mumbai, Oak Ridge, Prague, Tokyo
slow control	Detroit, Kolkata, Mumbai, Prague, Tokyo
integration	Amsterdam, Detroit, Knoxville, Livermore, Oak Ridge, Prague, Utrecht
FoCal-H	
mechanics	Detroit, Knoxville, Livermore, Oak Ridge
photosensors	Detroit, Knoxville, Oak Ridge
FEE/TRG	Detroit, Knoxville, Oak Ridge
slow control	Detroit, Prague
integration	Detroit, Knoxville, Livermore, Oak Ridge, Prague

6.3 Cost Estimates

The cost estimate for FoCal-E is summarized in Table 7. The cost estimate for a detector of an outer radius of $r = 0.6$ m is based on present quotations obtained from industrial vendors and on the already purchased material. Only items which are exclusive to the FoCal are included in the table, while items common to all ALICE sub-detector (DAQ, offline, etc.) are not included. Table 8 shows similar cost estimates for FoCal-H.

Table 7: Project cost estimate for FoCal-E, including the detector itself, electronics, infrastructure and installation.

	Cost (kCHF)
tungsten	700
unit mechanics	500
silicon sensors (pads)	3100
pad electronics	300
MAPS + electronics	1250
cables and connections	200
support + integration	1200
cooling	600
total detector cost	7850

Table 8: Project cost estimate for FoCal-H.

	Cost (kCHF)
Pb plates	700
scint. Fibers + Diffuser	280
tools	140
APD + accessories	130
LED system + CR calibration	130
misc. electronics	100
packing/shipping	120
integration	350
total detector cost	1950

6.4 Time Schedule

Table 9: FoCal project timeline.

Year	Activity
2011 - 2015	R&D
2013	finalization of detector specifications analysis of prototype data
2014	final prototype Technical Design Report
2015	final design
2015 - 2018	Construction and Installation
2015 - 2017	production, construction and test of detector modules
2017	pre-assembly
2018	installation

- [1] J.C. Collins, D.E. Soper, and G. Sterman, Adv. Ser. Direct. High Energy Phys. **5**, 1 (1988).
- [2] V.N. Gribov and L.N. Lipatov, Sov. J. Nucl. Phys. **15**, 438 (1972).
- [3] G. Altarelli and G. Parisi, Nucl. Phys. . B **126**, 298 (1977).
- [4] Yu. L. Dokshitzer, Sov. Phys. JETP **46**, 641 (1977).
- [5] R. D. Ball *et al.*, (NNPDF Collaboration), Nucl. Phys. B **849**, 296 (2011).
- [6] L. McLerran and R. Venugopalan, Phys. Rev. D **49**, 3352 (1994).
- [7] F. Caola, S. Forte, and J. Rojo, Nucl. Phys. B **854**, 32 (2011).
- [8] R. Ichou and D. d'Enterria, Phys. Rev. D **82**, 014015 (2010).
- [9] S. Chatrchyan *et al.*, (CMS Collaboration), Phys. Rev. D **84**, 052011 (2011).
- [10] V. Khachatryan *et al.*, (CMS Collaboration), Phys. Rev. Lett. **106**, 082001 (2011).
- [11] S. Chatrchyan *et al.*, (CMS Collaboration), Phys. Lett. B **710**, 256 (2012).
- [12] S. Chatrchyan *et al.*, (CMS Collaboration), Phys. Rev. Lett. **109**, 152303 (2012).
- [13] K. Gulbrandsen *for the ALICE Collaboration*, arXiv:1302.0894
- [14] G. Aad *et al.*, (ATLAS Collaboration), Phys. Lett. B **706**, 150 (2011).
- [15] P. Aurenche *et al.*, http://lappweb.in2p3.fr/lapth/PHOX_FAMILY/jetphox.html.
- [16] D. d'Enterria and J. Rojo, Nucl. Phys. B **860**, 311 (2012).
- [17] J.J. Aubert *et al.*, (EMC Collaboration) Phys. Lett. B **123**, 275 (1983).
- [18] C. A. Salgado *et al.*, J. Phys. G **39**, 115010 (2012).
- [19] A.H. Rezaeian, Phys. Lett. B **718**, 1058 (2013), and private communication.
- [20] R. Vogt, Phys. Rev. C **71**, 054902 (2005).
- [21] F. Arleo, private communication.
- [22] S.S. Adler *et al.* (PHENIX collaboration), Phys. Rev. Lett. **98**, 172302 (2007).
- [23] S. Afanasiev *et al.* (PHENIX collaboration), Phys. Rev. Lett. **109**, 152302 (2012).
- [24] T. Hirano, P. Huovinen, and Y. Nara, Phys. Rev. C **84**, 011901 (2011) .
- [25] E. Braudot *et al.* (STAR collaboration), to appear in Proceedings of the 45th Rencontres de Moriond (2010) preprint arXiv:1005.2378.
- [26] J. Adams *et al.* (STAR collaboration), Phys. Rev. Lett. **97**, 152302 (2006).
- [27] A. Adare *et al.*, (PHENIX Collaboration), Phys. Rev. Lett. **107**, 172301 (2011).
- [28] J.D. Bjorken, Fermilab-Pub-82/59-THY (1982).
- [29] R. Baier, D. Schiff, and B.G. Zhakarov, Ann. Rev. Nucl. Part. Sci. **50**, 37 (2000).
- [30] M. Gyulassy, I. Vitev, X.N. Wang, and B.-W. Zhang, **Quark Gluon Plasma**, Ed. R.C. Hwa, 123 (2003).
- [31] A. Kovner and U.A. Wiedeman, **Quark Gluon Plasma**, Ed. R.C. Hwa, 192 (2003).
- [32] J.D. Bjorken, FERMILAB-PUB-82-059-THY.
- [33] M.G. Mustafa, Phys. Rev. C **72**, 014905 (2005).
- [34] S. Wicks, W. Horowitz, M. Djordjevic, and M. Gyulassy, Nucl. Phys. A **784**, 426 (2007).
- [35] K. Adcox *et al.* [PHENIX Collaboration], Phys. Rev. Lett. **88**, 022301 (2002).

- [36] C. Adler *et al.* [STAR Collaboration], Phys. Rev. Lett. **89**, 202301 (2002).
- [37] S.S. Adler *et al.* [PHENIX Collaboration], Phys. Rev. Lett. **91**, 072301 (2003).
- [38] J. Adams *et al.* [STAR Collaboration], Phys. Rev. Lett. **91**, 172302 (2003).
- [39] C. Adler *et al.* [STAR Collaboration], Phys. Rev. Lett. **90**, 082302 (2003).
- [40] J. Adams *et al.* [STAR Collaboration], Phys. Rev. Lett. **97**, 162301 (2006).
- [41] S.S. Adler *et al.* [PHENIX Collaboration], Phys. Rev. Lett. **94**, 232301 (2005)
- [42] B.B. Back *et al.* [PHOBOS Collaboration], Phys. Rev. Lett. **91**, 072302 (2003).
- [43] S.S. Adler *et al.* [PHENIX Collaboration], Phys. Rev. Lett. **91**, 072303 (2003).
- [44] J. Adams *et al.* [STAR Collaboration], Phys. Rev. Lett. **91**, 072304 (2003).
- [45] I. Arsene *et al.* [BRAHMS Collaboration], Phys. Rev. Lett. **91**, 072305 (2003).
- [46] H. Appelshäuser *et al.* [ALICE Collaboration], J. Phys. G **38**, 124014 (2011).
- [47] J. Putschke *et al.* [STAR Collaboration], J. Phys. G**34**, S679 (2007).
- [48] N. Armesto, C.A. Salgado, and U.A. Wiedemann, Phys. Rev. Lett. **93**, 242301 (2004).
- [49] A. Majumder, B. Muller, and S.A. Bass, Phys. Rev. Lett. **99**, 042301 (2007).
- [50] P. Romatschke, Phys. Rev. C **75**, 014901 (2007).
- [51] C.B. Chiu, R.C. Hwa, Phys. Rev. C **72**, 034903 (2005).
- [52] S.A. Voloshin, Nucl. Phys. A **749**, 287 (2005).
- [53] C.A. Pruneau, S. Gavin, and S.A. Voloshin, Nucl. Phys. A **802**, 107 (2008).
- [54] K. Aamodt *et al.* [ALICE collaboration], Phys. Lett. B **708**, 249 (2012).
- [55] V. Khachatryan *et al.* [CMS collaboration], JHEP **1009**, 091 (2010).
- [56] M.J. Horner *et al.* [STAR Collaboration], J. Phys. G **34**, S995 (2007).
- [57] Z. Belghobsi *et al.* [JETPHOX Collaboration], Phys. Rev. D **79**, 114024 (2009). Phys. Rev. D **79**, 114024 (2009)
- [58] H. Stoecker, Nucl. Phys. A **750**, 121 (2005).
- [59] J. Casalderrey-Solana, E.V. Shuryak, and D. Teaney, J. Phys. Conf. Ser. **27**, 22 (2005).
- [60] A.D. Polosa and C.A. Salgado, Phys. Rev. C **75**, 041901 (2007).
- [61] G. Aad *et al.* (The ATLAS collaboration), The ATLAS experiment at the CERN LHC, JINST **3**, S08003 (2008).
- [62] (The CMS collaboration), The CMS experiment at the CERN LHC, JINST **3** S08004 (2008).
- [63] S. Chatrchyan *et al.* (CMS Collaboration), Phys. Rev. Lett. **109**, 152303 (2012).
- [64] K. Gulbrandsen *et al.* (ALICE Collaboration), preprint arXiv 1302.0894 (2013).
- [65] R. Wigmans, Nucl. Instrum. Meth. A **256**, 273 (1988).
- [66] E. Bernardi *et al.*, Nucl. Instrum. Meth. A **262** 229 (1987).
- [67] D. Acosta *et al.*, Nucl. Instrum. Meth. A **294** 163 (1990).
- [68] <http://www.phenix.bnl.gov/WWW/publish/johnson/FHC/docs/864calorimeter.pdf>
- [69] <http://www-minimax.fnal.gov>
- [70] <http://www.detectors.saint-gobain.com>

- [71] R. Turchetta, *et al.*, Nucl. Instrum. Meth. **458**, 677 (2001).
- [72] The ALICE Collaboration. Upgrade of the Inner Tracking System Conceptual Design Report. CERN-LHCC-2012-013, 2012.
- [73] <http://www.euDET.org/e26/e28/e86887/e106341/EUDET-Memo-2010-33.pdf>
- [74] A. Brogna *et al.*, Manual PHASE1, IPHC Strasbourg.
- [75] M. Szelezniak, CMOS pixel vertex detector for STAR, PoS (VERTEX 2008) 032.
- [76] M. Reicher *et al.*, An extreme granularity electromagnetic calorimeter using monolithic pixels for future forward measurements in ALICE, poster 118 at QM2012.
- [77] D. Fehlker *et al.*, Highly segmented electromagnetic Calorimeter prototype, Proceedings Topical Workshop on Electronics for Particle Physics 2012 (TWEPP-12) 2012 JINST.

A Analysis algorithms

A.1 Description of clustering algorithm

1. Sort digits according to energy.
2. Calculate SeedEnergy for each digit that is over SeedThreshold.
 - (a) The SeedEnergy is the sum of all digits within the MinRing radius.
3. Loop over digits starting from the highest energy:
 - (a) End if the digit is not over SeedThreshold.
 - (b) Skip if digit was already rejected.
 - (c) Add it to the seed list.
 - (d) Loop over all nearby digits ($\text{distance} < \text{MaxRing}$):
 - i. Add weight associated to the digit.
 - ii. If $\text{distance} \leq \text{MinRing}$, reject digit as a seed.
 - iii. If energy of current digit does not exceed calculated weight by a configurable amount (RejectionRatio), reject it (it is not energetic enough to become a new seed within MaxRing of existing seed).
4. Loop over the seed list to apply additional rejection criteria (loop from the lowest SeedEnergy):
 - (a) For each seed, loop over all nearby digits ($\text{distance} < \text{MaxRing}$):
 - i. Add portion of their energy and position to the cluster that is being created.
 - ii. Portion is defined by ratio of 'added weight by this seed' and 'total weight assigned to the digit'.
 - iii. Additional properties are also computed: weighted number of digits (i.e. energy), major and minor axis of the shower shape.
 - (b) Apply criteria - weighted number of cells, energy of the cluster, if cluster does not match them, reject it:
 - i. Remove its weights from all nearby digits
 - ii. Remove it from the seed list
5. Loop over the seed list again to sum-up energy and create the clusters:
 - (a) For each seed, loop over all nearby digits ($\text{distance} < \text{MaxRing}$):
 - i. Add portion of their energy and position to the cluster that is being created.
 - ii. Additional properties are also computed.

A.2 Description of shower reconstruction algorithm

1. Loop over all LGL segments, starting with the seed segment:
 - (a) For all clusters in a given segment, find close but not-yet-merged clusters in other LGL segments.
 - (b) If they are within the MinRing parameter distance in the (x, y) -plane, merge them.
 - i. The position of each cluster is projected to the $Z_{FOCALcenter}$ plane, assuming that the track originates at the interaction vertex. (This allows to compare the transverse distance of separation for clusters from different segments.)
 - ii. The energies are added, the position is taken as the energy-weighted average.
 - (c) Mark clusters as merged, so that they are not merged again.
2. Do the same for HGL segments. (At this point, we have a list of semi-final clusters (sf-clusters).)
3. Loop over sf-clusters from HGL segments.
 - (a) Find the closest LGL sf-cluster and assign energy to it as weight.
 - (b) If there is no nearby LGL sf-cluster (XY distance $<$ MinRing), the HGL sf-cluster is thrown away.
4. Loop over sf-clusters from HGL again.
 - (a) Take from the closest LGL sf-cluster appropriate amount of energy (assigned energy by this HGL sf-cluster / total assigned energy)
 - (b) create final cluster using this energy information and position information of the HGL sf-cluster
5. LGL sf-clusters with no assigned weight also create final cluster, using both energy and position information from the LGL sf-cluster.

B FoCal R&D and Prototype Results

B.1 W+Si pad prototype

W+Si pad prototype and beam tests: Development of a W+Si pad prototype began in 2011 by the CNS group. Figure B.1 shows the longitudinal segmentation of the prototype, where 14 layers of W+Si pad modules are installed on the summing board.

Figure B.2 shows a Si pad sensor produced by Hamamatsu Co. Ltd. This Si sensor has a size of $9.3\text{ cm} \times 9.3\text{ cm} \times 535\text{ }\mu\text{m}$ (thickness) and contains 64 readout pads with pad size of $1.1 \times 1.1\text{ cm}^2$. Figure B.3 shows one layer of W+Si pad module. A heavy alloy tungsten (94W+4Ni+2Cu) plate with $9.3 \times 9.3\text{ cm}^2$ was used in the prototype and is attached to the Si sensor. This n-doped Si sensor has common cathode biased to ground and negative bias (-100 V as full depletion voltage) supplied to each pad through a $10\text{ M}\Omega$ register. The signal from the pad

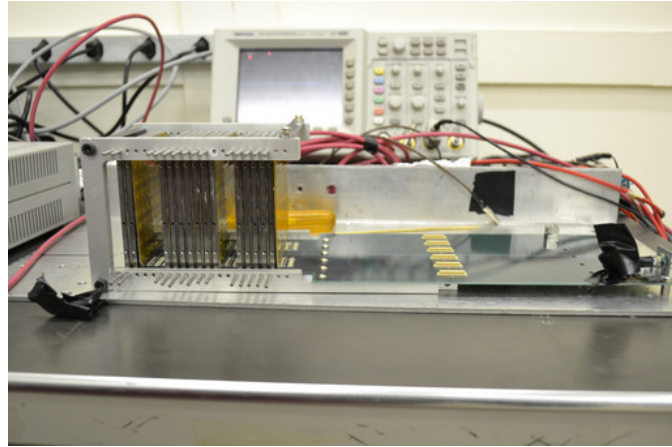


Fig. B.1: W+Si prototype with 14 layers of W+Si pad modules on the summing board.

is read out through a coupling capacitor of 10nF . The signals from all pads are brought off the sensor readout board via ribbon cable to the passive summing board. For each pad, the summing board performs a passive longitudinal sum of the signals from all of the individual sensor layers, to form a tower signal from the multi-layer segment. The composition of one W+Si pad layer is as follows: W of 3.5 mm thickness, glue (EP001N: a few μm thickness), Si pad (0.535 μm), glue, flexible board (0.175 mm thickness), and FR4 board (1 mm thickness).

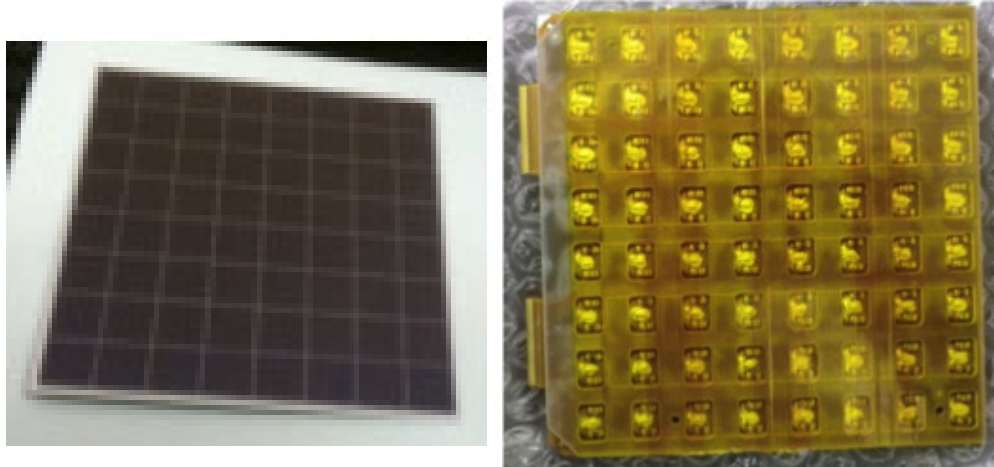


Fig. B.2: Si pad sensor produced by Hamamatsu.

Fig. B.3: The view of one layer W+Si pad module (seen from the pad side).

A beam test of the W+Si pad prototype was conducted at the T9 beamline at the CERN-PS in November 2011. A prototype segment with 8 W+Si pad layers was tested during this beam test. (Unfortunately, after the full setup with 14 W+Si pad layers was installed, the PS beam period was prematurely terminated due to a vacuum leak, after a period of less than 2 days with beam.) The beam energies used in this beam test were 3, 4, and 5 GeV.

Figure B.4 shows the setup of the 8 layer pad prototype at the beamtest. In front of the prototype, three layers of single-sided silicon strip detectors with spatial resolution of $40\ \mu\text{m}$ were installed to track the beam particles. A Cherenkov counter was used for electron/pion separation, and two scintillators were used for the beam trigger.

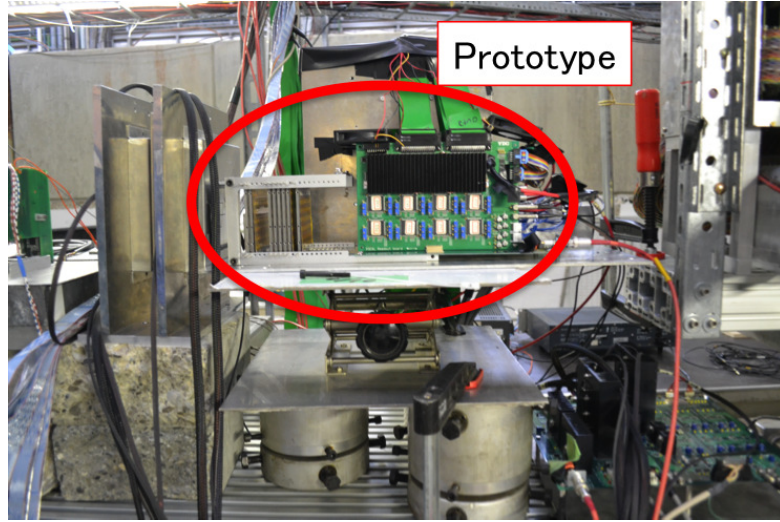


Fig. B.4: Experimental setup of the 8 layer W+Si pad prototype at the beamtest at the CERN-PS.

Figure B.5 shows the signal distributions for charged pion (blue) and pedestal noise (red) after removal of correlated noise. The MIP signal from charged pions is clearly separated from the noise with a S/N of around 6-10, depending on the pad or electronics (chip).

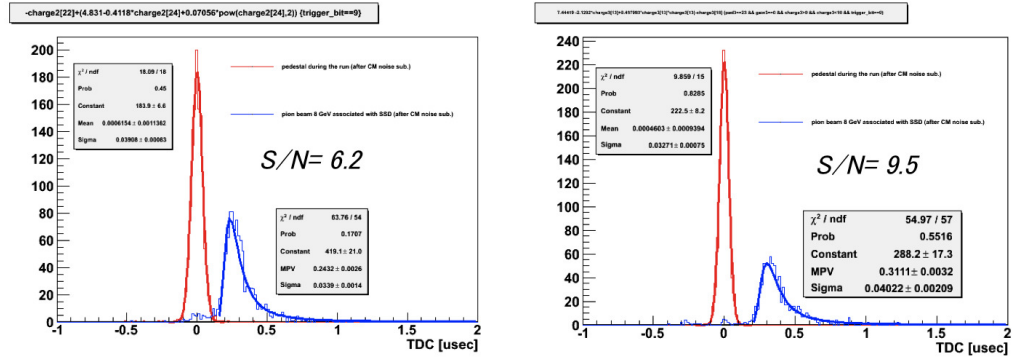


Fig. B.5: Signal distributions for charged pions (blue) and pedestal noise (red) for two different Si pads.

Figure B.6 shows the signal distributions for electrons at beam energies of 3 (upper left), 4 (upper right), and 5 (lower left) GeV, where the energy summation was taken over 3×3 pads. It is seen that the peak position clearly increases with the beam energy and that the relative resolution improves as the energy increases.

Figure B.7 shows the linearity (left) and resolution (right) for the prototype of 8 layers of W+Si pad modules as a function of the electron beam energy. Simulation results based on AliROOT

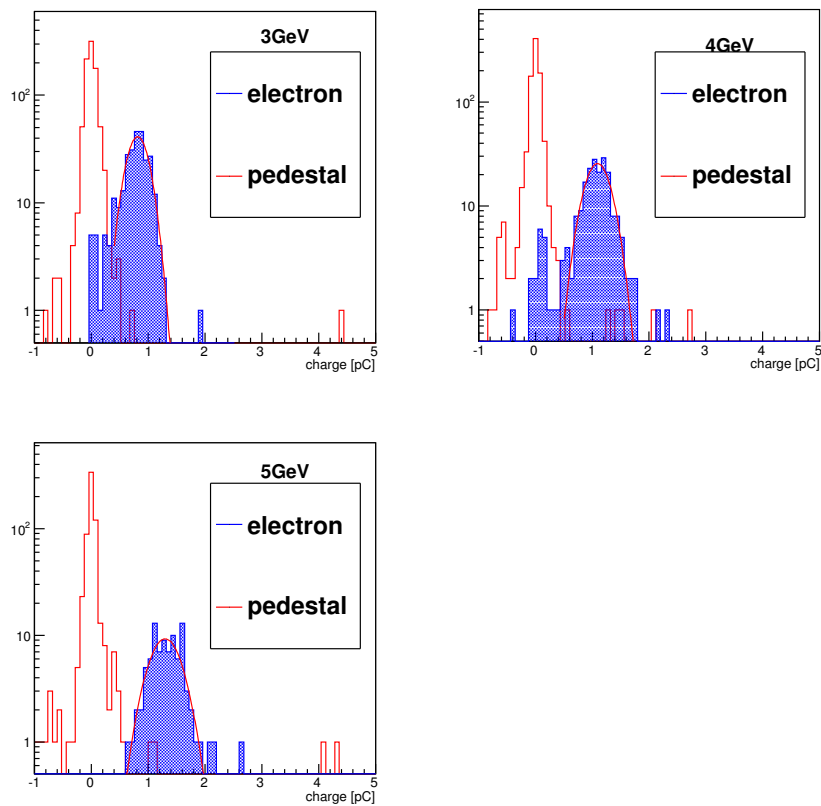


Fig. B.6: Measured signal distributions of electrons with 3 (upper left), 4 (upper right), and 5 GeV (lower left).

were performed with different Si thickness (300 μm and 525 μm) and are compared to the measured linearity and resolution shown in Fig. B.7.

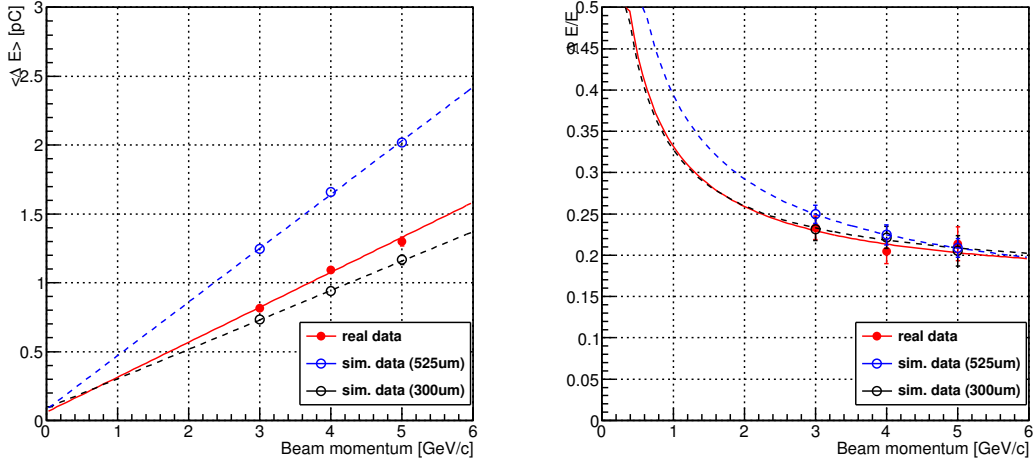


Fig. B.7: Left: Linearity. Right: Resolution. Closed: measurement. Open: simulation with 525 μm and 300 μm thickness.

According to the comparison, the resolution from the measurements is consistent with that of the simulation, however, the measured energy is 30 % lower than expected from simulation for the actual thickness of 525 μm . (Since applied HV was only -70 V, the thickness of the depletion layer in the Si could have been only $\sim 420 \mu\text{m}$.) Detailed studies are ongoing to understand the source of the observed signal deficit.

Figure B.8 shows the correlation between EM shower cluster position measured with the W+Si pad prototype and the beam position measured with the SSD installed in front of the prototype. The EM shower cluster position was extracted from the center of gravity of the energy deposition amongst the 3×3 pads. A clear correlation between the two position measurements is seen. A position resolution of 0.18 cm for the EM shower position is achieved, as shown in Fig B.9.

B.1.1 Pad sensor ASIC development at CNS:

In parallel with the preparation of the prototype W+Si pad detector, an Application Specific Integrated Circuit (ASIC) chip to process the pad signals is under development. Currently, two separate developments are underway for the pad readout, one by CNS and the other by ORNL.

The ASIC must be able to cover a wide dynamic range from 10 fC to 200 pC with a noise level that should be less than 3×10^4 ENC. Cross-talk between channels must be less than 1 % in order to achieve a good energy measurement. Moreover, it is desirable that the FoCAL has the capability to provide a fast trigger, which requires fast processing of the signal.

The prototype ASIC developed at CNS is a current conveyor amplifier with 4 different gain outputs, shaping amplifier, analog memory cell, and multiplexer as shown in Fig. B.10. Figure B.11

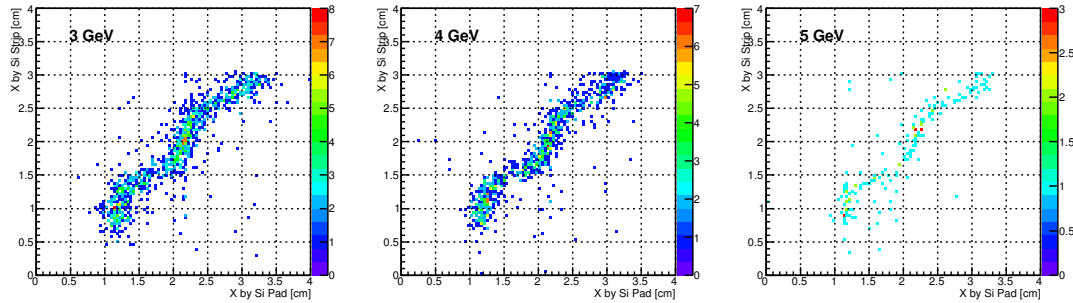


Fig. B.8: Correlation between measured EM shower cluster position with the W+Si pad prototype and beam position measured with the SSD.

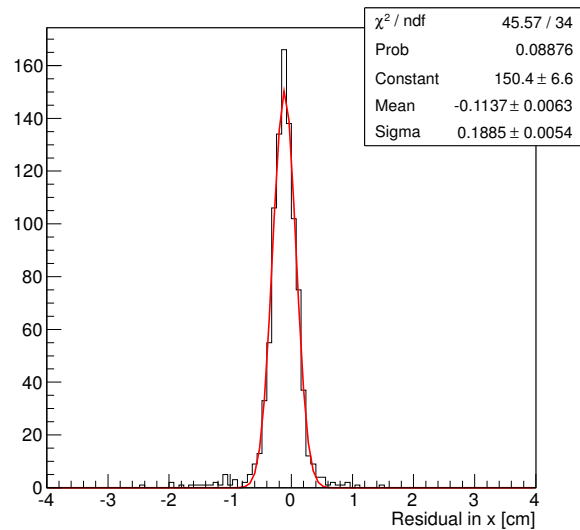


Fig. B.9: Residual distribution between the EM shower cluster position measured in the W+Si pad prototype and the beam position measured in the SSD.

shows the linearity from each gain output obtained by an hSPICE simulation.

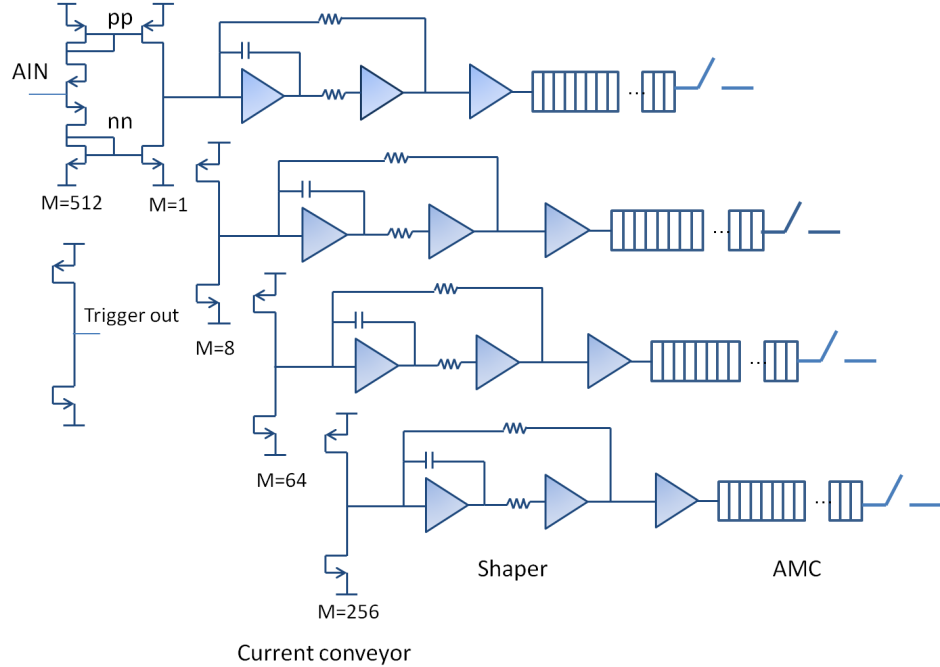


Fig. B.10: Schematics of the prototype CNS ASIC.

The number of input channels per chip is 6 and the analog current signal from the 6 input channels is summed and available for the trigger signal. Figure B.12 shows the current sum signal for different input charges (20, 100, and 200 pC) obtained by hSPICE simulations (terminated by $50\ \Omega$).

The CNS ASIC chip is being fabricated by UMC in a 0.25 μm process and the overall performance will be tested.

B.1.2 Pad sensor ASIC development at ORNL:

Another ASIC prototype chip is under development by ORNL. Because of the large amount of charge per event available, and the need for a fast trigger signal (fast preamplifier response), a traditional CSP is not ideal. Therefore a very fast high-speed follower topology similar to that used on a photomultiplier tube is being developed. This will allow to maintain high speed, low noise, and simplicity at the front end detector, with sufficient bandwidth to provide a fast trigger without having to maintain a high bandwidth closed loop CSP. Processing electronics can be placed away from the detector thus somewhat mitigating heat and power-distribution problems. The follower circuit is shown in Fig. B.13. Simulations indicate that if the design of the detector/follower is such that the maximum input charge results in an approximately 1.6 V output, the circuit will exhibit noise of approximately $108\ \mu\text{V rms}$, a peak/rms ratio of 14,800. This shows that it will likely not be limited by noise, but by inter-channel crosstalk. The follower requires a buffered output, preferably differential to minimize crosstalk. The output

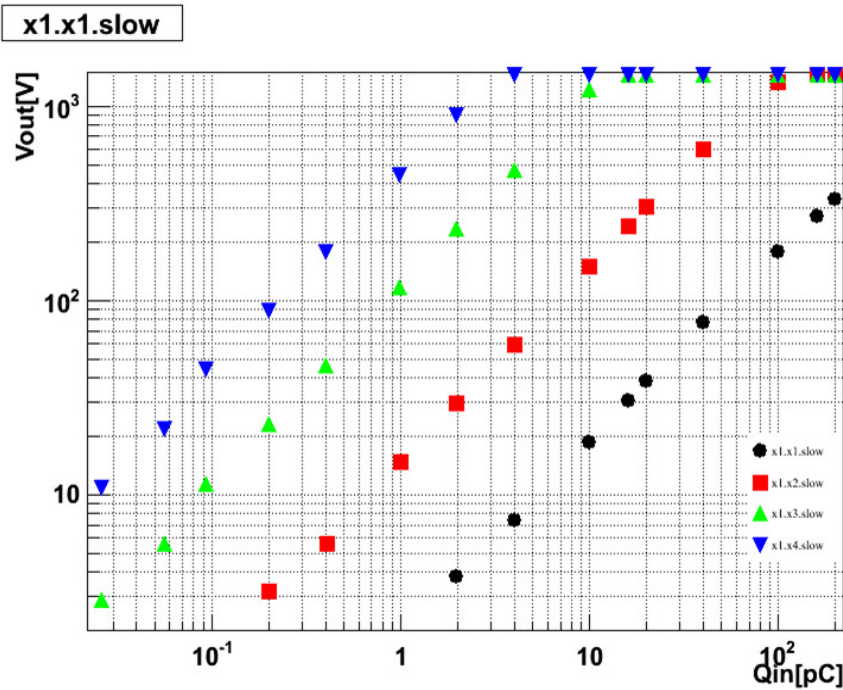


Fig. B.11: Linearity of the CNS ASIC for each of the four gain ranges.

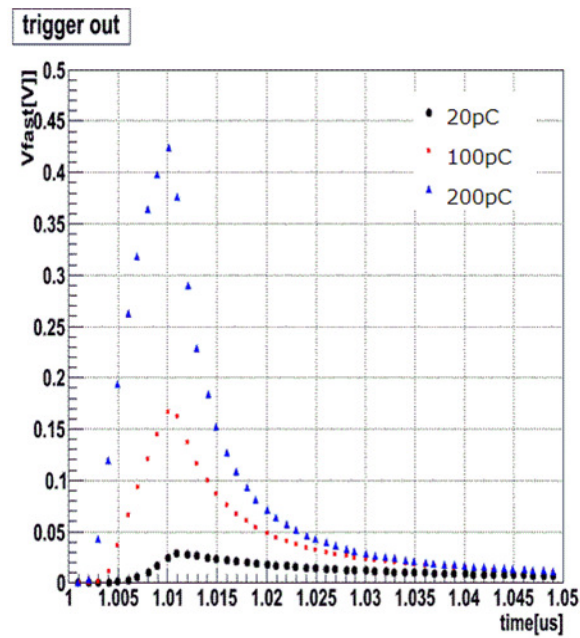


Fig. B.12: Output of current sum signals for different input charge (20, 100, and 200 pC)

of the differential buffer will drive the signal to an area with more available space, where it will be connected to processing electronics (shaper, trigger processor, ADC), simplifying their requirements.

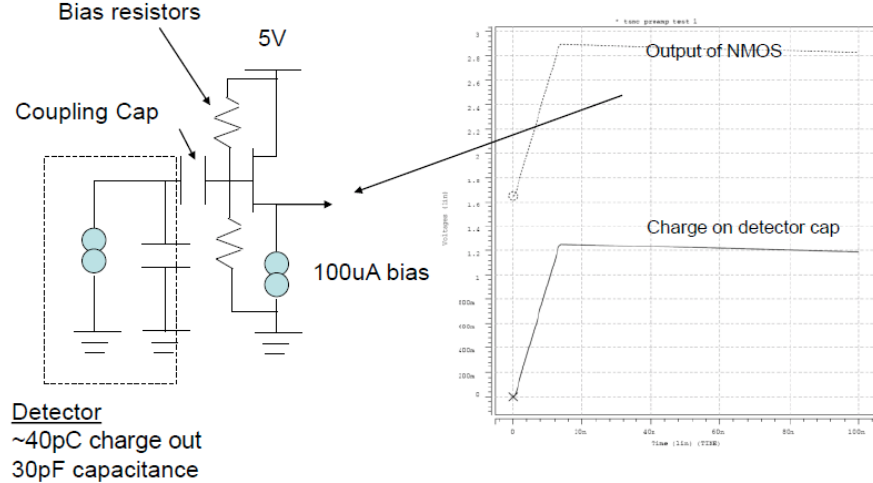


Fig. B.13: ORNL ASIC follower schematic and simulated output signal.

The block diagram for the proposed preamplifier/driver is shown in Fig. B.14. The preamplifier connects to the detector as shown in Fig. B.13 (through a coupling capacitor if needed) and can utilize either polarity of charge input. There are bias setting resistors on the chip that set the quiescent input voltage. When an event occurs, the charge is collected on the detector capacitance and the voltage output is buffered and sent to the single-ended-to-differential driver. This driver is designed to drive a 100-ohm differential line. The power dissipation is under 10 mW for the entire circuit which operates on 2.5 V. The preamplifier is presently under design in the TSMC 0.25 μ m CMOS process. An eight channel version of the chip has been submitted to MOSIS for fabrication and packaging. After testing is planned to be used in the next round of W+Si pad prototype tests.

B.2 W+Si MAPS prototype and beam tests

The development of a MAPS prototype began in 2011. This prototype serves as a technology demonstrator showing the feasibility of digital calorimetry. Its aim is further to provide data from which the resolution and linearity can be determined, as well the optimum pixel size. The latter is important because for digital calorimetry to work, there should be maximum one particle in each pixel. The prototype is not meant to validate the sensor, but to provide useful knowledge for the development of a dedicated sensor for calorimetry. We chose the PHASE2 sensor originally developed by IPHC Strasbourg for the STAR-PXL detector, ([74],[75]). This is the only full size MAPS which allows the continuous read-out of all pixels, albeit at the cost of a long integration time of 640 μ s. The small pixel pitch of 30 μ m allows very fine sampling of the shower core, where simulations have never been verified. Figure B.15 shows the prototype[76]. Its transverse size of 40 mm, dictated by the PHASE2 size, corresponds to a bit less than four Molière radii,

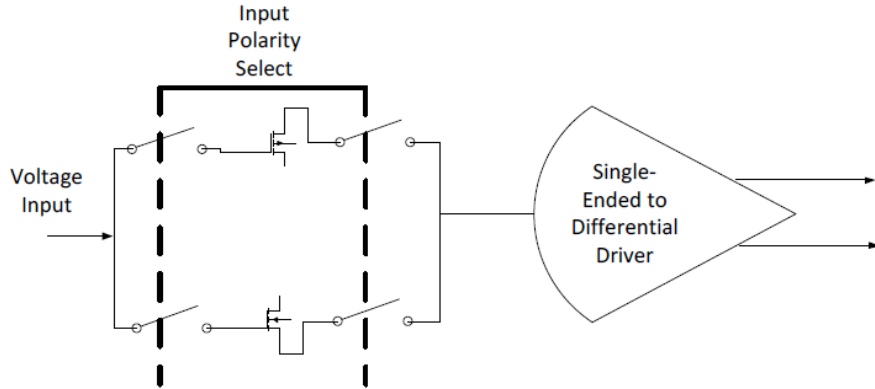


Fig. B.14: ORNL ASIC block diagram.

just enough to contain a shower. To achieve such a small Molière radius, whilst having enough layers to reach an acceptable sampling fraction, required a longitudinally very compact design.

Figure B.16 shows the MIMOSA23/PHASE2 sensor bonded to a specially developed PCB. The sensor is thinned no further down than to $120\ \mu\text{m}$ for ease of handling. As the active layer is only $15\ \mu\text{m}$ thick, thinning to $50\ \mu\text{m}$ is very well possible and is the baseline for the ITS upgrade [72]. In a calorimeter mass is of less importance and the distance between the absorbers is determined by other components like cabling. This spacing is however the determining factor for the Molière radius of the total construction as it consists of light materials including air and should be kept to a minimum. In this prototype the empty space between the absorber and the opposite sensor was filled with a thin tungsten plate, rather than leaving it open.

Two of these units are mounted side-by-side on a common tungsten absorber with a thickness of 1.5 mm. Such a module (figure B.17, left) together with cables is the basic building block forming one half layer. For a layer (figure B.17, right) two modules are placed on top of each other. The upper one is flipped over and displaced slightly such that the active areas of the sensors overlap. The space between the absorbers is 0.9 mm.

The composition of one layer can be seen in figure B.18. Note the small distance of 0.1 mm between the sensors. Thanks to this compactness, the estimated Molière radius is 11 mm, with a layer thickness of $0.97 X_0$.

Although this prototype has the minimum size required to contain a shower of tens of GeV, it has no less than 39 million pixels. Even with a very modest frame rate of 1.6 kHz the read-out system has to manage 7 GB/s datarate. Several FPGAs are used to manage this, see fig. B.19. A big local buffer memory allows to profit from the small duty factor of PS/SPS for writing the data to disk. The read-out system is described in detail in [77]. Because each sensor has its own cable, the set-up is dominated by the interconnections (fig. B.20).

Beam tests of the MAPS prototype were conducted at DESY, at the T9 beamline at the CERN-PS and at the H2 beamline at the CERN-SPS between March and September 2012. The test

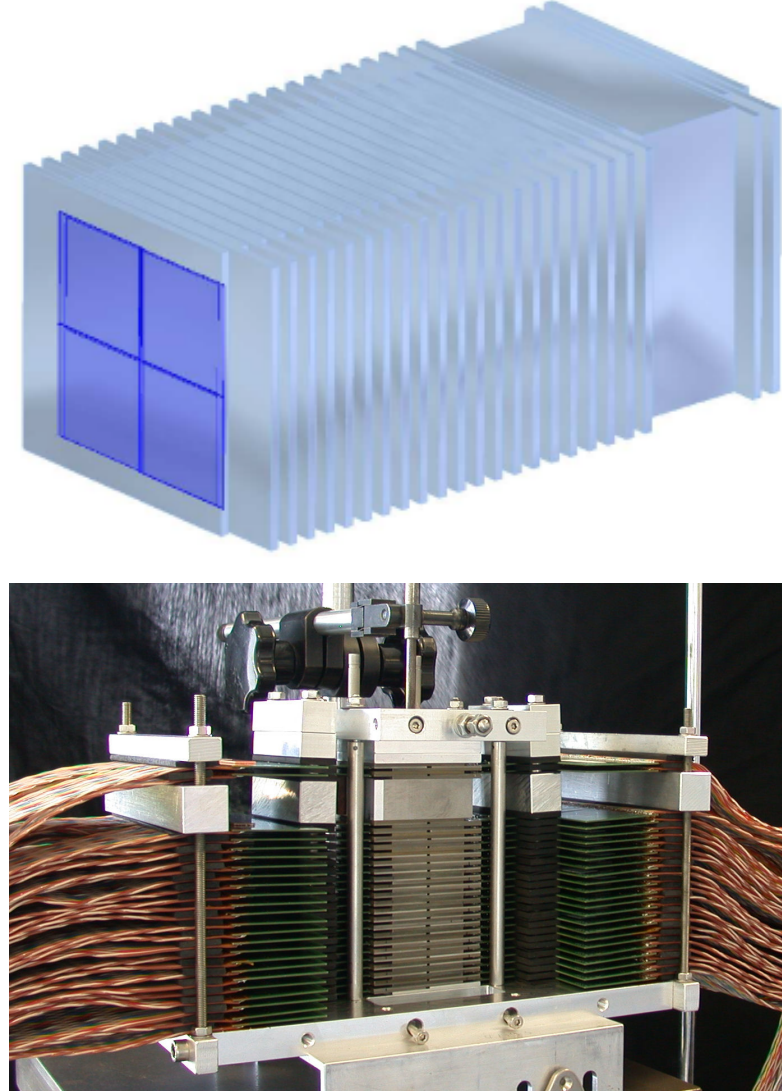


Fig. B.15: The MAPS prototype. *top*: Sketch showing the 24 active layers with 4 sensors each and the additional 20 mm W absorber before the last two layers. The transverse size of a layer is 50 mm. *bottom*: Sideview during assembly with the 24 layers in the centre and their read-out PCBs with cables on both sides. The z axis is vertical

at DESY was done with a prototype of 19 layers, the tests at CERN with a prototype of 24 layers. In the latter one, 20 mm of W was inserted before the last two layers, to increase the total radiation thickness to $28 X_0$. The beam energies and particle species used in this beam tests are given in table B.1.

Figure B.20 shows the setup of the MAPS prototype in the SPS beamtest. In front of the prototype, two scintillators were used as beam trigger. A front and a back scintillator of the same size

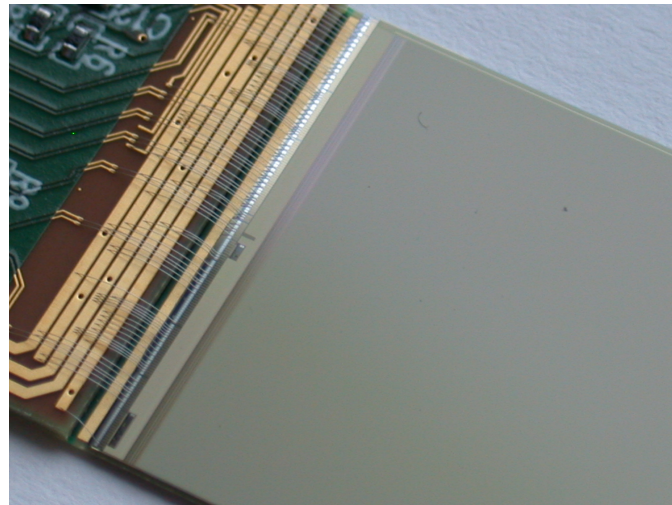


Fig. B.16: PHASE2 sensor bonded to PCB.

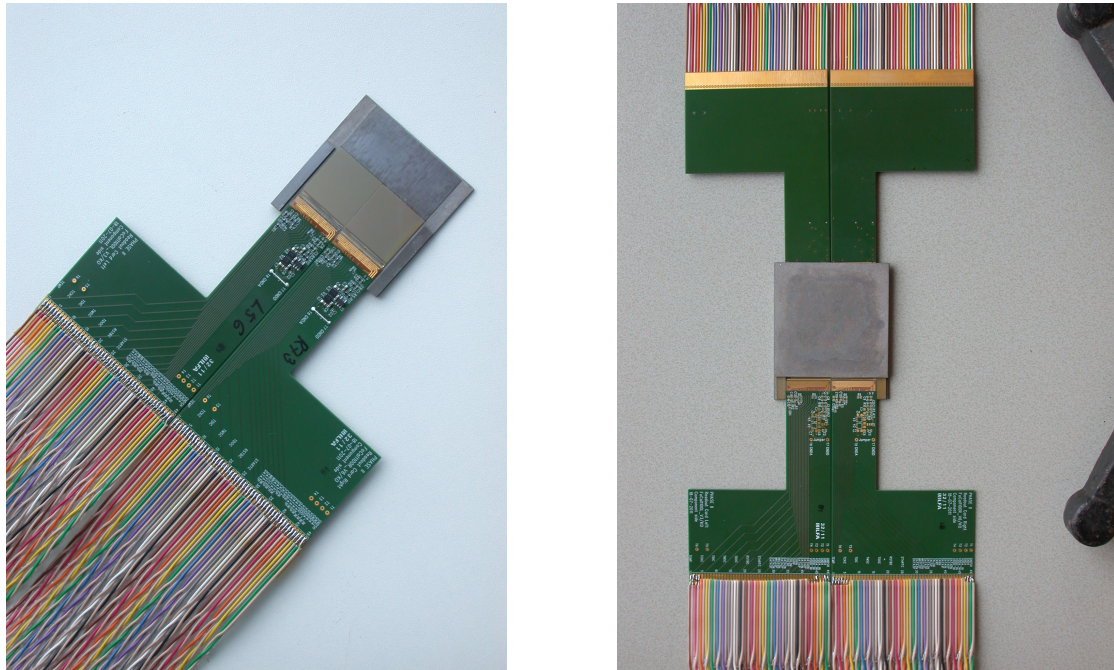


Fig. B.17: *left:* Module consisting of two sensors on a common W absorber. *right:* One layer consisting of two modules facing each other. The tungsten plate is 50 mm wide.

as the active area of the sensors served to label the incoming and outgoing particles. At the PS a Cherenkov threshold counter was used for electron/pion separation.

The analysis of the data taken during the various beamtests is in progress. To give a flavour of the data collected we show in figure B.21 all the hits caused by a single electron hitting the

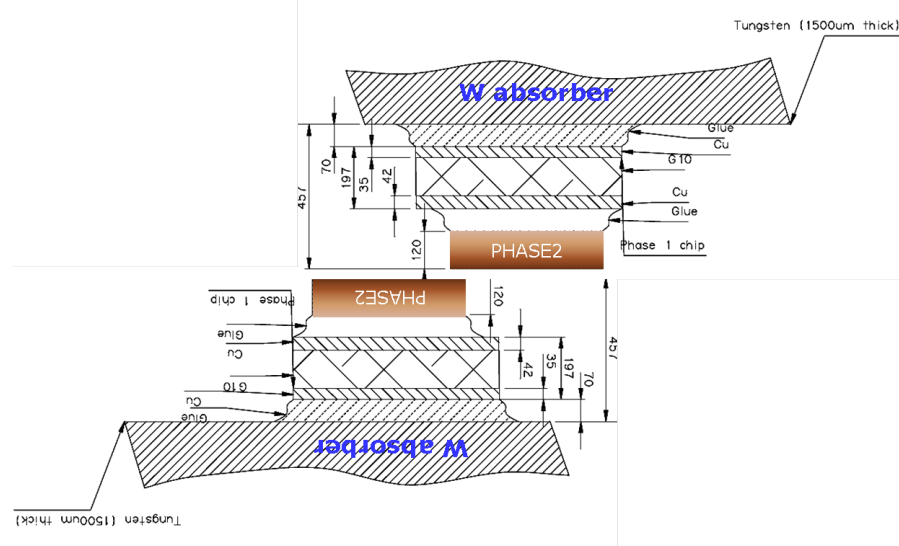


Fig. B.18: Schematic cross section of one layer along the Y-axis, showing the composition of one layer. From top to centre: W absorber, glue, PCB (Cu, G10, Cu), glue, sensor, air. Outside the overlap region the sensors are facing tungsten.

Table B.1: Particle species and momenta used in the beamtests

testbeam	momenta [GeV/c]	particle species
DESY	-2, -5	e^-
CERN-PS	-2, -5, 5, 8	e^-, π
CERN-SPS	-150, 30, 50, 100, 200	e^-, e^+, π

calorimeter, projected on the xy plane. The difference between a shower of 2 GeV and 5 GeV is obvious.

Figure B.22 shows the distributions of the number of hits in the calorimeter for runs taken at DESY with electrons at beam energies of 2 and 5 GeV. In red are the hit distributions in the same set-up, without beam. It is seen that the peak position clearly shifts with the beam energy and that the relative resolution improves as the energy increases.

Given the fact that the PHASE2 was designed for a tracker application one can expect an excellent position resolution. To demonstrate this we show (fig. B.23) the response to a non showering single pion of 200 GeV/c. (As the prototype has 0.9 pion interaction length a fraction of the pions will create a shower). In the left plot all hits are projected on the xy plane and the resulting spread is due to the mutual misalignment of the 96 sensors. On the right an extreme zoomed-in view of one layer is shown. In this view the sensors are plotted next to each other. A particle in the overlap zone will pass through both sensors. Indeed we see two clusters, one for each sensor. From the plot we determine the overlap of the sensors (in x) to be 0.6 mm, while the misalignment in y appears to be 0.1 mm. The clustersize of 4 pixels is due to charge sharing.

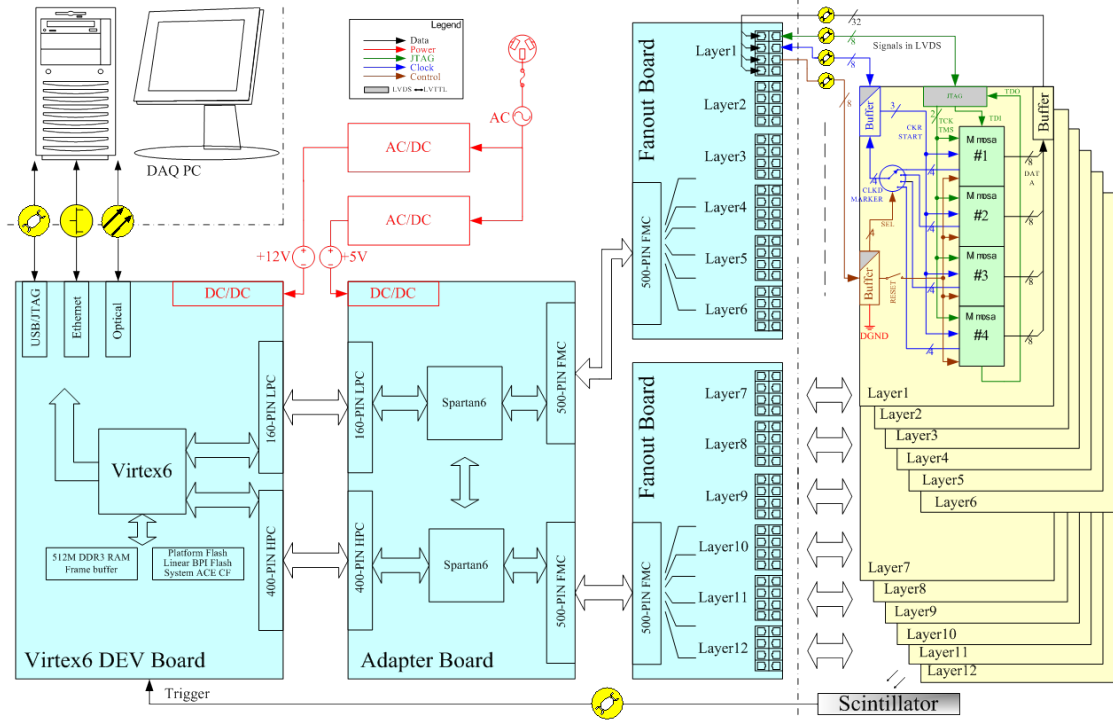


Fig. B.19: Schematic of the read-out electronics for the prototype tower. Only the circuits for 12 layers are shown.

To illustrate the particle identification capabilities we show in figure B.24 all hits, projected on the xy plane, caused by a single pion (left) and a single electron (right) of 200 GeV/c. The difference between these and also the MIP track in fig. B.23 is obvious.

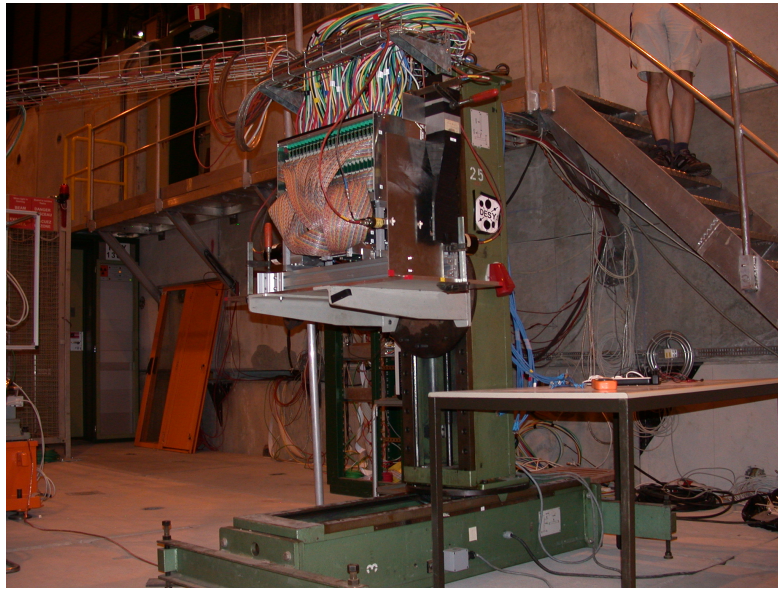


Fig. B.20: Experimental setup of the MAPS prototype at the CERN-SPS.

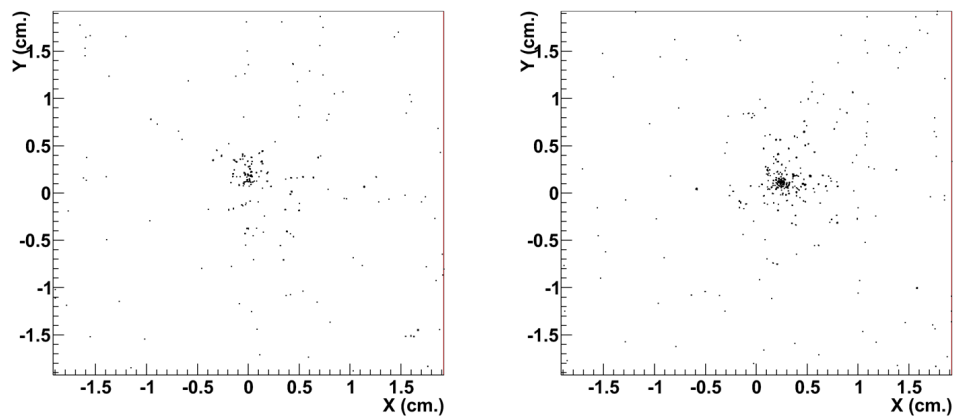


Fig. B.21: Pattern of hits caused by an electron of 2 GeV (left) and 5 GeV (right), respectively. The hits of all layers have been projected onto the xy plane.

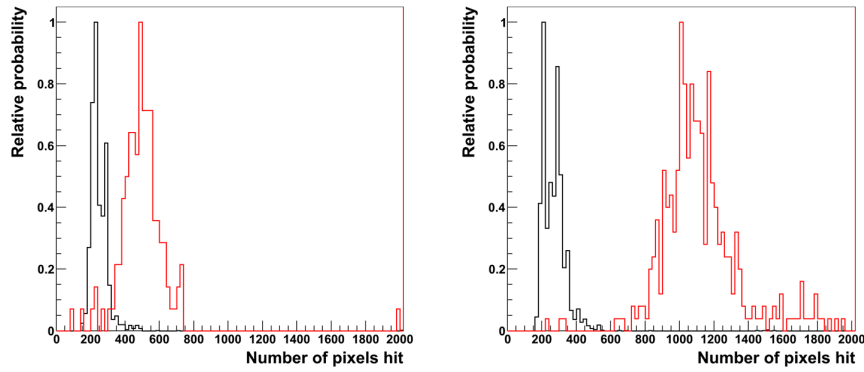


Fig. B.22: Measured hit distributions: in black without beam, in red with beam of electrons of 2 GeV (left) and 5 GeV (right), respectively.

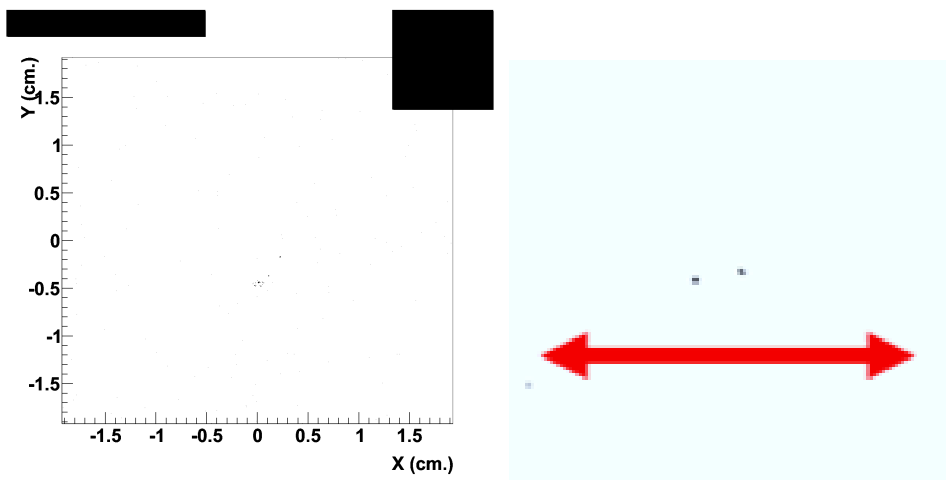


Fig. B.23: Measured hit pattern of a not showering pion of $200 \text{ GeV}/c$, *left*: all layers summed, *right*: a highly enlarged hitpattern of one layer, showing individual pixels. The length of the arrow is 5 mm.

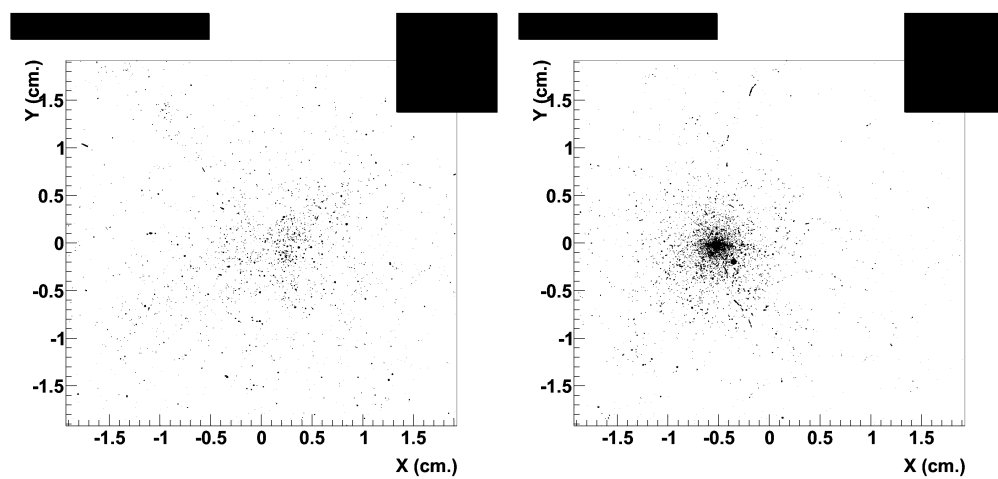


Fig. B.24: Measured hit patterns of 200 GeV/c particles: *left*: a pion and *right*: an electron.